SYNTHESIS OF GROUP IV TRANSITION METAL CHALCOGENIDES AND RELEVANT SOLID SOLUTIONS FOR ELECTRONICS APPLICATIONS

by

MATTHEW D. SEIVERT

(Under the Direction of Tina T. Salguero)

ABSTRACT

The chemistry of low-dimensional layered materials has drawn significant interest with a particular focus on the transition metal chalcogenides, a class of materials with a number of unique properties making them exceptional candidates for next generation electronics. Special interest has focused on the isolation and tunability of these materials and the study of their underlying properties as a result. In Chapter II, we focus on developing synthetic routes to isolate both polycrystalline and single crystalline $HfTe_3$. We find that the synthetic conditions employed in this study must be carefully tailored to isolate single phase $HfTe_3$. Furthermore, we find that deviations in these synthetic routes could inevitably lead to oxidation or the formation of neighboring phases. In Chapter III, we examine the synthesis of $Hf_xZr_{1-x}Te_3$ solid solutions which we develop by leveraging the chemistry of both $HfTe_3$ and $ZrTe_3$. Our study found that as we increase Hf incorporation into these solid solutions that our synthetic conditions rely more on the chemistry of $HfTe_3$, especially in respect to single phase isolation and crystal growth. Finally, in Chapter IV, we consider the isolation of three new solid solutions including $Ti_xZr_{1-x}Te_2$, $Ti_xHf_{1-x}Te_2$, and $Ti_xZr_{1-x}Se_2$. We found solid solutions of $Ti_xZr_{1-x}Te_2$ and $Ti_xHf_{1-x}Te_2$ are isolated by tuning the synthetic parameters related to the chemistry of $TiTe_2$, $ZrTe_2$, and $HfTe_2$, whereas $Ti_xZr_{1-x}Se_2$ solid

solutions are all synthesized using a uniform, but narrow temperature gradient. As a result, these findings further expands the chemistry of novel group IV transition metal chalcogenide materials which can be employed for the development of novel electronics applications and devices.

INDEX WORDS: transition metal dichalcogenides, transition metal trichalcogenides, solid state synthesis, chemical vapor transport, solid solutions, crystal growth, phase isolation

SYNTHESIS OF GROUP IV TRANSITION METAL CHALCOGENIDES AND RELEVANT SOLID SOLUTIONS FOR ELECTRONICS APPLICATIONS

by

MATTHEW D. SEIVERT

BS, University of West Florida, 2017

A Dissertation Submitted to the Graduate Faculty of The University of Georgia in Partial Fulfillment of the Requirements for the Degree

DOCTOR OF PHILOSOPHY

ATHENS, GEORGIA

2022

SYNTHESIS OF GROUP IV TRANSITION METAL CHALCOGENIDES AND RELEVANT SOLID SOLUTIONS FOR ELECTRONICS APPLICATIONS

by

MATTHEW D. SEIVERT

Major Professor:	Tina T. Salguero
Committee:	Paul A. Schroeder
	Jason Locklin

Electronic Version Approved:

Ron Walcott
Vice Provost for Graduate Education and Dean of the Graduate School
The University of Georgia
August 2022

DEDICATION

To my parents—I am eternally grateful for your help and support

ACKNOWLEDGEMENTS

I want to thank my Lord and Savior Jesus Christ for everything He has done for me, and for helping me through every step of graduate school. My faith in You was absolutely critical to my success in graduate school. I must also express my gratitude to my wonderful parents, Charles and Maria Seivert, for your unending love and encouragement throughout this journey. You have both showed me unwavering support through every step of not only graduate school, but in all of my educational and professional pursuits. I will never forget all of the encouragement you have both given me and for always pushing me to follow my dreams and believe in myself.

I must also thank my research advisor, Dr. Tina Salguero, for her guidance and mentorship through my graduate school career, and for always encouraging me to try new experiments and explore different techniques. Under her direction I have had the opportunity to develop new skills, expand my scientific intuition, and grow as a scientist and researcher. Thanks also to my committee members, Dr. Paul Schroeder and Dr. Jason Locklin, for your help throughout the years.

My appreciation also extends to both former and current members of the Salguero group for all of their help. I want to especially thank Eman Abdelrahman, Yassamin Ghafouri, Brad Norvell, Nick Nguyen, Harshani Rathnaweera, Greg Neher, Monika Milkovska, Nick Sesing, Xena Mansoura, and Casey Rowe for all of their support and friendships along this journey. It was an absolute pleasure working with all of you throughout the years. My sincerest gratitude to Eman Abdelrahman for being a huge support system for me while in graduate school, and for always being willing to help me in my research and teaching.

My gratitude extends to Kyle Meyer and Annalee Pickett for assisting me with all of my glassblowing needs, and for always being willing to go the extra mile in helping me reach my research goals. I also would like to thank Dr. Eric Formo for all of his help with electron microscopy.

Thank you to Dr. Sue Ellenberger for helping me become a better teacher, and for trusting me with so many different opportunities that aided me in my pedagogical practices. Thank you also to Dr. Zoe Morris for her insight, and for helping improve my teaching and approaches towards inclusive pedagogy.

I cannot forget to thank the many faculty members at the University of West Florida and Gulf Coast State College who helped me through my educational journey. Dr. Pamela Vaughan, thank you for the opportunity to do research in your lab and for all of your mentorship. Thank you also to Drs. Karen Molek, Karen Barnes, Linda Fitzhugh, and Sandra Etheridge for all of their help and guidance.

I also want to thank Billy Bolding for always encouraging me and being one of my biggest supporters. Thank you also to Jana Votavova for her help since our days at Gulf Coast State College, and for always giving solid show recommendations.

I also want to thank the cast and crew of the many television shows that helped keep me sane not only during the writing of this dissertation, but over the past five years. While there are too many shows to mention here, I would like to specifically acknowledge *Breaking Bad*, *Better Call Saul*, *Ozark*, *The Umbrella Academy*, *Avatar the Last Airbender*, *Dragon Ball Z* and *Super*, *Suits*, *Game of Thrones,* and *Modern Family*.

And finally, I must thank all of the individuals not directly named here who were involved in my success. It is impossible to name every person who has helped me along this journey, but I am grateful, nonetheless.

TABLE OF CONTENTS

Page

CHAPTER 1

INTRODUCTION AND LITERATURE REVIEW

Low-Dimensional Materials

Low-dimensional materials have received significant interest due to their exceptional properties making them unique candidates for electronic devices, batteries, drug delivery, supercapacitors, and a vast number of other applications.[1] In general, these materials are often defined as having their size or one of their dimensions in the range of 1 to 100 nm, and/or as a material whose chemical or physical properties (or both) change as the size of the materials change.[1,2] A very notable example of this phenomenon is gold, whose physical and chemical properties change as its dimensionality is decreased. As a result of this phenomenon, gold nanoparticles have been used extensively for applications in catalysis, drug delivery, bioimaging, etc.[3]

The dimensionality of nanomaterials are generally classified in four different categories: zero-dimensional materials (0D), one-dimensional materials (1D), two-dimensional materials (2D), and three dimensional materials (3D). Materials that are 0D have all of their dimensions within the nanoscale range and include quantum dots and nanoparticles. Nanorods, nanowires, or nanotubes can be considered 1D, and all of their dimensions are in the nanoscale range except for one dimension. Alternatively, 2D materials only have one dimension in the nanoscale range, whereas all of the other dimensions are outside of this scale. Finally, 3D materials do not have any

of their dimensions within the nanoscale, and these include core shells or bundles of nanotubes or nanowires.

Numerous approaches have been employed in the isolation of low-dimensional materials given their wide versatility. These methods have been generally classified in two general directions including the top-down or bottom-up approach. The top-down approach involves taking bulk material and disassociating it into its corresponding nanomaterial. Mechanical and chemical exfoliation approaches are both very common top-down approaches that have been used to delaminate bulk materials, particularly layered materials, into their nanostructures. For example, the remarkable discovery of graphene was accomplished using mechanical exfoliation via scotch tape, whereas chemical exfoliation techniques have been used for a number of materials such as transition metal chalcogenides, perovskites, metal borides, etc.[4,5,6,7] In addition, mechanical milling has also been used extensively as a top-down approach to synthesize a range of nanomaterials.[8,9]

Alternatively, the bottom-up approach involves direct elements or molecular precursors to isolate the corresponding nanomaterial. Like the top-down approach, a number of different methods fit under the bottom-up approach. Chemical vapor deposition (CVD) for example involves thin film deposition on a substrate using vapor-phase precursors. CVD growth has been used extensively for the synthesis of materials such as graphene, hexagonal boron nitride, and transition metal chalcogenide materials.[10,11] Hydrothermal and solvothermal techniques have also been used, which involve elemental or molecular precursors in addition to aqueous (hydrothermal) or non-aqueous (solvothermal) solvents in a closed system under high pressure. A number of materials with different morphologies have been isolated under these conditions including low-dimensional nanosheets, nanowires, nanospheres, etc.[12,13,14] In addition to these techniques, both

the solid state and chemical vapor transport methods have also been used, both of which will be described more in-depth later in this chapter.

While the study of nanomaterials has attracted significant interest for their unique properties, it was the remarkable discovery of graphene in 2004 that caused a renaissance of interest in low-dimensional layered materials specifically.[4] Graphene has exhibited exceptional properties such as immense current density, high carrier mobility, large thermal conductivity, and incredible strength, in addition to a number of other distinctive properties.[15] While graphene is undoubtedly a remarkable material, one of its greatest setbacks is its lack of an electronic bandgap. As a result, many researchers have examined ways in modifying graphene to introduce a bandgap while still preserving its underlying properties. Furthermore, workers in the field have devoted special attention to other 2D layered materials that are similar to graphene such as hexagonal boron nitride, "Xenes" (silicene, phosphorene, germanene, etc.), black phosphorus, and transition metal dichalcogenides.[16] In this dissertation, we focus on the chemistry of low-dimensional layered materials including both 2D transition metal dichalcogenides and quasi-1D transition metal trichalcogenides.

Transition Metal Dichalcogenides

The transition metal dichalcogenides (TMDs) are a class of two-dimensional (2D) layered materials with a MX_2 composition where M is a transition metal and X is a chalcogen (S, Se, or Te). The transition metal is coordinated to six chalcogen atoms in a MX_6 arrangement which can either be in trigonal prismatic (1*H*) or octahedral (1*T*) geometries as shown in Figure 1.1.The transition metal is sandwiched between the chalcogen atoms which are covalently bound throughout the crystalline plane forming a 2D layer. The 2D layers in the TMDs are held together

by much weaker van der Waals forces (in the van der Waals gap) making them susceptible by different means of exfoliation and delamination. The TMDs are also well known for their versatile band gaps, rich polymorphism, and in many cases unique properties such as CDW transitions and superconductivity.[17,18,19,20]

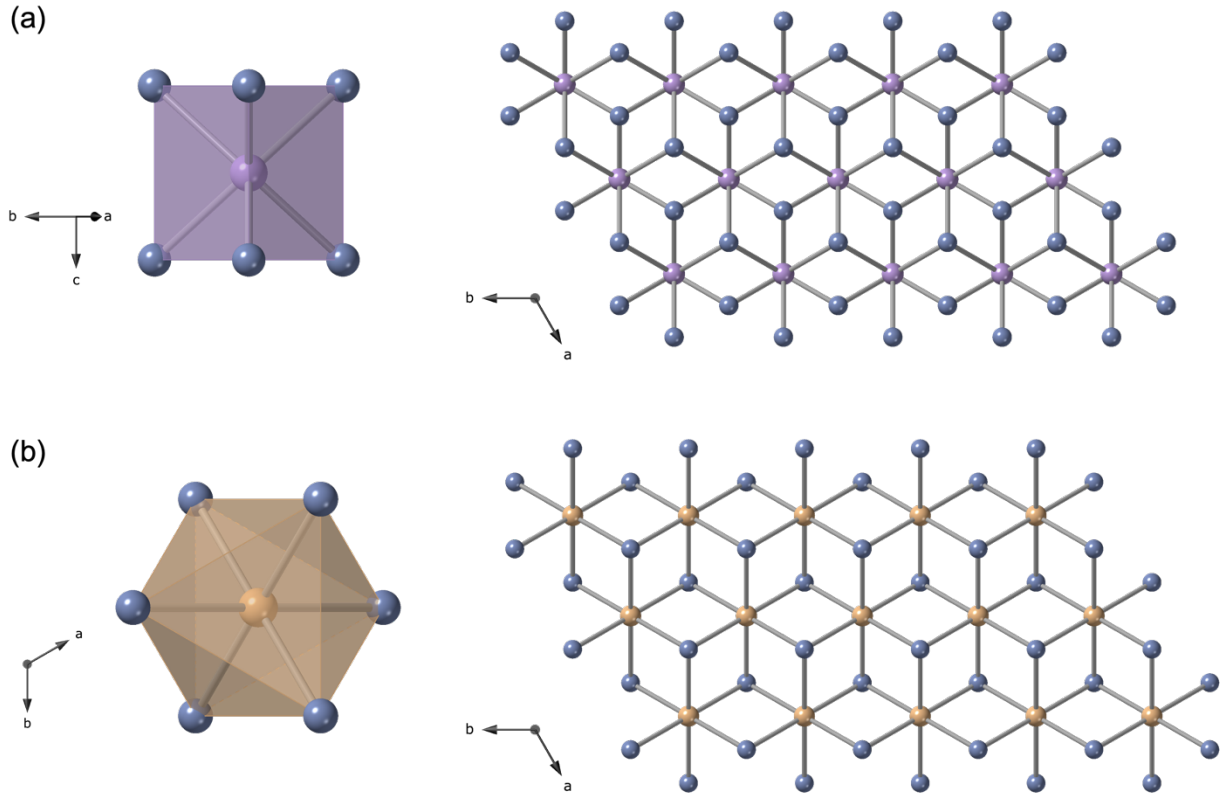

Figure 1.1 Crystal structures of TMDs in the (a) trigonal prismatic and (b) octahedral coordination's.

The various polymorphs in TMDs are denoted using a number-letter nomenclature (e.g. 1*T*, 3*R*, etc.) based on the materials unit cell where the integer represents the formula units present and the letter represents the symmetry (*H* = hexagonal, *R* = rhombohedral, and *C* = cubic). This nomenclature also extends to phases such as the 1*T* structure that exhibit distorted structures

written as 1*T*′, 1*T*″, or 1*T*‴. Furthermore, varying polymorphs can result in different stacking orders as seen in the placement of the metal and chalcogen in the stacked atomic layers. $TaSe_2$ shows a number of different polymorphic phases including, but not limited to the 1*T*, 2*H*, 3*R*, 4*H*, and 6*R* phases as illustrated in Figure 1.2. The 1*T* polymorph is unique in that is the only polymorph of $TaSe_2$ that only has an octahedral coordination, whereas the $4H_b$ and 6*R* phases show alternating geometries in each layer.[21]

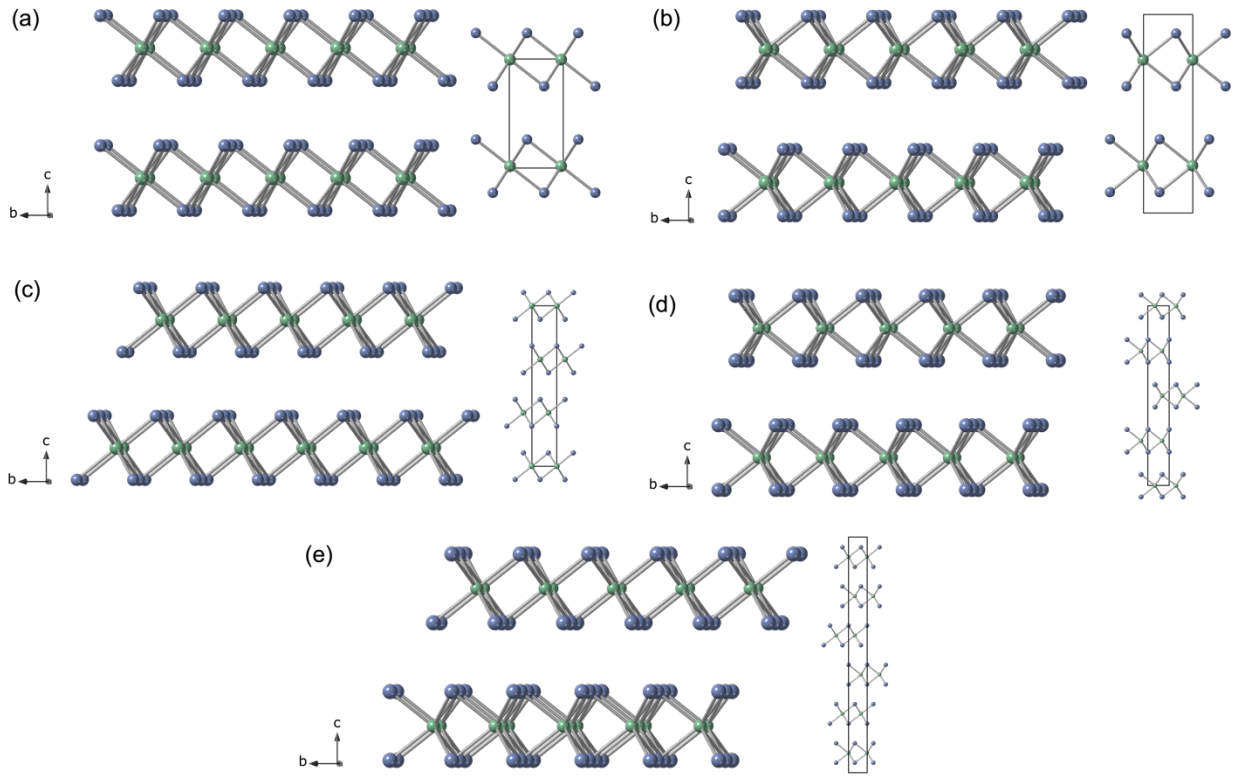

Figure 1.2 Crystal structures of layered (a) 1*T*, (b) 2*H*, (c) 3*R*, (d) 4*H*, and (e) 6*R* $TaSe_2$ from the viewpoint of the *a* axis and their corresponding unit cells illustrated within the black boxes.

In addition to polymorphism, the TMDs also exhibit a wide range of band gaps, and in many cases, they are directly related. The group IV TMDs exist in the 1*T* phase and vary from

metallic (TiS_2, $TiSe_2$, and $TiTe_2$), semiconducting (ZrS_2, $ZrSe_2$, HfS_2, $HfSe_2$), or semimetallic ($ZrTe_2$ and $HfTe_2$), although they are all in an octahedral coordination. In general, the group V TMDs generally exist in either the 1*T* or 2*H* phases (or often both) and frequently exhibit metallic behavior.[20,22,23] Group VI TMDs of MoX_2 and WX_2 generally have been isolated in 1*T* or 2*H* phases, with $MoTe_2$ being isolated in the 2*H* or 1*T*′ phases, and WTe_2 in the 1*T*′ phase. MoS_2 specifically has shown to be metallic in its 1*T* phase, a semiconductor in its 2*H* phase, and a non-centrosymmetric semiconductor in its 3*R* phase.[24,25,26] Semiconducting behavior has been found in the 2*H* phase group VI TMDs, whereas metallicity has been found for the 1*T* and 1*T*′ phases of these materials, except for 1*T*′-WTe_2 which shows semimetallicity.[23,27]

In addition to their versatile band gaps, the TMDs have been well reported to exhibit both CDW transitions and superconductivity. 1*T*-TaS_2 for example has been shown to exhibit multiple CDW transitions at 600 K, 350 K, and 180 K.[28] Alternatively, 2*H*-TaS_2 has a CDW transition at 75 K in addition to the evidence of superconductivity at 0.8 K.[29] Some studies have also examined the exfoliation of these materials and the change in their underlying properties. Thin flakes of 1*T*-TaS_2 were studied in which CDW transitions were ultimately suppressed upon delamination, whereas the superconductivity temperature in 2*H*-TaS_2 increases from 0.5 to 2.2 K upon layer minimization.[30,31] The various polymorphs of $TaSe_2$ also exhibit different properties as their polymorphs change. 1*T*-$TaSe_2$ shows CDW transitions at 600 K and 473 K, whereas 2*H*-$TaSe_2$ shows a transition at 122.3 K which was confirmed using neutron scattering.[29,32,33] Neutron scattering has also been used to confirm a CDW transition at 33.5 K in 2*H*-$NbSe_2$.[33] Further studies have also examined the coexistence of CDW transition and superconductivity in 2*H*-$NbSe_2$, which has been shown to have a superconductive state at 7.2 K.[34] The tunability of CDW transition temperature has been reported in 2*H*-$NbSe_2$ also, specifically by going from the bulk to the

monolayer which exhibited a transition temperature at 145 K.[35] Increased CDW transition temperature from the bulk to monolayer has also been seen in 1*T*-$TiSe_2$, which shows a transition temperature at 202 K in the bulk, and a transition temperature at 232 K in its monolayer form.[36,37]

The exfoliation of the TMDs and the corresponding change in properties has drawn significant interest in ways of delaminating these materials, which is easily accomplished due the weak van der Waals interactions holding these layers together. While mechanical exfoliation can be accomplished simply with scotch tape, this method is not scalable, with particular interest focusing on chemical exfoliation methods. These materials are easily exfoliated in mediums such as organic solvents or surfactant solutions, both of which have been explored in depth and shown to be scalable.[4,38] In addition, Li intercalation has also been examined in detail for the exfoliation of these materials. Many reports have used n-butyllithium to intercalate Li in the van der Waals gap of the corresponding TMD material and then adding water which generates H_2 gas thereby expanding the space between the layers and ultimately delaminating them.[12,39,40,41] This method of exfoliation has been particularly interesting due to prospects of phase engineering. For example, MoS_2 and WS_2 have been shown to undergo a phase transition ($2H \rightarrow 1T$) upon the use of Li intercalation and exfoliation techniques.[40,41] In addition to the use of Li intercalation, there are also reports of the use of other alkali metals such as Na, K, and ammonium ions to induce phase transitions in MoS_2 and WS_2.[42,43,44,45]

Transition Metal Trichalcogenides

Similar to the TMDs, the transition metal trichalcogenides (TMTs) are a broad class of layered van der Waals materials, although they are considered to be quasi-one-dimensional (quasi-1D) in nature versus the 2D TMDs. The TMTs have an MX_3 composition, where M is typically a

group IV or V transition metal and X is a chalcogen (S, Se, or Te). In addition to the group IV and V transition metals, there are reports of group VI TMTs that are amorphous including MoS_3, $MoSe_3$, WS_3, and WSe_3.[46] The crystalline TMTs instead are organized in infinitely long chains assembled from MX_6 triangular prisms that are covalently bonded down the *b* crystalline lattice. Unlike the TMDs, the TMTs only have trigonal prismatic geometries. In addition, there are weaker interchain covalent bonds that particularly define the TMTs as quasi-1D, versus true 1D materials such as Sb_2S_3, Bi_2S_3, or V_2Se_9 that only contain covalent bonds in the directions of their atomic chains.[47,48,49,50] These covalently bonded layers are held together by weak van der Waals interactions (in the van der Waals gap) which makes these materials prone to mechanical or chemical exfoliation. The crystal structure of $HfTe_3$, a TMT, is illustrated in Figure 1.3, where the infinitely long trigonal prismatic chains are illustrated, in addition to the van der Waals gap.

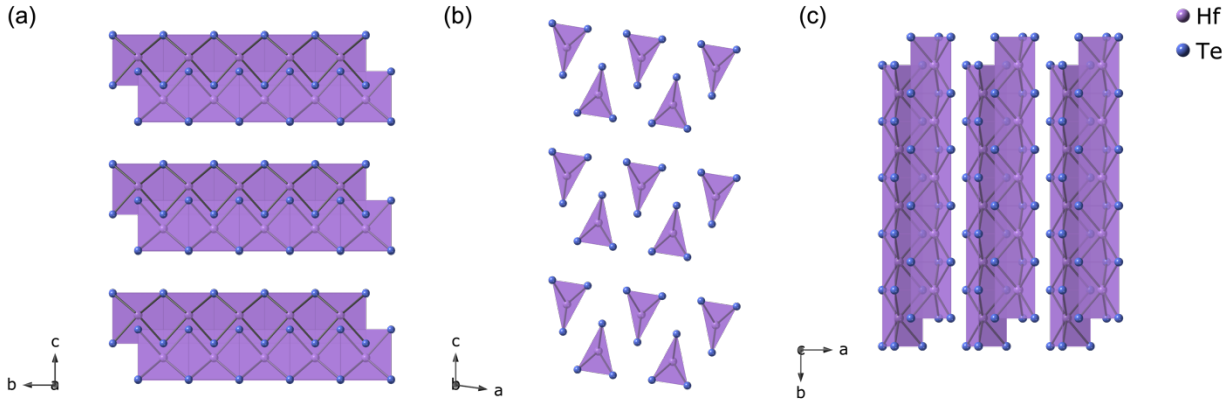

Figure 1.3 Crystal structure of $HfTe_3$ along the (a) *a*, (b) *b*, and (c) *c* axes.

The TMTs can be classified into three different structure types, including $ZrSe_3$-, $TaSe_3$-, and $NbSe_3$-type. The different chain types are differentiated by the number of different chains that are present in the structure, and the nomenclature is assigned to the first structure that was

discovered to have that particular chain arrangement. More specifically, the different chain types are assigned based on the different X–X bond lengths present. For $ZrSe_3$-type, only one chain type is present, and the majority of TMT materials belong to this type including TiS_3, ZrS_3, $ZrSe_3$, $ZrTe_3$, HfS_3, $HfSe_3$, $HfTe_3$, and NbS_3.[51,52,53] Using x-ray photoelectron spectroscopy (XPS), it was confirmed that the formula for TMTs with this chain type was $M^{4+}(X_2)^{2-}X^{2-}$.[54,55,56] The $TaSe_3$-type has two chain types present, in which the original structure was found to have two different Se–Se lengths present (2.58 Å and 2.91 Å).[57] Presently, $TaSe_3$ is the only material known to have two different chain types. The $NbSe_3$-type has three chain types present, with only $NbSe_3$ and TaS_3 belonging to this group.[58,59] The original structure of $NbSe_3$ was reported to have three different Se–Se distances of 2.37 Å, 2.48 Å, and 2.91 Å, making this chain type the most complex overall.[58] The crystal structures of $ZrSe_3$, $TaSe_3$, and $NbSe_3$ are provided in Figure 1.4.

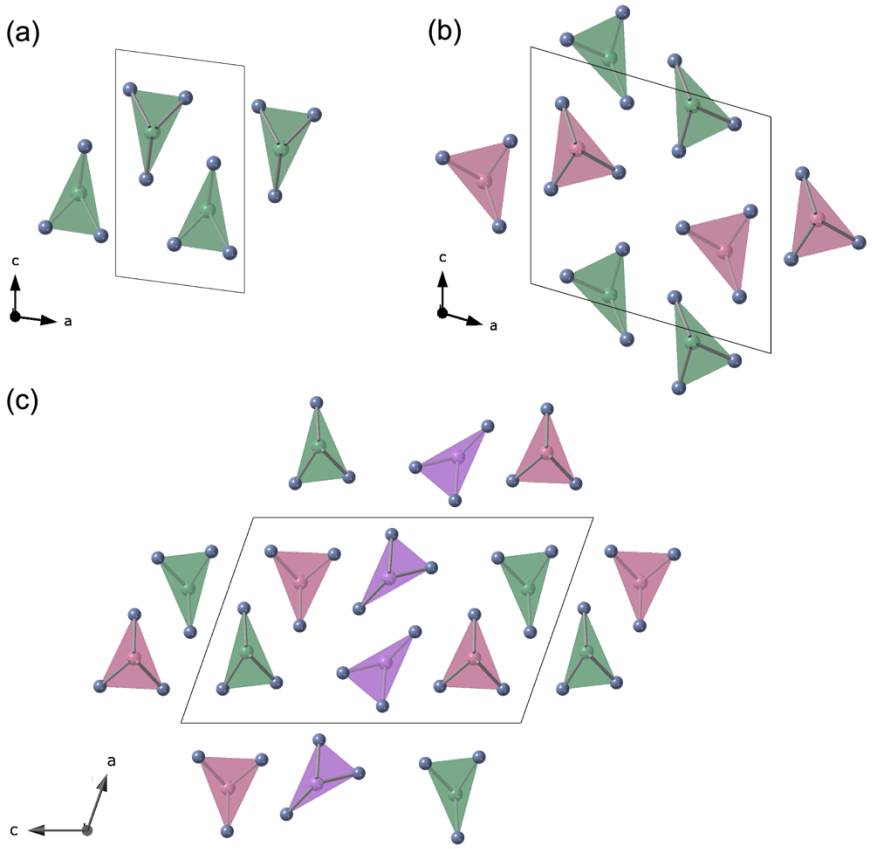

Figure 1.4 Crystal structures of (a) $ZrSe_3$, (b) $TaSe_3$, and (c) $NbSe_3$. The different chain types in each structure are color coded, and the unit cells of each structure are illustrated in the black boxes.

The TMTs are especially known for their anisotropic character defined by their trigonal prismatic chains down the *b* axis, versatile band gaps, and in some cases, CDW properties and superconductive states. All of the group IV TMTs crystallize in a monoclinic structure, with TiS_3, ZrS_3, $ZrSe_3$, HfS_3, and $HfSe_3$ exhibiting semiconducting behavior. Alternatively, $ZrTe_3$ is semi-metallic, whereas $HfTe_3$ is a narrow-gap semiconductor. [60] Both materials exhibit CDW transitions and superconducting states, and remarkably, they are the only two TMTs to exhibit both properties without chemical or physical modification.[61,62,63,64] More specifically, $ZrTe_3$ shows a superconductivity transition at 2.0 K and a CDW transition temperature at 63 K.[61,62]

Polycrystalline $HfTe_3$ has been reported to have a superconductivity transition at 1.4 K and a CDW transition temperature at 82 K, whereas single crystalline $HfTe_3$ has a reported CDW transition temperature at 93 K.[63,64]

The group V TMTs include NbS_3, $NbSe_3$, TaS_3, and $TaSe_3$. Both $NbSe_3$ and $TaSe_3$ are monoclinic, metallic, and either show CDW transitions or superconductive states. More specifically, $NbSe_3$ has reported CDW transitions at 145 K and 59 K, whereas $TaSe_3$ has shown superconductivity at 2.1 K. [65,66,67] Both TaS_3 and NbS_3 are unique in that they both exhibit polymorphism, and as a result exhibit different electronic properties. TaS_3 has two known structures referred to as monoclinic TaS_3 (m-TaS_3) and orthorhombic TaS_3 (o-TaS_3), both of which are metallic and show different CDW transition temperatures.[68,69,70] The o-TaS_3 polymorph has shown a CDW transition below 210 K, versus the m-TaS_3 polymorph showing two CDW transitions below 240 K and 160 K.[70]

Of particular interest is NbS_3 which exhibits the richest polymorphism out of all TMT materials. In total, seven different reported polymorphs have been reported which are denoted using a roman numeral system ($NbS_{3\text{-I}}$, $NbS_{3\text{-II}}$, etc.) except for the high pressure phase which is written as $NbS_{3\text{-HP}}$.[71,72,73,74,75,76] $NbS_{3\text{-I}}$ has been shown to exhibit semiconducting properties as a result of Nb atom bond pairing, versus $NbS_{3\text{-II}}$ which is metallic and has three different CDW transitions at 360 K, 150 K, and 620–650 K.[77,78,79] Furthermore, $NbS_{3\text{-III}}$ is reported to have a CDW transition at 155 K as evidenced by a phase transition and subsequent semiconducting behavior.[73]

Although the TMTs have many different compositions and in some cases exhibit polymorphism, the presence of a van der Waals gap making them susceptible to exfoliation remains a common factor. Numerous reports have examined both the mechanical and chemical exfoliation of TMT materials into various morphologies reported as whiskers, nanowires,

nanoribbons, etc.[80,81,82,83,84,85] Typically, mechanical exfoliation is easily performed using scotch tape, but this method is not scalable. Alternatively, chemical exfoliation can be used in different capacities, such as by dispersing bulk TMT material in an organic solvent followed by sonication.[82,85] Many approaches have built off of this method of exfoliation and studied colloidal solutions of TMT materials which has led into subsequent studies of resulting particle size and stability studies.[86,87] One report found the use of n-butyllithium in combination with various TMTs resulted in the compounds Li_3MX_3 which may be an alternative approach to further exfoliation studies of these materials.[88] Exfoliation of TMTs has been especially insightful into their underlying properties and in the study of device fabrication. Few-layered TiS_3 nanoribbons have been studied for the fabrication of field effect transistors in which high photoresponses and field-effect mobilities have been reported.[84,89] Furthermore, there have been reports of ultrahigh current densities for $TaSe_3$ nanowires (~10 MA/cm^2) and $ZrTe_3$ nanoribbons (~100 MA/cm^2), both of which are exponentially higher than elemental copper (2-3 MA/cm^2).[80,81,82,85]

Synthetic Approaches

A number of synthetic techniques have been reported in the literature for the synthesis and isolation of transition metal chalcogenide materials. These include but are not limited to the solid state route, chemical vapor transport (CVT), hydrothermal synthesis, melt flux, and chemical vapor deposition growth.[11,12,90,91]

From these methods, both the solid state and CVT approaches are commonly employed to isolate either polycrystalline or single crystalline transition metal chalcogenides. In both routes, quartz ampules are employed by loading starting materials which are subsequently flame sealed under vacuum creating a closed system. Carbon-coated quartz ampules may also be used to prevent

oxidation, which can be especially useful when using transition metals that have a high affinity for oxygen.[92,93,94]

The solid state approach is commonly completed by loading a quartz ampule with elemental precursors followed by subsequent heating resulting in polycrystalline product. Alternatively, the CVT approach is used for single crystalline isolation and also involves the use of elemental precursors, although there are reports in which the polycrystalline analog of the desired product is used.[95,96,97,98] A transport agent is also placed in the ampule to facilitate single crystalline growth. Examples include halogens (I_2, Br_2, or Cl_2), transition metal halides ($MoCl_5$, $TaCl_5$, etc.), chalcogen halides ($SeCl_4$, $TeCl_4$, $TeBr_4$, etc.), other halide complexes (NH_4Cl, NH_4I, etc.), or excess chalcogen (S, Se, or Te).[97,99,100,101,102,103,104] I_2 mediated transport is one of the most common transport agents used, although the versatility in transport agent selection has been well presented in the literature. Choice in transport agent has also been shown to directly affect the sizes of crystals grown and their subsequent morphologies.[100,101] Furthermore, a recent report found that using NH_4Cl transport resulted in a new polymorph of NbS_3, which was described as the first time a transport agent has directly led to a product's atomic structure.[75] It should be noted that while they are critical for crystal growth, there are reports that transport agents can cause chemical impurities in desired products.[36,105,106] The general mechanism for I_2 transport in a TMD synthesis can be represented in Equations 1.1 and 1.2 below:[107]

$$M + 2\ I_2 \rightarrow MI_4 \quad (1.1)$$

$$MI_4 + 2\ X \rightarrow MX_2 + 2\ I_2 \quad (1.2)$$

The transition metal is represented by "M" which reacts with I_2 forming a volatile metal halide intermediate "MI_4". This intermediate then reacts with the chalcogen "X" resulting in formation of the desired "MX_2" composition and I_2 which continues the reaction cycle. It should

be noted that in addition to transport agent choice, a temperature gradient also needs to be chosen to facilitate crystal growth. In a typical experiment, a furnace has two zones which are at different temperatures. The hotter zone of the furnace is termed the "source zone", whereas the colder zone is termed the "growth zone". Generally, the side of the ampule with the starting materials is placed in the source zone where formation of the volatile gaseous species occurs. The gaseous species then transports to the colder growth zone resulting in crystal deposition and release of the transport agent. Temperature gradients have varied widely in previous reports, allowing researchers the versatility to tune this parameter and enhance circulation of solid-gaseous-solid species in the closed system.[108] One report found that smaller gradients resulted in smaller crystals and less yield, but, with crystals of overall higher quality when studying the crystal growth of the TMTs.[109] Finally, for both CVT and solid state syntheses, various cooling methods may be used to enhance crystal growth and assist in phase isolation, including immediate water quenching and controlled slow-cooling approaches.[21,63,109]

Research Goals

The work described in this dissertation further expands our understanding in group IV transition metal chalcogenide materials. We take a special initiative in further developing synthetic pathways in isolating transition metal di- and trichalcogenide materials and their related solid solutions.

In Chapter II, we consider the synthesis of both polycrystalline and single crystalline $HfTe_3$. While synthetic routes have been reported for both in the literature, these reports have been very limited, especially compared to other known TMTs. Furthermore, there have been contradictions into the ideal reaction conditions.[63,64] In this chapter we provide a thorough

investigation into isolating both polycrystalline and single crystalline $HfTe_3$ that we hope will further expand the accessibility to workers in the field who are interested in isolating this material. When isolating polycrystalline $HfTe_3$, we found that choice in Hf metal source (foil vs powder) could affect the final product, in addition to variations in the cooling choice (natural cooling, controlled slow-cooling, or immediate water quenching). For single crystalline growth, we found it was necessary to use polycrystalline $HfTe_3$ as a precursor under CVT conditions, and that elemental precursors were inadequate for phase isolation. We also determined that different transport agents (I_2, NH_4Cl, or $TeBr_4$) led to changes in crystal growth and overall morphology. Through all of these syntheses, we took initiative in minimizing neighboring phases ($HfTe_2$ and $HfTe_5$) which were significantly more thermodynamically stable than our target $HfTe_3$ phase. Our work indicated that choice in temperature and elimination of the temperature gradient were critical to phase isolation. We also took measures to avoid oxidation such as using carbon-coated ampules, ball-milling under Ar atmosphere, and handling materials under air-free conditions.

Chapter III of this dissertation relied heavily on our synthetic studies with $HfTe_3$, and more specifically examines the isolation of $Hf_xZr_{1-x}Te_3$ solid solutions. We found that we could isolate $Hf_xZr_{1-x}Te_3$ solid solutions across a wide temperature range from 750–530 °C. Furthermore, we determined that leveraging the chemistry of $HfTe_3$ and $ZrTe_3$ was critical for appropriate phase isolation, especially as we increased the Hf percentage. We hypothesize this is important because the synthetic conditions for single crystalline $HfTe_3$ are more sensitive in regard to starting materials, reaction temperature, temperature gradient, etc. Similar to $HfTe_3$, we implemented similar synthetic parameters and experimental precautions to avoid the presence of neighboring phases and oxidation. We also used both single crystal x-ray diffraction and x-ray photoelectron

spectroscopy (XPS) to further elucidate the crystal structure and bonding environments of $Hf_{0.80}Zr_{0.20}Te_3$ solid solutions, especially as a function of metal alloying.

This chapter also briefly examines synthetic attempts at the isolation of $Ti_xZr_{1-x}Te_3$ and $Ti_xHf_{1-x}Te_3$ solid solutions. We were motivated by a recent report which $TiTe_3$ chains were isolated in multiwalled carbon nanotubes, the only current report of $TiTe_3$ isolation.[110] Our work focused on leveraging the favored synthetic conditions of $ZrTe_3$ and $HfTe_3$ and attempting the incorporation of Ti into these materials. We determined that we could only incorporate a miniscule percentage (~ 2%) of Ti into $ZrTe_3$ and that crystal growth was very minimal. Furthermore, additional attempts resulted in the ditelluride phases, as did attempts with Ti incorporation into $HfTe_3$.

In Chapter IV, we expand our synthetic approaches and examine solid solutions of group IV TMDs. We were able to isolate single crystals of $Ti_xZr_{1-x}Te_2$, $Ti_xHf_{1-x}Te_2$, and $Ti_xZr_{1-x}Se_2$ solid solutions via the CVT approach. Similar to $Hf_xZr_{1-x}Te_3$ solid solutions, we determined it was important to leverage the favored synthetic conditions of $TiTe_2$, $ZrTe_2$, and $HfTe_2$ to isolate solid solutions of $Ti_xZr_{1-x}Te_2$ and $Ti_xHf_{1-x}Te_2$. To our advantage, the temperature range in which these solid solutions were favored were within a smaller temperature range (875–825 °C), and the presence of neighboring phases was significantly of less concern. We also implemented single crystal x-ray diffraction for both $Ti_{0.50}Zr_{0.50}Te_2$ and $Ti_{0.25}Hf_{0.75}Te_2$ which further elucidated their structures. Finally, we examined solid solutions of $Ti_xZr_{1-x}Se_2$ which we isolated across the temperature gradient of 900–870 °C. Our interest in this material was heavily motivated by a computational report in which the presence of CDW transitions in $Ti_{0.50}Zr_{0.50}Se_2$ were predicted.[111]

References

1. Baig, N.; Kammakakam, I.; Falath, W. Nanomaterials: A Review of Synthesis Methods, Properties, Recent Progress, and Challenges. *Mater. Adv.* **2021**, *2*, 1821-1871.

2. Roduner, E. Size Matters: Why Nanomaterials Are Different. *Chem. Soc. Rev.* **2006**, *35*, 583-592.

3. Sardar, R.; Funston, A.; Mulvaney, P.; Murray, R. Gold Nanoparticles: Past, Present, and Future. *Langmuir* **2009**, *25*, 13840-13851.

4. Coleman, J.; Lotya, M.; O'Neill, A.; Bergin, S.; King, P.; Khan, U.; Young, K.; Gaucher, A.; De, S.; Smith, R.; Shvets, I.; Arora, S.; Stanton, G.; Kim, H.; Lee, K.; Kim, G.; Duesberg, G.; Hallam, T.; Boland, J.; Wang, J.; Donegan, J.; Grunlan, J.; Moriarty, G.; Shmeliov, A.; Nicholls, R.; Perkins, J.; Grieveson, E.; Theuwissen, K.; McComb, D.; Nellist, P.; Nicolosi, V. Two-Dimensional Nanosheets Produced by Liquid Exfoliation of Layered Materials. *Science* **2011**, *331*, 568-571.

5. Hintermayr, V.; Richter, A.; Ehrat, F.; Döblinger, M.; Vanderlinden, W.; Sichert, J.; Tong, Y.; Polavarapu, L.; Feldmann, J.; Urban, A. Tuning the Optical Properties of Perovskite Nanoplatelets Through Composition and Thickness by Ligand-Assisted Exfoliation. *Adv. Mater.* **2016**, *28*, 9478-9485.

6. Novoselov, K.; Geim, A.; Morozov, S.; Jiang, D.; Zhang, Y.; Dubonos, S.; Grigorieva, I.; Firsov, A. Electric Field Effect in Atomically Thin Carbon Films. *Science* **2004**, *306*, 666-669.

7. James, A.; Jasuja, K. Chelation Assisted Exfoliation of Layered Borides Towards Synthesizing Boron Based Nanosheets. *RSC Adv.* **2017**, *7*, 1905-1914.

8. Choi, Y.; Baik, N. Fabrication of Nano-Sized $Ba_xMg_{1-x}Fe_2O_4$ Ferrite Powders by Using Self-Propagating High Temperature Synthesis Reaction and Mechanical Milling. *J. Alloys Compd.* **2009**, *480*, 134-137.

9. Widatallah, H.; Johnson, C.; Gismelseed, A.; Al-Omari, I.; Stewart, S.; Al-Harthi, S.; Thomas, S.; Sitepu, H. Structural and Magnetic Studies of Nanocrystalline Mg-Doped $Li_{0.5}Fe_{2.5}O_4$ Particles Prepared by Mechanical Milling. *J. Phys. D: Appl. Phys.* **2008**, *41*, 165006.

10. Wang, M.; Jang, S.; Jang, W.; Kim, M.; Park, S.; Kim, S.; Kahng, S.; Choi, J.; Ruoff, R.; Song, Y.; Lee, S. A Platform for Large-Scale Graphene Electronics - CVD Growth of Single-Layer Graphene on CVD-Grown Hexagonal Boron Nitride. *Adv. Mater.* **2013**, *25*, 2746-2752.

11. van der Zande, A.; Huang, P.; Chenet, D.; Berkelbach, T.; You, Y.; Lee, G.; Heinz, T.; Reichman, D.; Muller, D.; Hone, J. Grains and Grain Boundaries in Highly Crystalline Monolayer Molybdenum Disulphide. *Nature Mater.* **2013**, *12*, 554-561.

12. Matte, H.; Plowman, B.; Datta, R.; Rao, C. Graphene Analogues of Layered Metal Selenides. *Dalton Trans.* **2011**, *40*, 10322.

13. Dong, Y.; Du, X.; Liang, P.; Man, X. One-Pot Solvothermal Method To Fabricate 1D-VS_4 Nanowires as Anode Materials for Lithium Ion Batteries. *Inorg. Chem. Commun.* **2020**, *115*, 107883.

14. Jiang, Y.; Peng, Z.; Zhang, S.; Li, F.; Liu, Z.; Zhang, J.; Liu, Y.; Wang, K. Facile In-Situ Solvothermal Method to Synthesize Double Shell $ZnIn_2S_4$ Nanosheets/TiO_2 Hollow Nanosphere with Enhanced Photocatalytic Activities. *Ceram. Int.* **2018**, *44*, 6115-6126.

15. Geim, A. Graphene: Status and Prospects. *Science* **2009**, *324*, 1530-1534.

16. Zhang, W.; Wang, Q.; Chen, Y.; Wang, Z.; Wee, A. van der Waals Stacked 2D Layered Materials For Optoelectronics. *2D Materials* **2016**, *3*, 022001.

17. Butler, S.; Hollen, S.; Cao, L.; Cui, Y.; Gupta, J.; Gutiérrez, H.; Heinz, T.; Hong, S.; Huang, J.; Ismach, A.; Johnston-Halperin, E.; Kuno, M.; Plashnitsa, V.; Robinson, R.; Ruoff, R.; Salahuddin, S.; Shan, J.; Shi, L.; Spencer, M.; Terrones, M.; Windl, W.; Goldberger, J. Progress, Challenges, and Opportunities in Two-Dimensional Materials Beyond Graphene. *ACS Nano* **2013**, *7*, 2898-2926.

18. Su, J.; Liu, K.; Wang, F.; Jin, B.; Guo, Y.; Liu, G.; Li, H.; Zhai, T. van der Waals 2D Transition Metal Tellurides. *Adv. Mater. Interfaces* **2019**, *6*, 1900741.

19. Manzeli, S.; Ovchinnikov, D.; Pasquier, D.; Yazyev, O.; Kis, A. 2D Transition Metal Dichalcogenides. *Nat. Rev. Mater.* **2017**, *2*, 17033.

20. Wang, Q.; Kalantar-Zadeh, K.; Kis, A.; Coleman, J.; Strano, M. Electronics and Optoelectronics of Two-Dimensional Transition Metal Dichalcogenides. *Nat. Nanotech.* **2012**, *7*, 699-712.

21. Hayashi, K.; Kawamura, A. Formation Of $TaSe_2$ Polytypes and Hydrogen Impurity. *Mater. Res. Bull.* **1987**, *22*, 11-18.

22. Wang, X.; Song, Z.; Wen, W.; Liu, H.; Wu, J.; Dang, C.; Hossain, M.; Iqbal, M.; Xie, L. Potential 2D Materials with Phase Transitions: Structure, Synthesis, and Device Applications. *Adv. Mater.* **2018**, *31*, 1804682.

23. Xiao, Y.; Zhou, M.; Liu, J.; Xu, J.; Fu, L. Phase Engineering of Two-Dimensional Transition Metal Dichalcogenides. *Sci. China Mater.* **2019**, *62*, 759-775.

24. Lukowski, M.; Daniel, A.; Meng, F.; Forticaux, A.; Li, L.; Jin, S. Enhanced Hydrogen Evolution Catalysis from Chemically Exfoliated Metallic MoS_2 Nanosheets. *J. Am. Chem. Soc.* **2013**, *135*, 10274-10277.

25. Lembke, D.; Bertolazzi, S.; Kis, A. Single-Layer MoS_2 Electronics. *Acc. Chem. Res.* **2015**, *48*, 100-110.

26. Shi, J.; Yu, P.; Liu, F.; He, P.; Wang, R.; Qin, L.; Zhou, J.; Li, X.; Zhou, J.; Sui, X.; Zhang, S.; Zhang, Y.; Zhang, Q.; Sum, T.; Qiu, X.; Liu, Z.; Liu, X. 3R MoS_2 with Broken Inversion Symmetry: A Promising Ultrathin Nonlinear Optical Device. *Adv. Mater.* **2017**, *29*, 1701486.

27. Song, Y.; Jia, Z.; Zhang, D.; Zhu, X.; Shi, Z.; Wang, H.; Zhu, L.; Yuan, Q.; Zhang, H.; Xing, D.; Li, S. Observation of Coulomb Gap in the Quantum Spin Hall Candidate Single-Layer 1T'-WTe_2. *Nat. Commun.* **2018**, *9*, 4071.

28. Di Salvo, F.; Rice, T. Charge-Density Waves In Transition-Metal Compounds. *Phys. Today* **1979**, *32*, 32-38.

29. Motizuki, K. Structural Phase Transitions in Layered Transition Metal Compounds, Springer International Publishing AG, Basel, Switzerland **1986**.

30. Yu, Y.; Yang, F.; Lu, X.; Yan, Y.; Cho, Y.; Ma, L.; Niu, X.; Kim, S.; Son, Y.; Feng, D.; Li, S.; Cheong, S.; Chen, X.; Zhang, Y. Gate-Tunable Phase Transitions in Thin Flakes of 1T-TaS_2. *Nature Nanotech.* **2015**, *10*, 270-276.

31. Navarro-Moratalla, E.; Island, J.; Mañas-Valero, S.; Pinilla-Cienfuegos, E.; Castellanos-Gomez, A.; Quereda, J.; Rubio-Bollinger, G.; Chirolli, L.; Silva-Guillén, J.; Agraït, N.; Steele, G.; Guinea, F.; van der Zant, H.; Coronado, E. Enhanced Superconductivity in Atomically Thin TaS_2. *Nat. Commun.* **2016**, *7*, 11043.

32. Wilson, J.; Di Salvo, F.; Mahajan, S. Charge-Density Waves in Metallic, Layered, Transition-Metal Dichalcogenides. *Phys. Rev. Lett.* **1974**, *32*, 882-885.

33. Moncton, D.; Axe, J.; DiSalvo, F. Study of Superlattice Formation in 2*H*-$NbSe_2$ and 2*H*-$TaSe_2$ by Neutron Scattering. *Phys. Rev. Lett.* **1975**, *34*, 734-737.

34. Morris, R. Connection Between Charge-Density Waves and Superconductivity in $NbSe_2$. *Phys. Rev. Lett.* **1975**, *34*, 1164-1166.

35. Xi, X.; Zhao, L.; Wang, Z.; Berger, H.; Forró, L.; Shan, J.; Mak, K. Strongly Enhanced Charge-Density-Wave Order in Monolayer $NbSe_2$. *Nature Nanotech.* **2015**, *10*, 765-769.

36. Di Salvo, F. J.; Moncton, D. E.; Waszczak, J. V. Electronic Properties and Superlattice Formation in the Semimetal $TiSe_2$. *Phys. Rev. B* **1976**, *14*, 4321-4328.

37. Chen, P.; Chan, Y.; Fang, X.; Zhang, Y.; Chou, M.; Mo, S.; Hussain, Z.; Fedorov, A.; Chiang, T. Charge Density Wave Transition in Single-Layer Titanium Diselenide. *Nat. Commun.* **2015**, *6*, 8943.

38. Smith, R.; King, P.; Lotya, M.; Wirtz, C.; Khan, U.; De, S.; O'Neill, A.; Duesberg, G.; Grunlan, J.; Moriarty, G.; Chen, J.; Wang, J.; Minett, A.; Nicolosi, V.; Coleman, J. Large-Scale Exfoliation of Inorganic Layered Compounds in Aqueous Surfactant Solutions. *Adv. Mater.* **2011**, *23*, 3944-3948.

39. Joensen, P.; Frindt, R.; Morrison, S. Single-Layer MoS_2. *Mater. Res. Bull.* **1986**, *21*, 457-461.

40. Chrissafis, K.; Zamani, M.; Kambas, K.; Stoemenos, J.; Economou, N.; Samaras, I.; Julien, C. Structural Studies of MoS_2 Intercalated by Lithium. *Mater. Sci. Eng. B* **1989**, *3*, 145-151.

41. Voiry, D.; Yamaguchi, H.; Li, J.; Silva, R.; Alves, D.; Fujita, T.; Chen, M.; Asefa, T.; Shenoy, V.; Eda, G.; Chhowalla, M. Enhanced Catalytic Activity in Strained Chemically Exfoliated WS_2 Nanosheets for Hydrogen Evolution. *Nature Mater.* **2013**, *12*, 850-855.

42. Wang, X.; Shen, X.; Wang, Z.; Yu, R.; Chen, L. Atomic-Scale Clarification of Structural Transition of MoS_2 Upon Sodium Intercalation. *ACS Nano* **2014**, *8*, 11394-11400.

43. Zhang, R.; Tsai, I.; Chapman, J.; Khestanova, E.; Waters, J.; Grigorieva, I. Superconductivity in Potassium-Doped Metallic Polymorphs of MoS_2. *Nano Lett.* **2015**, *16*, 629-636.

44. Liu, Q.; Li, X.; He, Q.; Khalil, A.; Liu, D.; Xiang, T.; Wu, X.; Song, L. Gram-Scale Aqueous Synthesis of Stable Few-Layered 1T-MoS_2: Applications for Visible-Light-Driven Photocatalytic Hydrogen Evolution. *Small* **2015**, *11*, 5556-5564.

45. Liu, Q.; Li, X.; Xiao, Z.; Zhou, Y.; Chen, H.; Khalil, A.; Xiang, T.; Xu, J.; Chu, W.; Wu, X.; Yang, J.; Wang, C.; Xiong, Y.; Jin, C.; Ajayan, P.; Song, L. Stable Metallic 1T-WS_2 Nanoribbons Intercalated with Ammonia Ions: The Correlation Between Structure and Electrical/Optical Properties. *Adv. Mater.* **2015**, *27*, 4837-4844.

46. Cramer, S.; Liang, K.; Jacobson, A.; Chang, C.; Chianelli, R. EXAFS Studies of Amorphous Molybdenum and Tungsten Trisulfides and Triselenides. *Inorg. Chem.* **1984**, *23*, 1215-1221.

47. Balandin, A.A.; Kargar, F.; Salguero, T.T.; Lake, R.K. One Dimensional van der Waals Quantum Materials. *Mater. Today* **2022**, *55*, 74-91.

48. Zhou, Y.; Wang, L.; Chen, S.; Qin, S.; Liu, X.; Chen, J.; Xue, D.; Luo, M.; Cao, Y.; Cheng, Y.; Sargent, E.; Tang, J. Thin-Film Sb_2Se_3 Photovoltaics with Oriented One-Dimensional Ribbons and Benign Grain Boundaries. *Nat. Photon.* **2015**, *9*, 409-415.

49. Yang, W.; Yang, J.; Zhao, K.; Gao, Q.; Liu, L.; Zhou, Z.; Hou, S.; Wang, X.; Shen, G.; Pang, X.; Xu, Q.; Wei, Z. Low-Noise Dual-Band Polarimetric Image Sensor Based on 1D Bi_2S_3 Nanowire. *Adv. Sci.* **2021**, *8*, 2100075.

50. Oh, S.; Chae, S.; Kim, B.; Choi, K.; Jang, W.; Jang, J.; Hussain, Y.; Lee, D.; Kim, Y.; Yu, H.; Choi, J. Synthesis of a One-Dimensional Atomic Crystal of Vanadium Selenide (V_2Se_9). *RSC Adv.* **2018**, *8*, 33980-33984.

51. Brattås, L.; Kjekshus, A. On the Properties of Compounds with the $ZrSe_3$ Type Structure. *Acta Chem. Scand.* **1972**, *26*, 3441-3449.

52. Kadijk, F.; Jellinek, F. The System Niobium-Sulfur. *J. Less Common Met.* **1969**, *19*, 421-430.

53. Furuseth, S.; Brattås, L.; Kjekshus, A.; Andresen, A.; Fischer, P. On the Crystal Structures of TiS_3, ZrS_3, $ZrSe_3$, $ZrTe_3$, HfS_3, and $HfSe_3$. *Acta Chem. Scand.* **1975**, *29a*, 623-631.

54. Jellinek, F.; Pollak, R.; Shafer, M. X-Ray Photoelectron Spectra and Electronic Structure of Zirconium Trisulfide and Triselenide. *Mater. Res. Bull.* **1974**, *9*, 845-856.

55. Endo, K.; Ihara, H.; Watanabe, K.; Gonda, S. XPS Study of One-Dimensional Compounds: TiS_3. *J. Solid State Chem.* **1982**, *44*, 268-272.

56. Endo, K.; Ihara, H.; Watanabe, K.; Gonda, S. XPS Study on Valence Band Structures of Transition-Metal Trisulfides, TiS_3, NbS_3, and TaS_3. *J. Solid State Chem.* **1981**, *39*, 215-218.

57. Bjerkelund, E.; Fermor, J.; Kjekshus, A.; Wagnières, M.; Williams, D.; Bunnenberg, E.; Djerassi, C.; Records, R. On the Properties of TaS_3 And $TaSe_3$. *Acta Chem. Scand.* **1966**, *20*, 1836-1842.

58. Hodeau, J.; Marezio, M.; Roucau, C.; Ayroles, R.; Meerschaut, A.; Rouxel, J.; Monceau, P. Charge-Density Waves in $NbSe_3$ at 145K: Crystal Structures, X-Ray and Electron Diffraction Studies. *J. Phys. C Solid State Phys.* **1978**, *11*, 4117-4134.

59. Meerschaut, A.; Rouxel, J.; Haen, P.; Monceau, P.; Núñez-Regueiro, M. Obtention of a New Phase of the One-Dimensional Compound TaS_3 : X-Ray Characterization and Electrical Measurements. *J. Phys. Lett.* **1979**, *40*, 157-159.

60. Island, J.; Molina-Mendoza, A.; Barawi, M.; Biele, R.; Flores, E.; Clamagirand, J.; Ares, J.; Sánchez, C.; van der Zant, H.; D'Agosta, R.; Ferrer, I.; Castellanos-Gomez, A. Electronics and Optoelectronics of Quasi-1D Layered Transition Metal Trichalcogenides. *2D Mater.* **2017**, *4*, 022003.

61. Canadell, E.; Mathey, Y.; Whangbo, M. Band Electronic Structure Study of the Semimetallic Properties and the Anisotropic Resistivity Hump in Zirconium Tritelluride. *J. Am. Chem. Soc.* **1988**, *110*, 104-108.

62. Takahashi, S.; Sambongi, T.; Okada, S. Conduction Properties of $ZrTe_3$. *J. de Physique* **1983**, *44*, 1733-1736.

63. Denholme, S.; Yukawa, A.; Tsumura, K.; Nagao, M.; Tamura, R.; Watauchi, S.; Tanaka, I.; Takayanagi, H.; Miyakawa, N. Coexistence of Superconductivity and Charge-Density Wave in the Quasi-One-Dimensional Material $HfTe_3$. *Sci. Rep.* 2017, *7*, 45217..

64. Li, J.; Peng, J.; Zhang, S.; Chen, G. Anisotropic Multichain Nature and Filamentary Superconductivity in the Charge Density Wave System $HfTe_3$. *Phys. Rev. B* **2017**, *96*, 174510.

65. Bullett, D. Variation of Electronic Properties with Structure of Transition Metal Trichalcogenides *J. Phys. C: Solid State Phys.* **1979**, *12*, 277-281.

66. Monçeau, P.; Ong, N.; Portis, A.; Meerschaut, A.; Rouxel, J. Electric Field Breakdown of Charge-Density-Wave—Induced Anomalies in $NbSe_3$. *Phys. Rev. Lett.* **1976**, *37*, 602-606.

67. Sambongi, T.; Yamamoto, M.; Tsutsumi, K.; Shiozaki, Y.; Yamaya, K.; Abe, Y. Superconductivity In One-Dimensional $TaSe_3$. *J. Phys. Soc. Japan* **1977**, *42*, 1421-1422.

68. Meerschaut, A.; Guemas, L.; Rouxel, J. Structure and Properties of the New Phase of the Pseudo One-Dimensional Compound TaS_3. *J. Solid State Chem.* **1981**, *36*, 118-123.

69. Bjerkelund, E.; Kjekshus, A. On the Properties of TaS_3, $TaSe_3$ and $TaTe_4$. *Z. fur Anorg. Allg. Chem.* **1964**, *328*, 235-242.

70. Roucau, C.; Ayroles, R.; Monceau, P.; Guemas, L.; Meerschaut, A.; Rouxel, J. Electron Diffraction and Resistivity Measurements on the One-Dimensional Orthorhombic and Monoclinic Structures of TaS_3. Comparison With $NbSe_3$. *Phys. Stat. Sol.* **1980**, *62*, 483-493.

71. Rijnsdorp, J.; Jellinek, F. The Crystal Structure of Niobium Trisulfide, NbS_3. *J. Solid State Chem.* **1978**, *25*, 325-328.

72. Zupanič, E.; van Midden, H.; van Midden, M.; Šturm, S.; Tchernychova, E.; Pokrovskii, V.; Zybtsev, S.; Nasretdinova, V.; Zaitsev-Zotov, S.; Chen, W.; Pai, W.; Bennett, J.; Prodan, A. Basic and Charge Density Wave Modulated Structures of NbS_3-II. *Phys. Rev. B* **2018**, *98*, 174113.

73. Zettl, A.; Jackson, C.; Janossy, A.; Grüner, G.; Jacobsen, A.; Thompson, A. Charge Density Wave Transition and Nonlinear Conductivity in NbS_3. *Solid State Commun.* **1982**, *43*, 345-347.

74. Bloodgood, M.; Wei, P.; Aytan, E.; Bozhilov, K.; Balandin, A.; Salguero, T. Monoclinic Structures of Niobium Trisulfide. *APL Mater.* **2018**, *6*, 026602.

75. Bloodgood, M.; Ghafouri, Y.; Wei, P.; Salguero, T. Impact of the Chemical Vapor Transport Agent on Polymorphism in the Quasi-1D NbS_3 System. *Appl. Phys. Lett.* **2022**, *120*, 173103.

76. Kikkawa, S.; Ogawa, N.; Koizumi, M.; Onuki, Y. High-Pressure Syntheses of TaS_3, NbS_3, $TaSe_3$, and $NbSe_3$ with $NbSe_3$-Type Crystal Structure. *J. Solid State Chem.*, **1982**, *41*, 315-322.

77. Zybtsev, S.; Pokrovskii, V.; Nasretdinova, V.; Zaitsev-Zotov, S.; Pavlovskiy, V.; Odobesco, A.; Pai, W.; Chu, M.; Lin, Y.; Zupanič, E.; van Midden, H.; Šturm, S.; Tchernychova, E.; Prodan, A.; Bennett, J.; Mukhamedshin, I.; Chernysheva, O.; Menushenkov, A.; Loginov, V.; Loginov, B.; Titov, A.; Abdel-Hafiez, M. NbS_3: A Unique Quasi-One-Dimensional Conductor with Three Charge Density Wave Transitions. *Phys. Rev. B* **2017**, *95*, 039901.

78. Wang, Z.; Monceau, P.; Salva, H.; Roucau, C.; Guemas, L.; Meerschaut, A. Charge-Density-Wave Transport Above Room Temperature in a Polytype of NbS_3. *Phys. Rev. B* **1989**, *40*, 11589-11593.

79. Bullett, D. Electronic Structure and Properties of NbS_3 and Nb_3S_4. *J. Solid State Chem.* **1980**, *33*, 13-16.

80. Geremew, A.; Bloodgood, M.; Aytan, E.; Woo, B.; Corber, S.; Liu, G.; Bozhilov, K.; Salguero, T.; Rumyantsev, S.; Rao, M.; Balandin, A.A. Current Carrying Capacity of Quasi-1D $ZrTe_3$ van der Waals Nanoribbons. *IEEE Electron Device Lett.* **2018**, *39*, 735-738.

81. Geremew, A.; Rumyantsev, S.; Bloodgood, M.; Salguero, T.; Balandin, A. Unique Features of the Generation–Recombination Noise in Quasi-One-Dimensional van der Waals Nanoribbons. *Nanoscale* **2018**, *10*, 19749-19756.

82. Stolyarov, M.; Liu, G.; Bloodgood, M.; Aytan, E.; Jiang, C.; Samnakay, R.; Salguero, T.; Nika, D.; Rumyantsev, S.; Shur, M.; Bozhilov, K.; Balandin, A. Breakdown Current Density in *h*-BN-Capped Quasi-1D $TaSe_3$ Metallic Nanowires: Prospects of Interconnect Applications. *Nanoscale* **2016**, *8*, 15774-15782.

83. Gorlova, I.; Zybtsev, S.; Pokrovskii, V.; Bolotina, N.; Gavrilkin, S.; Tsvetkov, A. Magnetotransport and Power-Law *I–V* Curves of the Layered Quasi One-Dimensional Compound TiS_3. *Phys. B: Condens. Matt.* **2015**, *460*, 11-15.

84. Island, J.; Buscema, M.; Barawi, M.; Clamagirand, J.; Ares, J.; Sánchez, C.; Ferrer, I.; Steele, G.; van der Zant, H.; Castellanos-Gomez, A. Ultrahigh Photoresponse of Few-Layer TiS_3 Nanoribbon Transistors. *Adv. Opt. Mater.* **2014**, *2*, 641-645.

85. Liu, G.; Rumyantsev, S.; Bloodgood, M.; Salguero, T.; Shur, M.; Balandin, A. Low-Frequency Electronic Noise in Quasi-1D $TaSe_3$ van der Waals Nanowires. *Nano Lett.* **2016**, *17*, 377-383.

86. Poltarak, P.; Artemkina, S.; Bulavchenko, A.; Podlipskaya, T.; Fedorov, V. Colloidal Dispersions of Tantalum Trisulfide: Syntheses and Characteristics. *Russ. Chem. Bull.* **2015**, *64*, 1850-1856.

87. Fedorov, V.; Artemkina, S.; Grayfer, E.; Naumov, N.; Mironov, Y.; Bulavchenko, A.; Zaikovskii, V.; Antonova, I.; Komonov, A.; Medvedev, M. Colloidal Solutions of Niobium Trisulfide and Niobium Triselenide. *J. Mater. Chem. C* **2014**, *2*, 5479-5486.

88. Chianelli, R.; Dines, M. Reaction of n-Butyllithium with Transition Metal Trichalcogenides. *Inorg. Chem.* **1975**, *14*, 2417-2421.

89. Lipatov, A.; Wilson, P.; Shekhirev, M.; Teeter, J.; Netusil, R.; Sinitskii, A. Few-Layered Titanium Trisulfide (TiS_3) Field-Effect Transistors. *Nanoscale* **2015**, *7*, 12291-12296.

90. Wang, J.; Zheng, H.; Xu, G.; Sun, L.; Hu, D.; Lu, Z.; Liu, L.; Zheng, J.; Tao, C.; Jiao, L. Controlled Synthesis of Two-Dimensional 1*T*-$TiSe_2$ with Charge Density Wave Transition by Chemical Vapor Transport. *J. Am. Chem. Soc.* **2016**, *138*, 16216-16219.

91. Mangelsen, S.; Bensch, W. $HfTe_2$: Enhancing Magnetoresistance Properties by Improvement of the Crystal Growth Method. *Inorg. Chem.* **2020**, *59*, 1117-1124.

92. Harrison, M.; Graebner, A.; McNeil, W.; McGregor, D. Carbon Coating of Fused Silica Ampoules. *J. Cryst. Growth* **2006**, *290*, 597-601.

93. Meerson, G.A. *Atomic Energy*, Springer, **1963**, 1230-1233.

94. Fjellvåg, H.; Furuseth, S.; Kjekshus, A.; Rakke, T. Low-Temperature Oxidative Degradation of Low-Dimensional Zirconium and Hafnium Tellurides. *Solid State Commun.* **1987**, *63*, 293-297.

95. Zhang, M.; Wang, X.; Rahman, A.; Zeng, Q.; Huang, D.; Dai, R.; Wang, Z.; Zhang, Z. Pressure-Induced Topological Phase Transitions and Structural Transition in 1T-$TiTe_2$ Single Crystal. *Appl. Phys. Lett.* **2018**, *112*, 041907.

96. Lv, Y.; Zhang, F.; Zhang, B.; Pang, B.; Yao, S.; Chen, Y.; Ye, L.; Zhou, J.; Zhang, S.; Chen, Y. Microstructure, Growth Mechanism and Anisotropic Resistivity of Quasi-One-Dimensional $ZrTe_5$ Crystal. *J. Cryst. Growth* **2017**, *457*, 250-254.

97. Zhang, Y.; Di, C.; Lv, Y.; Dong, S.; Zhou, J.; Yao, S.; Chen, Y.; Lu, M.; Chen, Y. One-Order Decrease of Thermal Conductivity in Nanostructured $ZrTe_5$ and $HfTe_5$ Crystals. *Crystal Growth & Design* **2019**, *20*, 680-687.

98. Li, J.; Peng, J.; Zhang, S.; Chen, G. Anisotropic Multichain Nature and Filamentary Superconductivity in the Charge Density Wave System $HfTe_3$. *Phys. Rev. B* **2017**, *96*, 174510.

99. Späh, R.; Elrod, U.; Lux-Steiner, M.; Bucher, E.; Wagner, S. *pn* Junctions in Tungsten Diselenide. *Appl. Phys. Lett.* **1983**, *43*, 79-81.

100. Ubaldini, A.; Jacimovic, J.; Ubrig, N.; Giannini, E. Chloride-Driven Chemical Vapor Transport Method for Crystal Growth of Transition Metal Dichalcogenides. *Cryst. Growth Des.* **2013**, *13*, 4453-4459.

101. Ubaldini, A.; Giannini, E. Improved Chemical Vapor Transport Growth of Transition Metal Dichalcogenides. *J. Cryst. Growth* **2014**, *401*, 878-882.

102. Sankar, R.; Narsinga Rao, G.; Muthuselvam, I.; Butler, C.; Kumar, N.; Senthil Murugan, G.; Shekhar, C.; Chang, T.; Wen, C.; Chen, C.; Lee, W.; Lin, M.; Jeng, H.; Felser, C.; Chou, F. Polymorphic Layered $MoTe_2$ from Semiconductor, Topological Insulator, to Weyl Semimetal. *Chem. Mater.* **2017**, *29*, 699-707.

103. Jiang, J.; Liu, Z.; Sun, Y.; Yang, H.; Rajamathi, C.; Qi, Y.; Yang, L.; Chen, C.; Peng, H.; Hwang, C.; Sun, S.; Mo, S.; Vobornik, I.; Fujii, J.; Parkin, S.; Felser, C.; Yan, B.; Chen, Y. Signature of Type-II Weyl Semimetal Phase in $MoTe_2$. *Nat. Commun.* **2017**, *8*, 13973.

104. Barry, J.; Hughes, H.; Klipstein, P.; Friend, R. Stoichiometry Effects in Angle-Resolved Photoemission and Transport Studies of $Ti_{1+x}S_2$. *J. Phys. C: Solid State Phys.* **1983**, *16,* 393-402.

105. Baglio, J.; Kamieniecki, E.; DeCola, N.; Struck, C.; Marzik, J.; Dwight, K.; Wold, A. Growth and Characterization of n-WS_2 and Niobium-Doped p-WS_2 Single Crystals. *J. Solid State Chem.* **1983**, *49*, 166-179.

106. Pisoni, A.; Jacimovic, J.; Barisic, O. S.; Walter, A.; Nafradi, B.; Bugnon, P.; Magrez, A.; Berger, H.; Revay, Z.; Forro, L. The Role of Transport Agents in MoS_2 Single Crystals. *J. Phys. Chem. C* **2015**, *119*, 3918-3922.

107. Su, J.; Liu, K.; Wang, F.; Jin, B.; Guo, Y.; Liu, G.; Li, H.; Zhai, T. van der Waals 2D Transition Metal Tellurides. *Adv. Mater. Interfaces* **2019**, *6*, 1900741.

108. Binnewies, M.; Schmidt, M.; Schmidt, P. Chemical Vapor Transport Reactions - Arguments for Choosing a Suitable Transport Agent. *Z. fur Anorg. Allg. Chem.* **2017**, *643*, 1295-1311.

109. Lévy, F.; Berger, H. Single Crystals of Transition Metal Trichalcogenides. *J. Cryst. Growth* **1983**, *61*, 61-68.

110. Stonemeyer, S.; Cain, J.; Oh, S.; Azizi, A.; Elasha, M.; Thiel, M.; Song, C.; Ercius, P.; Cohen, M.; Zettl, A. Stabilization of $NbTe_3$, VTe_3, and $TiTe_3$ via Nanotube Encapsulation. *J. Am. Chem. Soc.* 2021, *143*, 4563-4568.

111. Kabiraj, A.; Mahapatra, S. Machine-Intelligence-Driven High-Throughput Prediction of 2D Charge Density Wave Phases. *J. Phys. Chem. Lett.* **2020**, *11*, 6291-6298.

CHAPTER 2

INSIGHTS INTO THE CRYSTALLINE GROWTH OF HAFNIUM TRITELLURIDE

Matthew D. Seivert and Tina T. Salguero. To be submitted to *Crystal Growth & Design*.

Abstract

In this study, we report pathways leading to the synthesis and crystal growth of $HfTe_3$. Polycrystalline $HfTe_3$ was isolated via the solid state route at 550 °C, whereas single crystalline $HfTe_3$ was prepared via the chemical vapor transport (CVT) route at 530 °C. For polycrystalline $HfTe_3$, we determined that Hf metal source (Hf foil vs Hf powder) and cooling route (immediate water quenching, controlled slow-cooling, or natural cooling) had an impact on singular phase isolation. When Hf foil was used, polycrystalline $HfTe_3$ could be isolated regardless of cooling route implemented, versus Hf powder, in which we only isolated phase-pure $HfTe_3$ when employing immediate water quenching. For single crystalline $HfTe_3$, we found that ball milling under Ar atmosphere for 1 h led to optimized vs crystal growth versus 0.5 h treatment, or mortar/pestle grinding. We also determined that transport agents such as I_2, NH_4Cl, and $TeBr_4$ each led to distinctive crystal morphologies under CVT conditions. Finally, x-ray photoelectron spectroscopy (XPS) was implemented for single crystalline $HfTe_3$ in which we observed the Hf^{4+} valence state as a result of surface oxidation.

Introduction

Since interest in layered van der Waals materials was re-ignited by the remarkable isolation of graphene in 2004, researchers have gravitated toward low-dimensional metal chalcogenides. Such materials present promising alternatives for downscaled optical and electronic devices that can be complementary to state-of-the-art silicon-based technologies. Many investigators have focused on the transition metal dichalcogenides and, more recently, the trichalcogenides, due to their unique properties and amenability for nanostructuring.[1,2,3,4] These trichalcogenides with MX_3 compositions (where M is usually a group IV or V transition metal and X is S, Se, or Te) are comprised of MX_6 units exclusively in the trigonal prismatic geometry. These units are assembled into covalently bonded chains oriented along the *b* axis of the crystalline lattices; these chains may also be bound by weak van der Waals interactions across the *a*-*b* plane yielding "sheet-like" layers to a greater or lesser extent, depending on composition. The van der Waals gap between these layers makes them susceptible to mechanical or chemical exfoliation. Furthermore, MX_3 materials are quasi-one-dimensional in nature due to the confinement of electrons within the atomic chains, are characterized by strong anisotropic character, and in some cases, exhibit transitions into charge density wave (CDW) and superconductive states.[2] The quasi-one-dimensional nature of MX_3 materials is particularly defined by the weak van der Waals interactions in the *a*-*b* plane, versus true one-dimensional materials like Sb_2S_3, Bi_2S_3, V_2Se_9, and Nb_2Se_9.[5,6,7,8,9]

Here we focus on group IV tritelluride compositions because both $HfTe_3$ and $ZrTe_3$ show useful electronic properties.[10,11,12] Although bulk $TiTe_3$ has not been reported, a recent report by Zettl and coworkers described the growth of $TiTe_3$ chains within multiwalled carbon nanotubes.[2,13] Previous studies of $ZrTe_3$ have examined how to tune the conditions for superconductivity and CDWs through the application of pressure, the intercalation of transition metals, doping with

chalcogen counterparts, and alloying.[14,15,16,17,18,19] In recent work, we and others characterized the exceptionally high current density of single crystalline $ZrTe_3$, ~100 MA/cm^2, which surpasses values of 2-3 MA/cm^2 for elemental copper.[20,21]

In comparison to $ZrTe_3$, much less work has been done with $HfTe_3$ because it poses synthetic challenges that have limited its reproducible preparation. Early reports of $HfTe_3$ during the 1970s described powder samples prepared from the elements at 470-520 °C.[22] Since then, several studies have reported the chemical vapor transport (CVT) growth of $HfTe_3$ crystals under diverse conditions. Chen and coworkers claimed the synthesis of $HfTe_3$ single crystals with a gradient of 500–540 °C, I_2 transport agent, and polycrystalline $HfTe_3$ which was prepared by heating a pressed pellet of the elements at 500 °C followed by quenching.[10] However, Denholme and coworkers found that such rapid quenching favors $HfTe_2$, leading to samples mixed with unreacted Te. Their successful approach to polycrystalline $HfTe_3$ involved slow-cooling from 500–470 °C (rate of ~0.25 °C h^{-1}), followed by cooling to room temperature at a rate of 5 °C h^{-1}.[12] In related work, Zettl and coworkers examined the growth of few- and single-chains of $HfTe_3$ within carbon nanotubes at 520 °C using CVT conditions.[23] Additional studies have involved $Hf_xZr_{1-x}Te_3$ (x=0.01 or 0.05) and $ZrTe_{3-x}Se_x$ (x<0.04) crystals prepared by I_2-mediated CVT. [14,24]

In this contribution, we consider the solid state synthesis and CVT crystal growth of $HfTe_3$. For solid state syntheses, we determined that choice of Hf metal source, temperature, and cooling method were critical to single phase isolation. For single crystalline growth, we found that ball-milled polycrystalline $HfTe_3$ under Ar atmosphere was best for crystal growth. In addition, we found that choice in transport agent (I_2, NH_4Cl, or $TeBr_4$) could affect both crystal size and morphology. These experimental studies point to the most reproducible pathways toward polycrystalline and single crystalline samples of these materials. The results help resolve previous

contradictions regarding optimum reaction conditions. Furthermore, we implemented XPS analysis for single crystalline $HfTe_3$ showing the presence of the Hf^{4+} oxidation state in our samples confirming significant surface oxidation, a disadvantageous but important observation in our experimental results.

Experimental

Materials: Hf foil (0.25 mm thickness, annealed, 99.5% metals basis excluding Zr), Hf powder (~325 mesh, 99.6% metals basis excluding Zr), and $TeBr_4$ (99.9% metals basis) were purchased from Alfa Aesar. Te powder (~200 mesh, 99.8% trace metals basis) and NH_4Cl (≥ 99.5%) were purchased from Sigma Aldrich. I_2 (crystals, 99.9% purity) was obtained from J.T. Baker Company. HNO_3 (15.8 M, Certified ACS Plus) was obtained from Fisher Chemical.

Ampule Preparation: Two sizes of fused quartz glass ampules were used in this work. "Solid state ampules": body dimensions of 90 mm length, 19 mm inner diameter, 22 mm outer diameter, volume ~33 cm^3; neck dimensions of 170 mm length, 7 mm inner diameter, 9.6 mm outer diameter. "CVT ampules": body dimensions of 175 mm length, 10 mm inner diameter, 14 mm outer diameter, volume ~13 cm^3; neck dimensions of 170 mm length, 7 mm inner diameter, 9.6 mm outer diameter. Ampules were cleaned by immersing in 15.8 M HNO_3 overnight. Afterwards, they were rinsed 3-5 times with deionized water, and then positioned in a horizontal tube furnace or box furnace and heated at 6 °C min^{-1} to a final temperature of 900 °C for 12 h followed by natural cooling to room temperature.

To apply the carbon coating, the inside of an ampule was rinsed thoroughly with acetone. Then a National brand flame torch (propane and oxygen fuel source) was used to heat the outside of the ampules slowly from bottom to top at ~1400 °C under constant rotation using a glass

blowing lathe to assure homogeneous carbon deposition. Upon heating, a black layer immediately covers the inside of the ampule. After cooling to room temperature, the procedure was repeated to deposit an additional layer of carbon.

Solid State Synthesis of $HfTe_3$: 0.954 g (5.34 mmol) Hf foil was cut into mm-sized squares and positioned at the bottom of a carbon-coated solid state quartz ampule in addition to 2.046 g (16.0 mmol) Te powder while exposed to ambient atmosphere. The ampule was evacuated and backfilled with Ar three times using a Schlenk line manifold before being flame sealed under vacuum (~10^{-2} Torr). The evacuated ampule was then placed inside a preheated horizontal tube furnace at 550 °C for either (i) 48 h, followed by quenching by submerging the hot ampule in a salted ice water bath, or (ii) 10 d, followed by cooling to 520 °C at 0.25 °C h^{-1}, and then to 25 °C at 5 °C h^{-1}. The product was isolated as mm-sized, grey/black flakes (2.2852 g collected; 76.17 % isolated yield).

Crystal Growth of $HfTe_3$: Approximately 1 g (1.78 mmol) of pre-prepared $HfTe_3$ (solid state synthesis) was lightly ground into a fine powder using an agate mortar/pestle inside an Ar-filled glovebox. The resulting powder was ball milled under Ar atmosphere for 1 h (Fritsch Pulverisette 6 planetary ball mill using about thirty 10-mm Si_3N_4 balls in an 80 mL Si_3N_4 milling bowl at 300 rpm). Upon completion, the milling bowl was opened inside the glovebox to avoid combustion. I_2 (~125 mg), NH_4Cl (~ 55 mg), or $TeBr_4$ (~125 mg) were transferred to a carbon-coated solid state quartz glass ampule using a funnel, followed by the ground $HfTe_3$ (1.1105 g). The ampule was evacuated and backfilled with Ar three times using a Schlenk line manifold while submerged in an acetonitrile/dry ice bath before being flame sealed under vacuum (~10^{-2} Torr). The evacuated ampule was positioned inside a preheated horizontal tube furnace at 530 °C (no gradient) for 14 d

followed by natural cooling to room temperature. $HfTe_3$ crystals were observed as silver plates mixed with microcrystalline $HfTe_3$.

Characterization: Powder X-ray diffraction (PXRD) data were collected on a Bruker D8 Advance instrument utilizing a Co−Kα X-ray source (λ = 1.78890 Å) operated at 35 kV and 40 mA. Data was collected from 5 to 80° 2θ with a scan rate of 0.1 s/step. Samples were prepared as powder mounts.

Scanning electron microscopy (SEM) analysis was performed with an FEI Teneo FE-SEM at 10 keV with a spot size of 13. Energy dispersive x-ray spectroscopy (EDS) was performed using an Aztec Oxford Instruments X-MAX^N detector operated at 10 keV with a spot size of 13. Samples were mounted onto a stub with carbon tape and exfoliated using scotch tape.

XPS analysis was accomplished using a Thermo Scientific K-Alpha X-ray Photoelectron Spectrometer System operated with a monochromatic beam of Al Kα x-rays (1486 eV) with a 50 μm spot size. Instrument calibration was completed with Au (4*f*), Ag (3*d*), and Cu (2*p*) standards. The adventitious C 1*s* peak at ~284.9 eV was used for binding energy reference. Samples were mounted on carbon tape and exfoliated using scotch tape. Peak fitting (Gaussian type) and data analysis were completed using Thermo Scientific Avantage Software.

Results and Discussion

General Synthetic Considerations: The high affinity of hafnium for oxygen (unavoidably present in fused quartz and as oxide impurities) prompted us to use carbon-coated ampules for all syntheses; indeed, we observed heavily oxidized products during early attempts using non-coated ampules.[12,25,26,27,28] In addition, the use of air-free conditions for all reactions is absolutely necessary. We have also found that competition between neighboring phases is significantly more

problematic for $HfTe_3$ than its isostructural counterpart $ZrTe_3$. However, the choice of appropriate synthetic conditions can help minimize or even avoid the formation of competing phases during MTe_3 preparation.

Solid State Synthesis of $HfTe_3$: Advantageously, we have established that polycrystalline $HfTe_3$ can be prepared readily by solid state synthesis from the elements, with reaction temperature being the most crucial factor for success but with temperature gradient and starting materials also playing roles. Prior literature indicates that $HfTe_3$ forms at 500 °C, but our experiments show that an elevated reaction temperature of 550 °C is ideal; according to powder x-ray diffraction (PXRD), the major product at 550 °C is reliably phase-pure $HfTe_3$. In fact, 500 °C favors the formation of $HfTe_5$, and temperatures >550 °C lead to $HfTe_2$ (Figure S2.3).[10,12,28,29,30] Prior reports also describe the use of various cooling protocols. Following Chen and coworkers, we quenched our solid-state product after reaction at 550 °C for 48 h.[10] Quenching at this temperature reliably resulted in $HfTe_3$ as shown in Figure 2.1 which is evidenced by characteristic peaks such as those at ~10°, ~30-40°, and ~45° 2θ . In contrast, Denholme and coworkers did not find quenching to be effective and instead used slow cooling to isolate $HfTe_3$.[12] Based on their cooling recipe of 500 to 470 °C at 0.25 °C h^{-1}, followed by 470 to 25 °C at 5 °C h^{-1}, we applied a recipe of 550 to 520 °C at 0.25 °C h^{-1}, followed by 520 to 25 °C at 5 °C h^{-1}. This reaction yielded dark gray $HfTe_3$ polycrystalline product (Figure 2.1) and a significant quantity of silver wires, which we determined were crystallized elemental Te by PXRD and SEM/EDS (Figure S2.4). We also evaluated the efficacy of natural cooling, i.e., ending heating after 48 h and allowing the furnace to cool to room temperature before removing the ampule. As shown in Figure 2.1, we isolated phase-pure $HfTe_3$ after natural cooling from 48 h at 550 °C. Unexpectedly, we found that the form of the Hf precursor (foil vs. powder) could impact the products. Whereas Hf foil consistently led to $HfTe_3$ regardless of cooling

protocol, the use of Hf powder yielded $HfTe_3$ only in combination with quenching; as shown in Figure 2.1, natural cooling led to $HfTe_2$, which can be distinguished by the presence of a peak at ~16° 2θ, in addition to the absence of peaks present in $HfTe_3$. We hypothesize that the choice in Hf precursor was important due to the considerable difference in surface area between Hf foil and Hf powder. Hf foil has significantly less surface area, which we believe contributed to lower reactivity and ultimately "stabilization" of the $HfTe_3$ phase upon reaction with Te. Comparatively, the larger surface area from Hf powder likely contributed to increased reactivity, resulting in neighboring Hf–Te phase isolation in the absence of immediate quenching. In addition, we note that Hf is able to passivate by forming an "impermeable" surface oxide layer, which was likely an important factor when trying to isolate phase-pure $HfTe_3$.

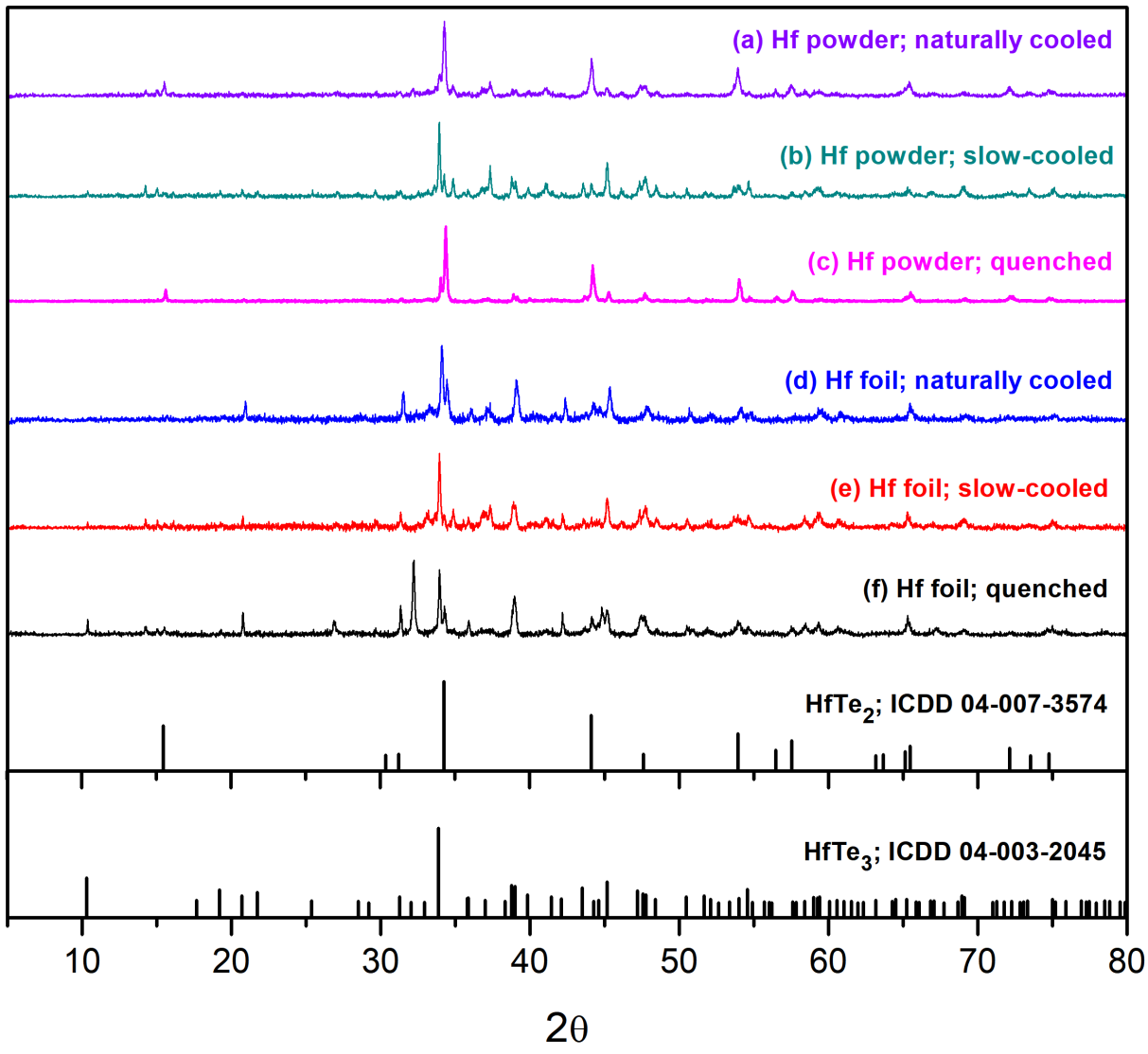

Figure 2.1 PXRD patterns of products from $HfTe_3$ solid state synthesis attempts at 550 °C, using either Hf foil or powder, followed by varying cooling protocols.

Surprisingly, we observed $HfTe_3$ wires in the quenched product when using Hf powder (Figure 2.2b). The mm-sized wires present in the sample were confirmed to be $HfTe_3$ based on the experimental atomic percentages collected via EDS (Hf: 27.2%, Te: 72.8%). Upon further analysis with SEM, we determined that $HfTe_3$ also sometimes adopts an elongated platelet morphology not

previously reported (Figure 2.2a). EDS confirmed the composition of as synthesized elongated platelets and found elemental analysis to be within the average atomic percentages (Hf: 25.5 %, Te: 74.5%) expected for $HfTe_3$.

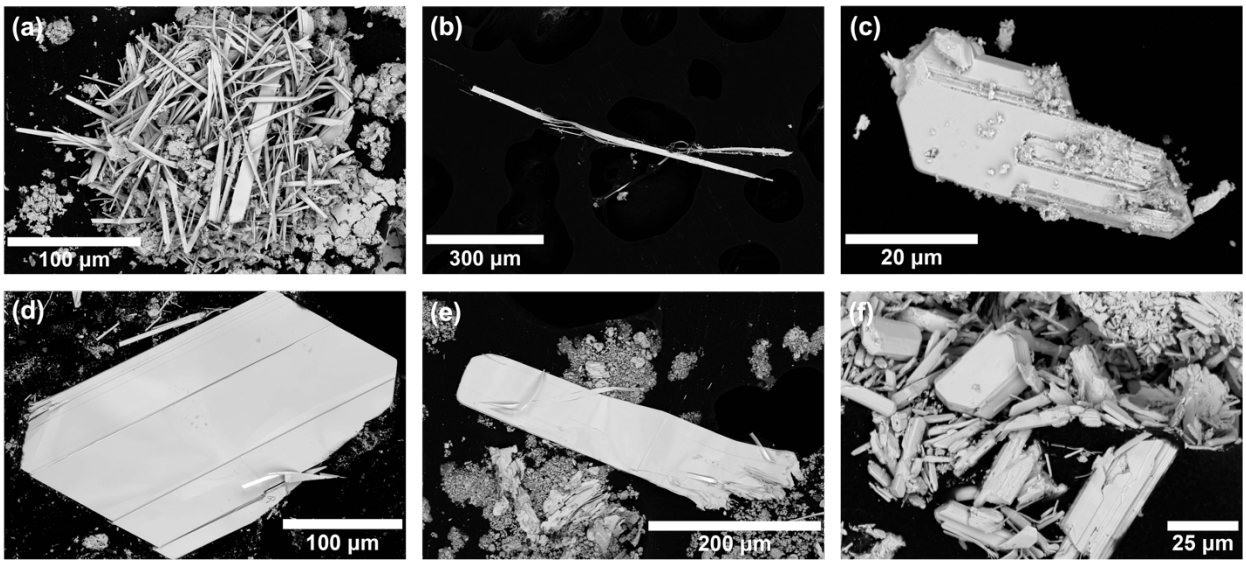

Figure 2.2 SEM imaging of representative $HfTe_3$ crystals: (a) elongated platelet morphology of $HfTe_3$ synthesized via solid state route using Hf foil at 550 °C for 48 h followed by quenching (b) single crystalline $HfTe_3$ synthesized via solid state route using Hf powder at 550 °C for 48 h followed by quenching. Single crystalline hexagonal plate-like morphologies synthesized via CVT approach at 530 °C using polycrystalline precursor ball milled at 300 rpm for (c) 0.5 h and (d) 1 h under air-free conditions. Single crystalline ribbon-like and plate-like $HfTe_3$ synthesized via CVT approach at 530 °C using polycrystalline precursor ball milled at 300 rpm for 1 h substituting I_2 transport agent for (e) NH_4Cl and (f) $TeBr_4$.

CVT growth of $HfTe_3$ crystals: Consistent with the findings of Chen and coworkers,[10] we conclude that the CVT growth of $HfTe_3$ single crystals is reproducible when starting with polycrystalline $HfTe_3$ prepared by solid state synthesis and I_2 as the transport agent. CVT experiments starting from the elements yielded exclusively cm-sized $HfTe_5$ crystals (Figure S2.5) instead of the desired product. Optimization of reaction temperature is also essential, and we examined conditions of 520–580 °C with gradients in the range of 0–40°, selected based on prior reports.[10,23] These experiments indicate that the best conditions for the CVT growth of $HfTe_3$ occur at 530 °C without a gradient. Lower or higher temperatures of 520 °C or 540–580 °C led to increased $HfTe_2$ and/or $HfTe_5$ formation (Figure S2.7). Thus, the optimized conditions represent a compromise that maximizes $HfTe_3$ formation while minimizing $HfTe_2$ and $HfTe_5$. Most CVT processes take advantage of temperature gradients to enhance the transport and circulation of solid-gaseous-solid species within the sealed ampule, therefore the lack of gradient here is unusual.[31]

We also evaluated the impact of mortar/pestle grinding or planetary ball milling of the polycrystalline $HfTe_3$ precursor prior to CVT, which can increase reactivity by decreasing grain sizes and introducing defects. Both techniques were conducted completely under Ar atmosphere. Hand-ground precursor led solely to $HfTe_5$ formation. Ball milled precursor (300 rpm for 0.5 h or 1 h) led to $HfTe_3$ crystals (40–50 μm after 0.5 h and 300–500 μm after 1 h), and decreased $HfTe_2$ and $HfTe_5$ content, especially with the 1 h milled material as seen in Figure 2.2c and 2.2d.

We evaluated several alternative transport agents, including NH_4Cl and $TeBr_4$. The change to NH_4Cl led to anisotropic $HfTe_3$ growth, yielding crystals up to 200–400 μm long (Figure 2.2e). In contrast, transport with $TeBr_4$ led to 25-50 μm, blocky $HfTe_3$ crystals (Figure 2.2f) along with significant $HfTe_2$ and $HfTe_5$ formation. PXRD patterns are provided in Figure S2.8.

Despite the fact that CVT in the Hf–Te system tends to yield mixed phase products composed of $HfTe_3$, $HfTe_5$, and $HfTe_2$, optimization of reaction conditions makes it possible to favor $HfTe_3$ formation, and the distinct visual appearance of each phase makes it possible to identify the phase of single crystals with good accuracy. $HfTe_3$ crystals are silver, typically platelike with distorted hexagonal morphology, and have a distinctive surface texture—as seen in Figure 2.2d, these crystals exhibit parallel cleavage planes that we have not seen in other systems. $HfTe_2$ crystals are gold in color and present a smooth, hexagonal, platelet morphology (Figure S2.1a). $HfTe_5$ crystals are silver in color and can present varied morphologies, including anisotropic forms (Figure S2.1b). These observations were corroborated with SEM/EDS analysis: average atomic percentages for $HfTe_2$ (Hf: 35.7 %, Te: 64.3 %) and $HfTe_5$ (Hf: 17.1 %, Te: 82.9 %) confirmed the compositions of these phases.

XPS Analysis of $HfTe_3$: XPS of $HfTe_3$ single crystals provided information about its valence states and local bonding environments. A comprehensive list of experimental binding energies and additional information is provided in Table S2.1.

A doublet of Hf 4*f* peaks are present as illustrated in Figure 2.3a. A previous report found Hf 4*f* peaks for single crystalline $HfTe_3$ at 17.7 eV ($4f_{7/2}$), 19.5 eV ($4f_{5/2}$), 15.7 eV ($4f_{7/2}$), and 17.4 eV ($4f_{5/2}$), interpreted as the presence of mixed valence Hf^{4+} and Hf^{2+}.[10] These authors also compared their data to XPS binding energies of HfO_2 (18.3 eV and 20.0 eV), noting a small shift in the lower binding energy due to the presence of mixed valence Hf^{4+} and Hf^{2+}. Based on our results, we hypothesize the presence of the Hf^{4+} valence state in our single crystalline $HfTe_3$ sample. We believe the Hf^{4+} valence state was due to surface oxidation because of an O 1*s* peak that we assigned to HfO_2 which has been reported to have a O 1*s* peak at 531.4 eV (Figure S2.10a).[32] Furthermore, we found in related studies that oxidation of transition metal chalcogenide

materials (e.g. $MoTe_2$, $TiTe_2$, ZrS_2, HfS_2, etc.) causes an upward shift in binding energy due to the introduction of M—O (M = metal) bonding.[33,34,35] Work by Pumera and coworkers specifically cited Zr^{4+} and Hf^{4+} in pristine ZrS_2 and HfS_2 and the subsequent shift in higher binding energy due to oxide environments while under identical oxidation states.[34]

For the analysis of Te 3*d*, three doublets were present as illustrated in Figure 2.3b. Comparable data was also reported by Chen and coworkers in their report for $HfTe_3$: 572.7 eV ($3d_{5/2}$), 583.1 eV ($3d_{3/2}$), 576.9 eV ($3d_{5/2}$), and 587.3 eV ($3d_{3/2}$). We found a third doublet at 574.50 ($3d_{5/2}$) and 585.29 eV ($3d_{3/2}$) that we hypothesize was a result of Te—O bonding in our samples. The shift to higher binding energies because of oxidation is not limited to M—O bonding, with findings of the same behavior occurring in Te—O bonding also in previous reports.[33,35] Although this sample was surface exfoliated with tape prior to analysis, the persistent presence of M—O and Te—O bonding is consistent with the susceptibility of $HfTe_3$ to oxidation.

We also found the experimental spin-orbit splitting separations for Hf 4*f* (1.68 eV) and Te 3*d* (10.41 eV, 10.44 eV, and 10.79 eV) comparable to expected values (1.71 eV for Hf 4*f* and 10.39 eV for Te 3*d*).[36]

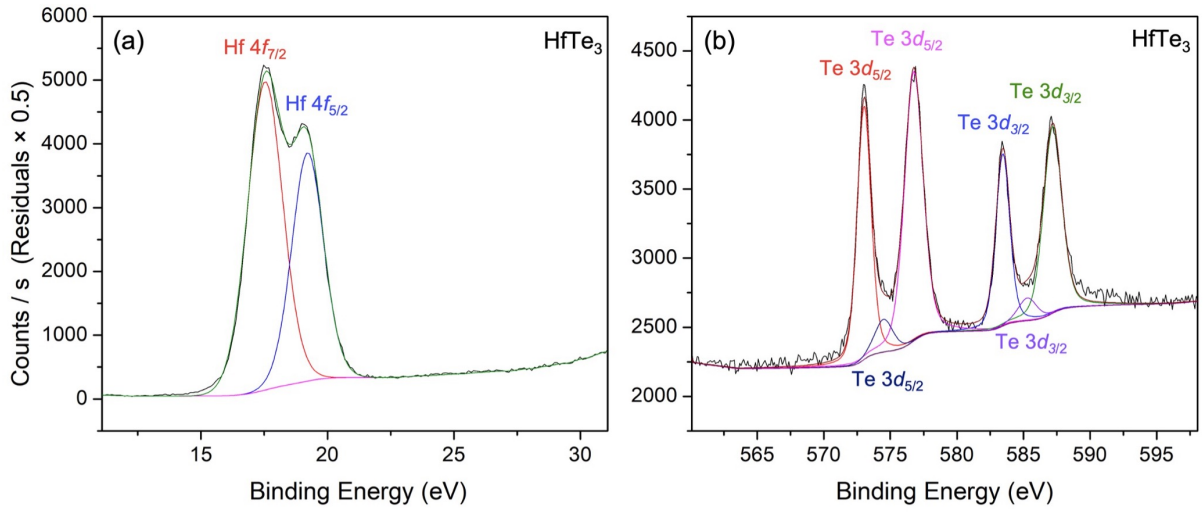

Figure 2.3 XPS spectra of (a) Hf 4*f* and (b) Te 3*d* collected from $HfTe_3$ crystals.

Conclusions

In this contribution, we have described successful approaches in isolating both polycrystalline and single crystalline $HfTe_3$. Indeed, $HfTe_3$ is significantly less thermodynamically stable than its isostructural counterpart $ZrTe_3$, or its neighboring Hf–Te phases ($HfTe_2$ and $HfTe_5$). Our work indicates the careful parameters needed to successfully isolate either polycrystalline or single crystalline $HfTe_3$, and the necessity of tuning the reaction temperature to bypass the $HfTe_5$ phase but not produce $HfTe_2$ at higher temperatures. Furthermore, we determined that starting materials, gradient, and transport agent could affect the presence of neighboring phases, crystal size, and morphology. XPS analysis confirmed the prone nature of $HfTe_3$ to surface oxidation. Overall, our findings expand synthetic pathways and considerations into isolating $HfTe_3$, which we believe will help workers in the field reproducibly isolate this material, and ultimately expand current research into this material for future applications.

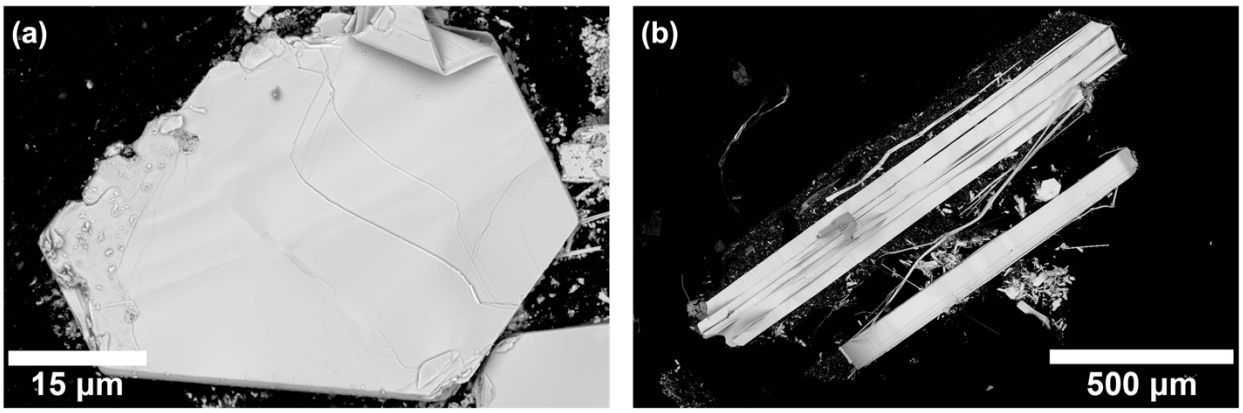

Figure S2.1 Representative SEM imaging of single crystalline (a) $HfTe_2$ and (b) $HfTe_5$.

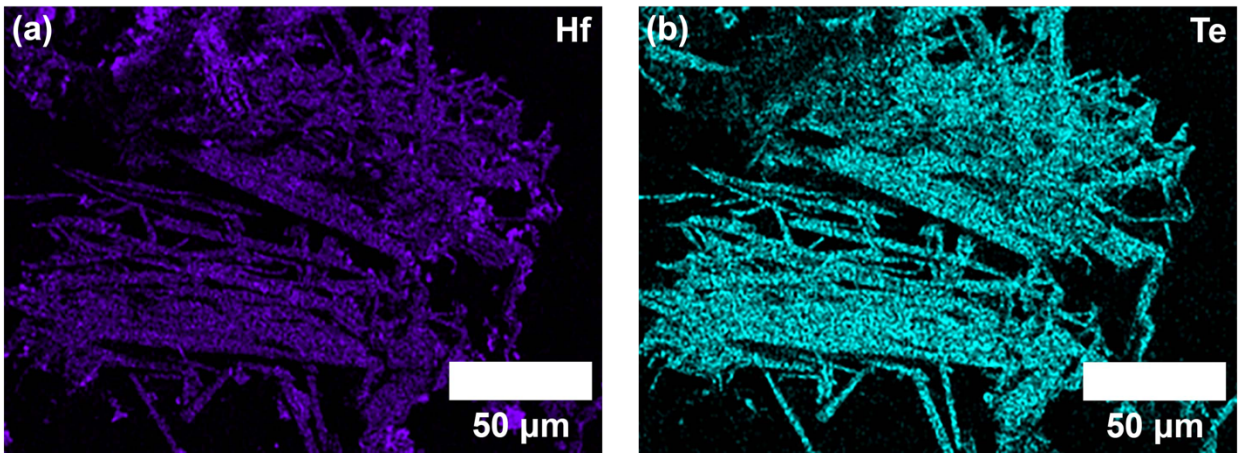

Figure S2.2 Elemental mapping of $HfTe_3$ illustrating elemental distribution of (a) Hf and (b) Te.

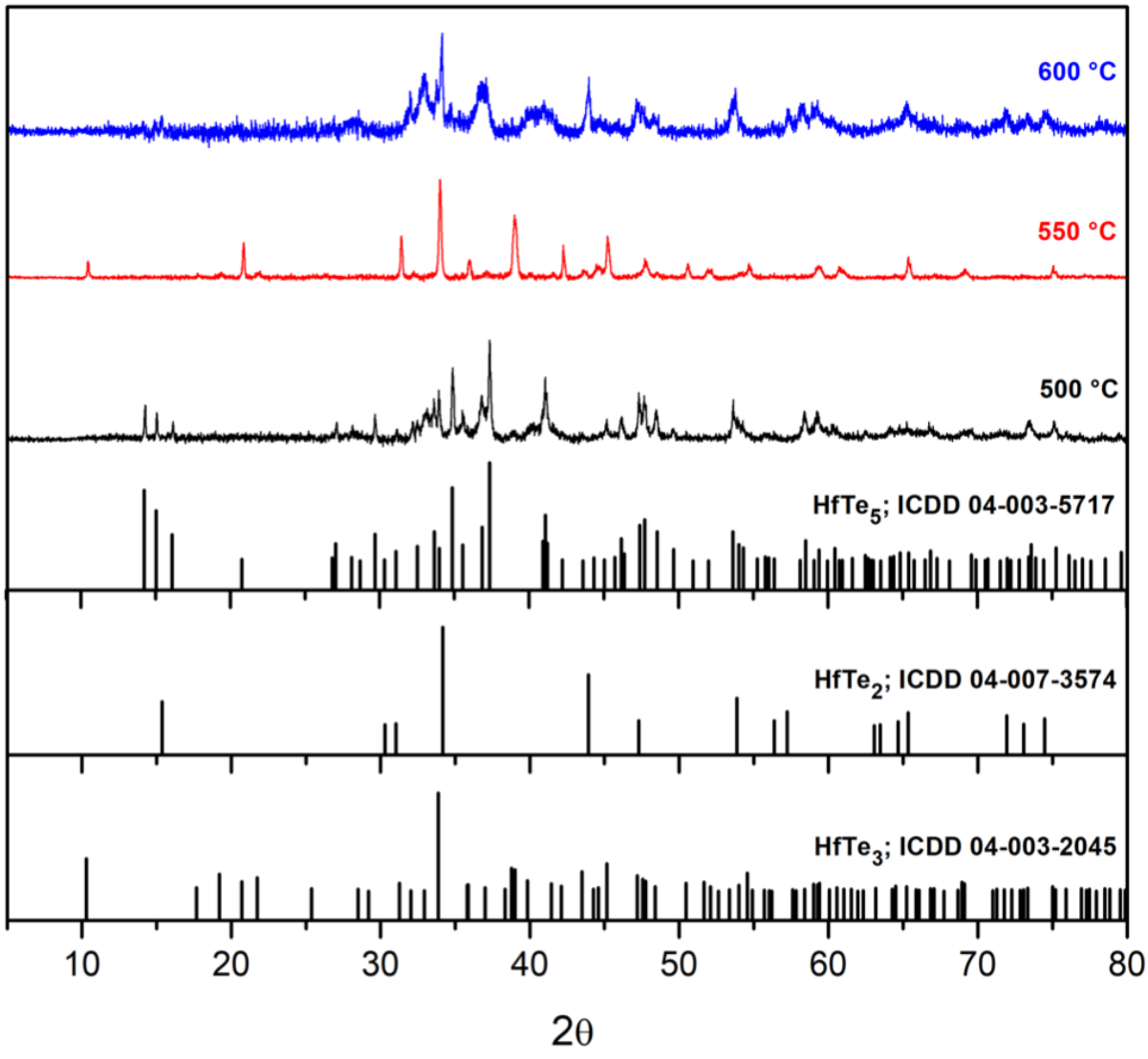

Figure S2.3 Representative PXRD patterns from solid-state reactions of Hf and Te attempted at 500, 550, and 600 °C.

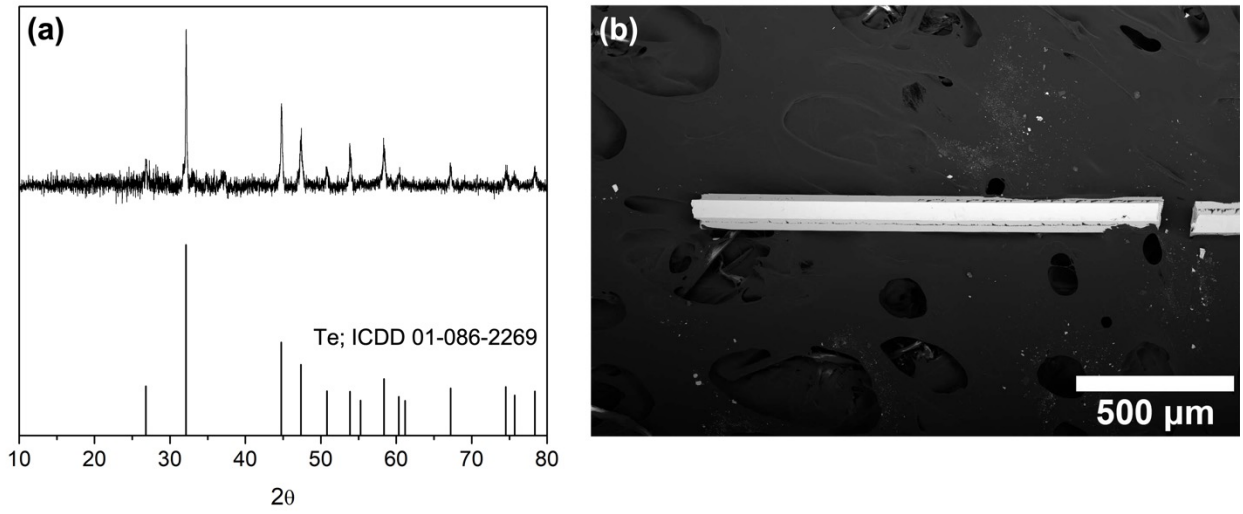

Figure S2.4 (a) PXRD and (b) SEM of silver, wirelike crystals from $HfTe_3$ solid state reaction (with slow-cooling) confirming the formation of crystalline Te.

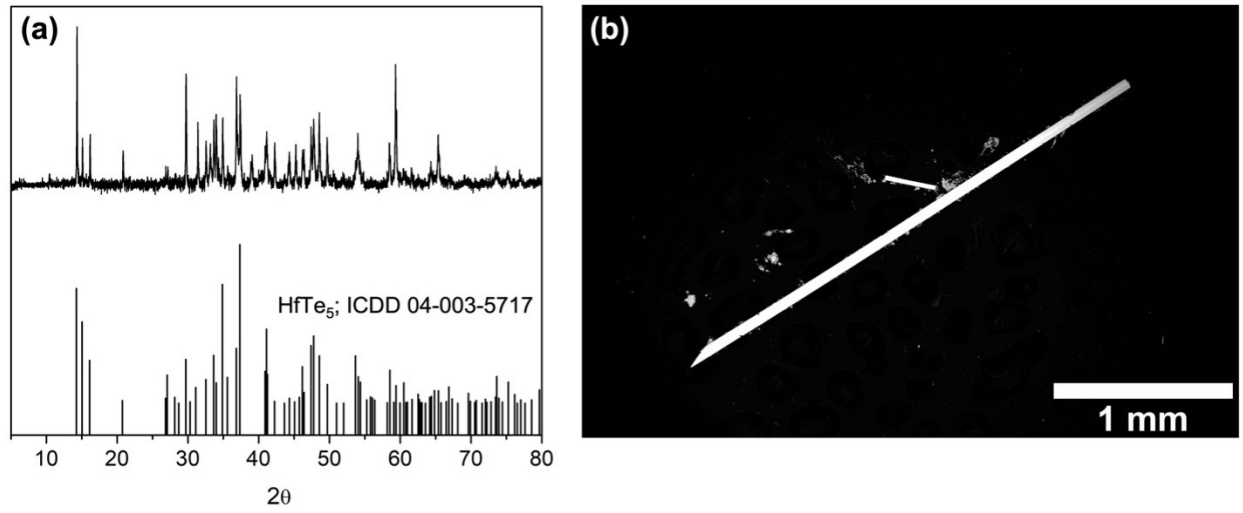

Figure S2.5 (a) PXRD and (b) SEM of silver, wirelike crystals from $HfTe_3$ CVT reaction (using the elements) confirming the formation of $HfTe_5$.

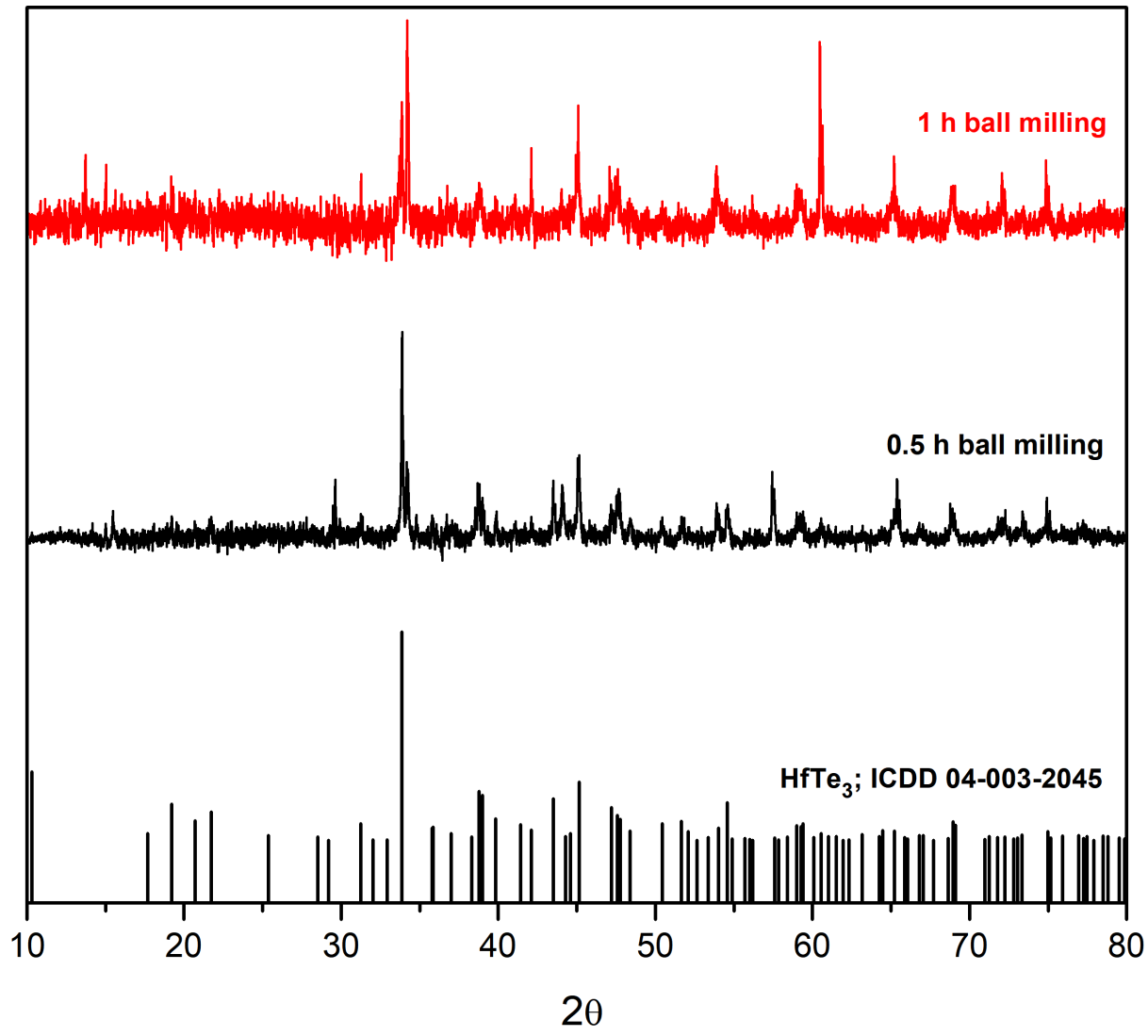

Figure S2.6 PXRD patterns of $HfTe_3$ prepared following CVT conditions after 0.5 h or 1 h ball milling.

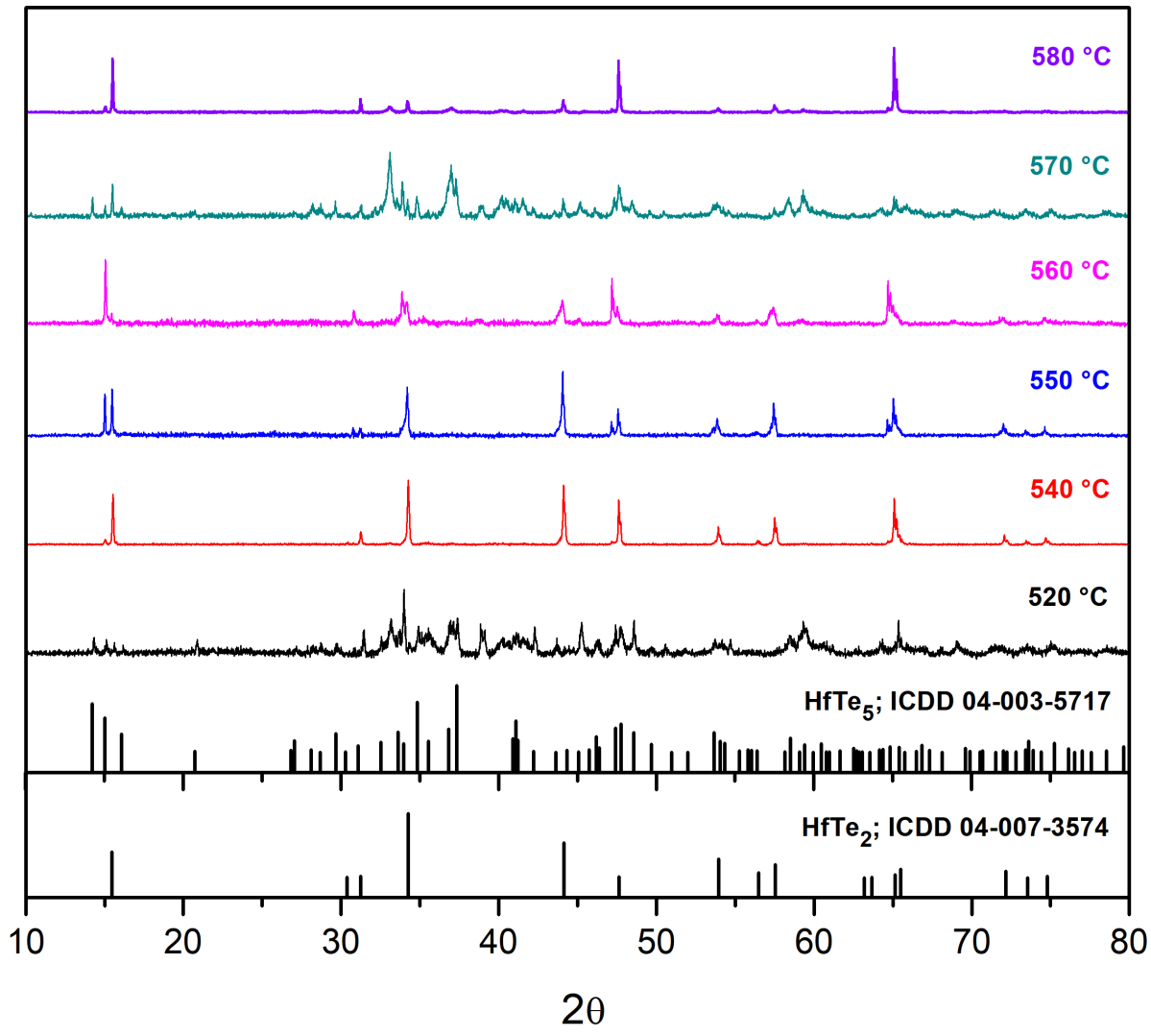

Figure S2.7 PXRD patterns of products from $HfTe_3$ CVT reactions at temperatures ranging from 520 to 580 °C.

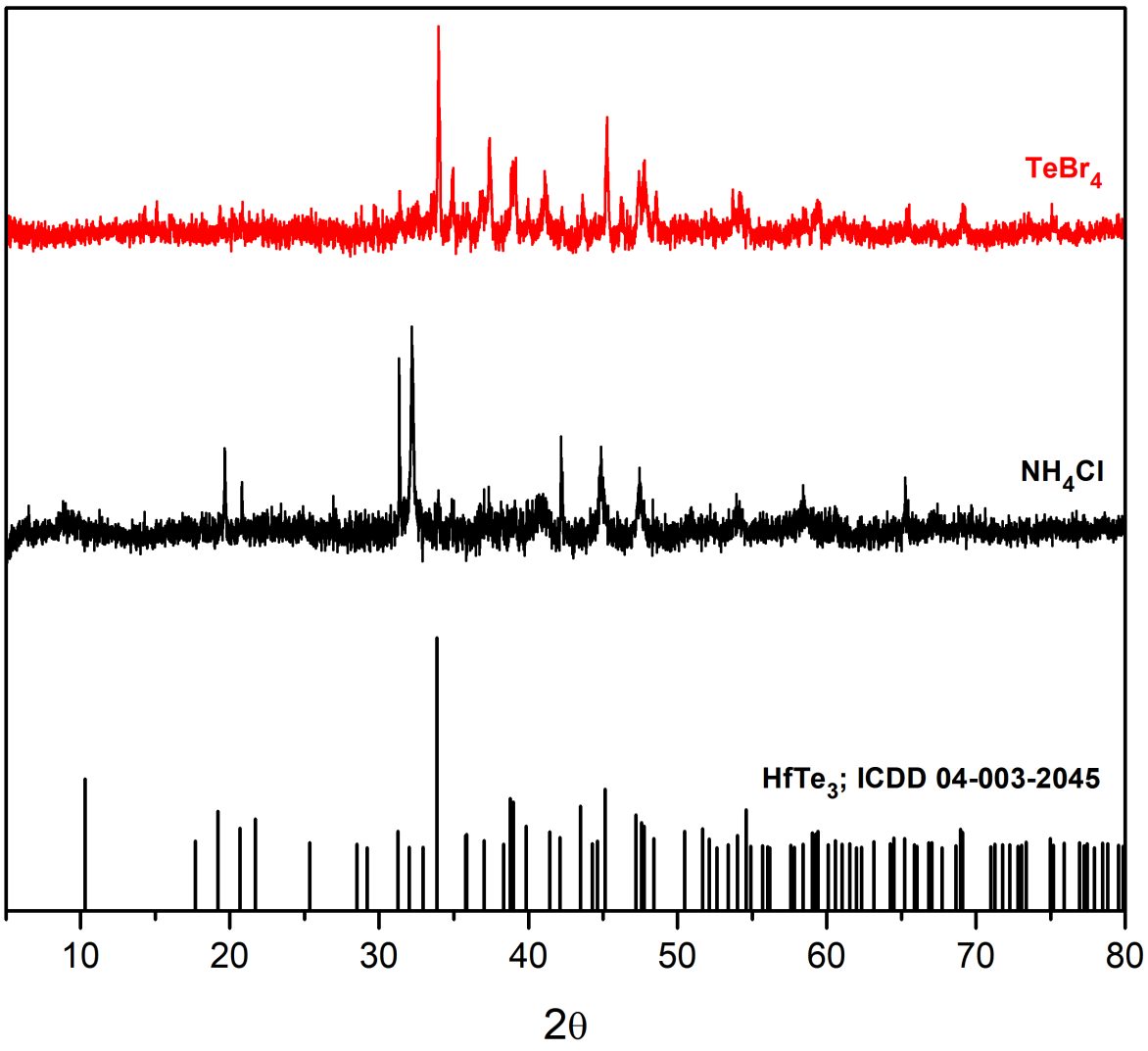

Figure S2.8 PXRD patterns of $HfTe_3$ CVT reactions using NH_4Cl and $TeBr_4$ as transport agents.

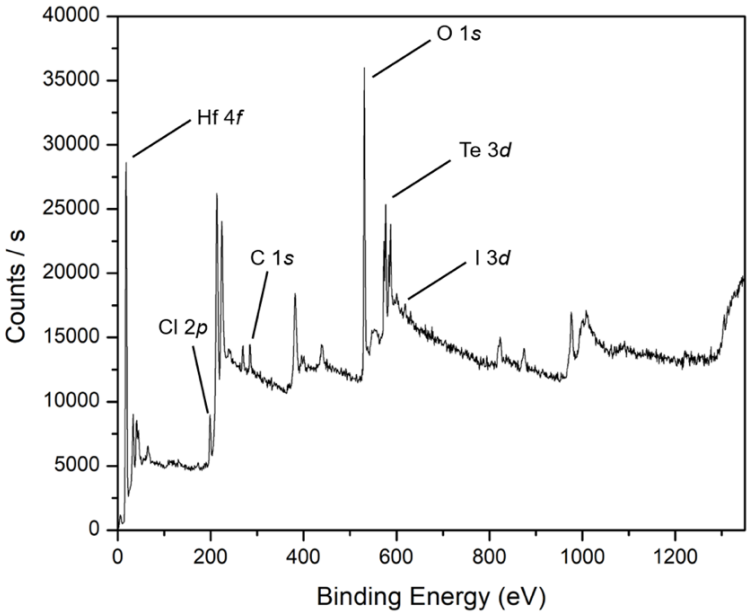

Figure S2.9 XPS survey collected from $HfTe_3$ crystals.

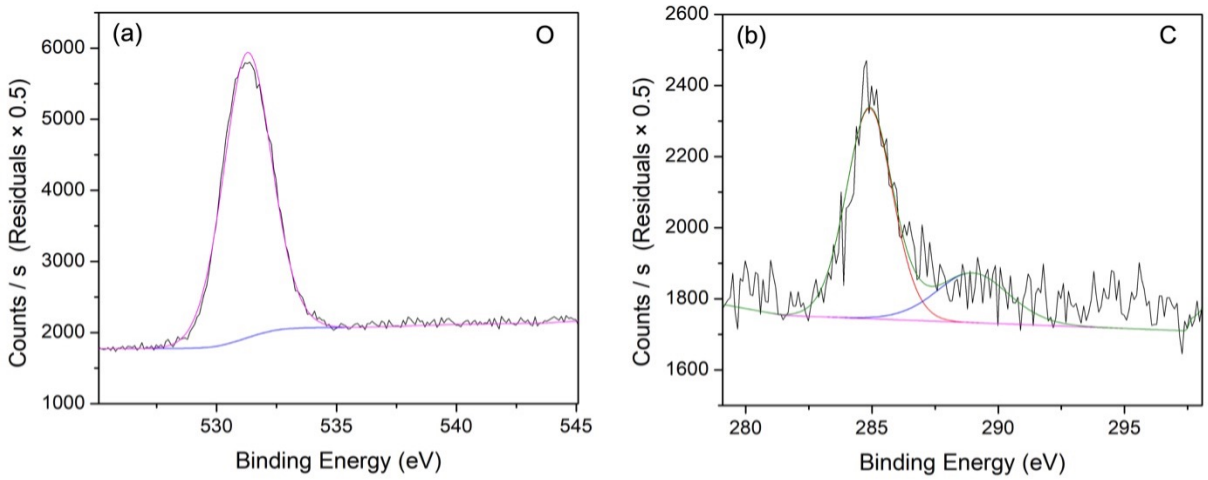

Figure S2.10 XPS spectra of (a) O 1*s* and (b) C 1*s* collected from $HfTe_3$ crystals.

Table S2.1 XPS peak assignments, binding energies, FWHM values, and atomic percentages collected from $HfTe_3$ crystals.

Experimental Result	Assignments	Binding Energies (eV)	FWHM (eV)	Atomic %
$HfTe_3$	Hf: $4f_{7/2}$, $4f_{5/2}$	17.53, 19.21	1.65, 1.48	14.37, 9.59
	Te: $3d_{5/2}$, $3d_{3/2}$	573.03, 583.44	1.24, 1.24	2.08, 2.06
	Te: $3d_{5/2}$, $3d_{3/2}$	576.75, 587.19	1.64, 1.64	2.93, 2.95
	Te: $3d_{5/2}$, $3d_{3/2}$	574.50, 585.29	1.64, 1.64	0.36, 0.36
	O: 1*s*	531.29	2.36	65.30

References

1. Dai, J.; Li, M.; Zeng, X. Group IVB Transition Metal Trichalcogenides: A New Class of 2D Layered Materials Beyond Graphene. *WIREs Comput. Mol. Sci.* **2016**, *6*, 211-222.

2. Island, J.; Molina-Mendoza, A.; Barawi, M.; Biele, R.; Flores, E.; Clamagirand, J.; Ares, J.; Sánchez, C.; van der Zant, H.; D'Agosta, R.; Ferrer, I.; Castellanos-Gomez, A. Electronics and Optoelectronics of Quasi-1D Layered Transition Metal Trichalcogenides. *2D Mater.* **2017**, *4*, 022003.

3. Chhowalla, M.; Shin, H.; Eda, G.; Li, L.; Loh, K.; Zhang, H. The Chemistry of Two-Dimensional Layered Transition Metal Dichalcogenide Nanosheets. *Nat. Chem.* **2013**, *5*, 263-275.

4. Manzeli, S.; Ovchinnikov, D.; Pasquier, D.; Yazyev, O.; Kis, A. 2D Transition Metal Dichalcogenides. *Nat. Rev. Mater.* **2017**, *2*, 17033.

5. Balandin, A.A.; Kargar, F.; Salguero, T.T.; Lake, R.K. One Dimensional van der Waals Quantum Materials. *Mater. Today* **2022**, *55*, 74-91.

6. Yang, W.; Yang, J.; Zhao, K.; Gao, Q.; Liu, L.; Zhou, Z.; Hou, S.; Wang, X.; Shen, G.; Pang, X.; Xu, Q.; Wei, Z. Low-Noise Dual-Band Polarimetric Image Sensor Based on 1D Bi_2S_3 Nanowire. *Adv. Sci.* **2021**, *8*, 2100075.

7. Zhou, Y.; Wang, L.; Chen, S.; Qin, S.; Liu, X.; Chen, J.; Xue, D.; Luo, M.; Cao, Y.; Cheng, Y.; Sargent, E.; Tang, J. Thin-film Sb_2Se_3 Photovoltaics with Oriented One-Dimensional Ribbons and Benign Grain Boundaries. *Nat. Photonics* **2015**, *9*, 409-415.

8. Oh, S.; Chae, S.; Kim, B.; Choi, K.; Jang, W.; Jang, J.; Hussain, Y.; Lee, D.; Kim, Y.; Yu, H.; Choi, J. Synthesis of a One-Dimensional Atomic Crystal of Vanadium Selenide (V_2Se_9). *RSC Adv.* **2018**, *8*, 33980-33984.

9. Oh, S.; Chae, S.; Kim, B.; Siddiqa, A.; Choi, K.; Jang, W.; Lee, K.; Kim, H.; Lee, D.; Kim, Y.; Yu, H.; Choi, J. Inorganic Molecular Chain Nb_2Se_9: Synthesis of Bulk Crystal and One-Atom-Thick Level Exfoliation. *Phys. Status Solidi Rapid Res. Lett.* **2018**, *12*, 1800451.

10. Li, J.; Peng, J.; Zhang, S.; Chen, G. Anisotropic Multichain Nature and Filamentary Superconductivity in the Charge Density Wave System $HfTe_3$. *Phys. Rev. B* **2017**, *96*, 174510.

11. Starowicz, P.; Battaglia, C.; Clerc, F.; Despont, L.; Prodan, A.; van Midden, H.; Szerer, U.; Szytuła, A.; Garnier, M.; Aebi, P. Electronic Structure of $ZrTe_3$. *J. Alloys Compd.* **2007**, *442*, 268-271.

12. Denholme, S.; Yukawa, A.; Tsumura, K.; Nagao, M.; Tamura, R.; Watauchi, S.; Tanaka, I.; Takayanagi, H.; Miyakawa, N. Coexistence of Superconductivity and Charge-Density Wave in the Quasi-One-Dimensional Material $HfTe_3$. *Sci. Rep.* **2017**, *7*, 45217.

13. Stonemeyer, S.; Cain, J.; Oh, S.; Azizi, A.; Elasha, M.; Thiel, M.; Song, C.; Ercius, P.; Cohen, M.; Zettl, A. Stabilization of $NbTe_3$, VTe_3, and $TiTe_3$ via Nanotube Encapsulation. *J. Am. Chem. Soc.* **2021**, *143*, 4563-4568.

14. Zhu, X.; Ning, W.; Li, L.; Ling, L.; Zhang, R.; Zhang, J.; Wang, K.; Liu, Y.; Pi, L.; Ma, Y.; Du, H.; Tian, M.; Sun, Y.; Petrovic, C.; Zhang, Y. Superconductivity and Charge Density Wave in $ZrTe_{3-x}Se_x$. *Sci. Rep.* **2016**, *6*, 26974.

15. Lei, H.; Zhu, X.; Petrovic, C. Raising T_c in Charge Density Wave Superconductor $ZrTe_3$ by Ni Intercalation. *Europhys. Lett.* **2011**, *95*, 17011.

16. Zhu, X.; Lei, H.; Petrovic, C. Coexistence of Bulk Superconductivity and Charge Density Wave in Cu_xZrTe_3. *Phys. Rev. Lett.* **2011**, *106,* 246404.

17. Tsuchiya, S.; Matsubayashi, K.; Yamaya, K.; Takayanagi, S.; Tanda, S.; Uwatoko, Y. Effects of Pressure and Magnetic Field on Superconductivity in $ZrTe_3$: Local Pair-Induced Superconductivity. *New J. Phys.* **2017**, *19*, 063004.

18. Yomo, R.; Yamaya, K.; Abliz, M.; Hedo, M.; Uwatoko, Y. Pressure Effect on Competition Between Charge Density Wave and Superconductivity in $ZrTe_3$: Appearance of Pressure-Induced Reentrant Superconductivity. *Phys. Rev. B* **2005**, *71*, 132508.

19. Liu, Y.; Hu, Z.; Tong, X.; Leshchev, D.; Zhu, X.; Lei, H.; Stavitski, E.; Attenkofer, K.; Petrovic, C. Thermal Transport and Mixed Valence in $ZrTe_3$ Doped with Hf and Se. *Appl. Phys. Lett.* **2022**, *120*, 022601.

20. Geremew, A.; Bloodgood, M.; Aytan, E.; Woo, B.; Corber, S.; Liu, G.; Bozhilov, K.; Salguero, T.; Rumyantsev, S.; Rao, M.; Balandin, A.A. Current Carrying Capacity of Quasi-1D $ZrTe_3$ van der Waals Nanoribbons. *IEEE Electron Device Lett.* **2018**, *39*, 735-738.

21. Geremew, A.; Rumyantsev, S.; Bloodgood, M.; Salguero, T.; Balandin, A. Unique Features of the Generation–Recombination Noise in Quasi-One-Dimensional van der Waals Nanoribbons. *Nanoscale* **2018**, *10*, 19749-19756.

22. Brattås, L.; Kjekshus, A. On the Properties of Compounds with the $ZrSe_3$ Type Structure. *Acta Chem. Scand.* **1972**, *26*, 3441-3449.

23. Meyer, S.; Pham, T.; Oh, S.; Ercius, P.; Kisielowski, C.; Cohen, M.; Zettl, A. Metal-Insulator Transition in Quasi-One-Dimensional $HfTe_3$ in the Few-Chain Limit. *Phys. Rev. B* **2019**, *100*, 041403.

24. Liu, Y.; Hu, Z.; Tong, X.; Leshchev, D.; Zhu, X.; Lei, H.; Stavitski, E.; Attenkofer, K.; Petrovic, C. Thermal Transport and Mixed Valence in $ZrTe_3$ Doped with Hf and Se. *Appl. Phys. Lett.* **2022**, *120*, 022601.

25. Fjellvåg, H.; Furuseth, S.; Kjekshus, A.; Rakke, T. Low-Temperature Oxidative Degradation of Low-Dimensional Zirconium and Hafnium Tellurides. *Solid State Comm.* **1987**, *63*, 293-297.

26. Yamanaka, S.; Takatsuka, N.; Katsura, M.; Miyake, M. Study of the Zr-Te-O Ternary System. *J. Nucl. Mater.* **1989**, *161*, 210-215.

27. Kidd, T.; O'Shea, A.; Boyle, K.; Wallace, J.; Strauss, L. Synthesis of Freestanding HfO_2 Nanostructures. *Nanoscale Research Lett.* **2011**, *6*, 294.

28. Saibene, S.; Butz, T.; Lerf, A. Thermal Decomposition and Oxidation of $HfTe_5$ Single Crystals. *Ber. Bunsenges. Phys. Chem.* **1989**, *93*, 1359-1362.

29. Furuseth, S.; Brattås, L.; Kjekshus, A.; Enzell, C.; Enzell, C.; Swahn, C. The Crystal Structure of $HfTe_5$. *Acta Chem. Scand.* **1973**, *27*, 2367-2374.

30. Feng, T.; Wu, X.; Yang, X.; Wang, P.; Zhang, L.; Du, X.; Wang, X.; Pantelides, S. Thermal Conductivity of $HfTe_5$: A Critical Revisit. *Adv. Funct. Mater.* **2020**, *30*, 1907286

31. Binnewies, M.; Schmidt, M.; Schmidt, P. Chemical Vapor Transport Reactions - Arguments for Choosing a Suitable Transport Agent. *Z. fur Anorg. Allg. Chem.* **2017**, *643*, 1295-1311.

32. Tan, R.; Azuma, Y.; Kojima, I. Comparative Study of the Interfacial Characteristics of Sputter-Deposited HfO_2 on Native SiO_2/Si (100) Using in situ XPS, AES and GIXR. *Surf. Interface Anal.* **2006**, *38*, 784-788.

33. Yang, L.; Wu, H.; Zhang, W.; Chen, Z.; Li, J.; Lou, X.; Xie, Z.; Zhu, R.; Chang, H. Anomalous Oxidation and Its Effect on Electrical Transport Originating from Surface Chemical Instability in Large-Area, Few-Layer 1T′-$MoTe_2$ Films. *Nanoscale* **2018**, *10*, 19906-19915.

34. Toh, R.; Sofer, Z.; Pumera, M. Catalytic Properties of Group 4 Transition Metal Dichalcogenides (MX_2; M = Ti, Zr, Hf; X = S, Se, Te). *J. Mater. Chem. A* **2016**, *4*, 18322-18334.

35. Huang, J.; Hsu, H.; Wang, D.; Lin, W.; Cheng, C.; Lee, Y.; Hou, T. Polymorphism Control of Layered $MoTe_2$ through Two-Dimensional Solid-Phase Crystallization. *Sci. Rep.* **2019**, *9*, 8810.

36. Moulder, J. F.; Sticle, W. F.; Sobol, P. E.; Bomben, K. D. Handbook of X-ray Photoelectron Spectroscopy, Perkin-Elmer: **1993**.

CHAPTER 3

CRYSTAL GROWTH OF ALLOYED GROUP IV TRANSITION METAL TRITELLURIDES

Matthew D. Seivert and Tina T. Salguero. To be submitted to *Crystal Growth & Design*.

Abstract

Solid solutions of single crystalline $Hf_xZr_{1-x}Te_3$ were obtained via the chemical vapor transport (CVT) route at 750 °C (x = 0.20), 675 °C (x = 0.40), and 530 °C (x = 0.80). Synthetic pathways were developed by leveraging the favored synthetic conditions of both $HfTe_3$ and $ZrTe_3$, especially with increasing Hf percentage. We found $Hf_{0.20}Zr_{0.80}Te_3$ was readily isolated using elemental precursors, while polycrystalline $HfTe_3$ and $ZrTe_3$ precursors were necessary for crystal growth and phase isolation of both $Hf_{0.40}Zr_{0.60}Te_3$ and to $Hf_{0.80}Zr_{0.20}Te_3$. Single crystal x-ray diffraction for $Hf_{0.80}Zr_{0.20}Te_3$ shows that this composition crystallizes in the monoclinic space group $P2_1/m$ with lattice parameters a = 5.8765(7) Å, b = 3.9052(5) Å, c = 10.0684(12), β = 97.901(4), V = 228.87(5) Å^3, and Z = 2. X-ray photoelectron spectroscopy (XPS) for $Hf_{0.80}Zr_{0.20}Te_3$ presented shifts in binding energy due to Hf/Zr alloying in addition to confirmation of Hf/Zr—Te, Hf/Zr—O, and Te—O bonding environments.

Introduction

Graphene's incredible discovery in 2004 initiated a resurgence of interest in low-dimensional materials, with researchers taking special interest in two-dimensional (2D) and one-dimensional (1D) layered materials. While there are many classes of materials that fit within these categories, workers in the field have focused significantly on the transition metal trichalcogenides (TMTs).[1,2,3,4,5] The TMTs have MX_3 compositions, where M is typically a group IV or group V transition metal, and X is a chalcogen (S, Se, or Te). In general, these materials are composed of MX_6 units that form covalently bonded chains extending down the *b* axis. Based on their structure, the TMTs are referred to as quasi-1D due to the presence of weaker covalent bonds within the perpendicular plane of these atomic chains forming layers, in addition to the confinement of electrons within these chains.[6] Furthermore, these covalently bonded layers are held together by significantly weaker van der Waals interactions making them prone to exfoliation by mechanical and chemical exfoliation techniques. The term quasi-1D makes a distinction between true-1D materials such as Sb_2S_3 and V_2Se_9 whose only covalent bonds are evidenced down their atomic chains.[6,7,8] Beyond their unique structures, the TMTs are characterized by varying characteristics including strong anisotropies, semiconducting behavior, charge density wave (CDW) transitions, and superconductivity.

Thus far, there has been increased interest in general for the modification of TMT materials, including metal alloying such as with $Ta_xNb_{1-x}S_3$, $Ti_xZr_{1-x}S_3$, and $Ti_xNb_{1-x}S_3$.[9,10,11,12,13] It should be noted that workers in the field have dealt with synthetic challenges when alloying. For example, work reported by Tongay and coworkers found chalcogen rejection in $TiS_{3(1-x)}Se_{3x}$ solid solutions beyond $x = 0.08$.[14] Furthermore, beyond modifications, recent work by Zettl and coworkers determined new TMT compositions including $NbTe_3$, VTe_3, and $TiTe_3$ that could be synthesized

in the few- to single-chain limit in multiwalled carbon nanotubes.[15] Although these materials have not been synthesized in bulk, these findings further drive the possibilities of isolating polycrystalline or single crystalline analogs of new TMTs.

Here, we focus on solid solutions involving the group IV transition metal tritellurides $HfTe_3$ and $ZrTe_3$ because they both exhibit unique electronic properties, including the coexistence of both CDW transitions and superconductivity in the absence of physical or chemical modifications.[16,17,18] In addition, Balandin and coworkers recently reported an exceptionally high current density (~100 MA/cm^2) in single crystalline $ZrTe_3$, which surpasses the values for elemental copper (2-3 MA/cm^2).[19,20] Further studies into $ZrTe_3$ have examined how to tune the conditions for superconductivity and CDWs through the application of pressure, the intercalation of transition metals, doping with chalcogen counterparts, and alloying.[21,22,23,24,25,26] Specific studies have involved $Hf_xZr_{1-x}Te_3$ (x=0.01 or 0.05) and $ZrTe_{3-x}Se_x$ (x<0.04) crystals prepared by I_2-mediated CVT.[21,26] Comparatively, previous work with $HfTe_3$ has been much more limited despite the isostructural relationship between both materials. In Chapter 2, we discuss at depth previous reports for $HfTe_3$ and provide insights into isolating this material which we hope will help workers in the field.

In this contribution, we consider the CVT growth of single crystalline solid solutions of $Hf_xZr_{1-x}Te_3$ (where x = 0.25, 0.50, 0.75 are target compositions). We found that relying on the favored synthetic conditions of $HfTe_3$ and $ZrTe_3$ were critical to single crystalline growth and phase isolation. We also report the single crystal x-ray diffraction structure of $Hf_{0.80}Zr_{0.20}Te_3$, finding that compared to single crystalline reports for $HfTe_3$ and $ZrTe_3$, the lattice parameter *a* is slightly lower than both analogs, but the parameters *b* and *c* were between reported values. We noted the bond lengths and bond angles of the Hf/Zr metal site coordinated to six Te atoms, and

determined they were also between the reported ranges of single crystalline $HfTe_3$ and $ZrTe_3$. These findings confirm structural deviations from both $HfTe_3$ and $ZrTe_3$ due to the alloying of these analogs. XPS analysis confirms the presence of Hf/Zr—Te bonding environments in our sample, shifts in binding energy as a result of metal alloying, and evidence of surface oxidation. Finally, we report preliminary results for single crystalline attempts at $Ti_xZr_{1-x}Te_3$ (x = 0.25, 0.50) and $Ti_xHf_{1-x}Te_3$ (x = 0.25)

Experimental

Materials: Zr foil (0.025 mm thickness, annealed, 99.8% metals basis excluding Hf) and Hf foil (0.25 mm thickness, annealed, 99.5% metals basis excluding Zr) were purchased from Alfa Aesar. Te powder (~200 mesh, 99.8% trace metals basis), crystalline Ti pieces (5-10 mm, ≥ 99.99% trace metals basis), and NH_4Cl (≥ 99.5%) were obtained from Sigma Aldrich. I_2 (crystals, 99.9% purity) was obtained from J.T. Baker Company. HNO_3 (15.8 M, Certified ACS Plus) was obtained from Fisher Chemical.

Ampule Preparation: Two sizes of fused quartz glass ampules were used in this work. "Solid state ampules": body dimensions of 90 mm length, 19 mm inner diameter, 22 mm outer diameter, volume ~33 cm^3; neck dimensions of 170 mm length, 7 mm inner diameter, 9.6 mm outer diameter. "CVT ampules": body dimensions of 175 mm length, 10 mm inner diameter, 14 mm outer diameter, volume ~13 cm^3; neck dimensions of 170 mm length, 7 mm inner diameter, 9.6 mm outer diameter. Ampules were cleaned by immersing in 15.8 M HNO_3 overnight. Afterwards, they were rinsed 3-5 times with deionized water, and then positioned in a horizontal tube furnace or box furnace and heated at 6 °C min^{-1} to a final temperature of 900 °C for 12 h followed by natural cooling to room temperature.

To apply the carbon coating, the inside of an ampule was rinsed thoroughly with acetone. Then a National brand flame torch (propane and oxygen fuel source) was used to heat the outside of the ampules slowly from bottom to top at ~1400 °C under constant rotation using a glass blowing lathe to assure homogeneous carbon deposition. Upon heating, a black layer immediately covers the inside of the ampule. After cooling to room temperature, the procedure was repeated to deposit an additional layer of carbon.

Solid State Synthesis of $HfTe_3$: 0.954 g (5.34 mmol) Hf foil was cut into mm-sized squares and positioned at the bottom of a carbon-coated solid state quartz ampule in addition to 2.046 g (16.0 mmol) Te powder while exposed to ambient atmosphere. The ampule was evacuated and backfilled with Ar three times using a Schlenk line manifold before being flame sealed under vacuum (~10^{-2} Torr). The evacuated ampule was then placed inside a preheated horizontal tube furnace at 550 °C for either (i) 48 h, followed by quenching by submerging the hot ampule in a salted ice water bath, or (ii) 10 d, followed by cooling to 520 °C at 0.25 °C h^{-1}, and then to 25 °C at 5 °C h^{-1}. The product was isolated as mm-sized, grey/black flakes (2.2852 g collected; 76.17 % isolated yield).

Solid State Synthesis of $ZrTe_3$: 0.385 g (4.22 mmol) Zr foil was cut into mm-sized squares and positioned inside the bottom of a carbon-coated solid state quartz ampule in addition to 1.615 g (12.7 mmol) Te powder while exposed to ambient atmosphere. The ampule was evacuated and backfilled with Ar three times using a Schlenk line manifold before being flame sealed under vacuum (~10^{-2} Torr). The evacuated ampule was placed inside a horizontal tube furnace and heated at 5 °C min^{-1} to a final temperature of 800 °C for 48 h, followed by natural cooling to room temperature. The product was isolated as mm-sized, grey/black flakes (2.5639 g collected; 85.46 % isolated yield).

Crystal Growth of $ZrTe_3$: 0.385 g (4.22 mmol) Zr foil was cut into mm-sized squares and positioned at the bottom of a carbon-coated CVT quartz ampule with 1.615 g (12.7 mmol) Te powder and iodine crystals (~60 mg) while exposed to ambient atmosphere. The ampule was evacuated and backfilled with Ar three times using a Schlenk line manifold while submerged in an acetonitrile/dry ice bath before being flame sealed under vacuum (~10^{-2} Torr). The evacuated ampule was positioned inside a horizontal tube furnace and heated at 10 °C min^{-1} to a final temperature gradient of 850-750 °C for 7 d followed by natural cooling to room temperature. The product was isolated as mm-sized, silver hexagonal plates.

Crystal Growth of $Hf_xZr_{1-x}Te_3$: for x = 0.25, 0.50, and 0.75 target compositions, stoichiometric masses of as-prepared $HfTe_3$ and $ZrTe_3$ (solid state syntheses) were lightly ground into fine powders using an agate mortar and pestle inside an Ar glovebox. For $Hf_xZr_{1-x}Te_3$ where x = 0.50, specifically, 1.60 g (2.85 mmol) of as-prepared polycrystalline $HfTe_3$ and 1.35 g (2.85 mmol) of as-prepared polycrystalline $ZrTe_3$ was lightly ground into a homogeneous, fine powder using an agate mortar and pestle inside an Ar glovebox. The ground powders were then ball milled together under Ar atmosphere for 1 h (Fritsch Pulverisette 6 planetary ball mill using about thirty 10-mm Si_3N_4 balls in an 80 mL Si_3N_4 milling bowl at 300 rpm). Upon completion, the milling bowl was opened inside an Ar glovebox to avoid combustion. The ground $HfTe_3/ZrTe_3$ mixtures (1.0230 g) were transferred to carbon-coated CVT quartz ampules with iodine crystals (~60 mg). The ampules were evacuated and backfilled with Ar three times using a Schlenk line manifold while submerged in an acetonitrile/dry ice bath before being flame sealed under vacuum (~10^{-2} Torr). The evacuated ampules were then positioned inside a preheated horizontal tube furnace to final temperature gradients (750–650 °C for $Hf_{0.20}Zr_{0.80}Te_3$; 675–575 °C for $Hf_{0.40}Zr_{0.60}Te_3$; 530–500 °C for $Hf_{0.80}Zr_{0.20}Te_3$) based on the target compositions of the materials for 14 d followed by

natural cooling to room temperature. These syntheses resulted in mm-sized, silver, hexagonal plates. Isolated yields of $Hf_{0.20}Zr_{0.80}Te_3$, $Hf_{0.40}Zr_{0.60}Te_3$, and $Hf_{0.80}Zr_{0.20}Te_3$ crystals were 1.8322 g (83.26 %), 0.2236 g (21.86 %), and 0.6360 g (56.04 %), respectively.

Crystal Growth of $Ti_xZr_{1-x}Te_3$: for x = 0.25 and 0.50 target compositions, stoichiometric masses of elemental precursors were used. For $Ti_xZr_{1-x}Te_3$ where x = 0.50, specifically, 0.1926 g (2.111 mmol) Zr foil was cut into mm-sized squares and positioned at the bottom of a carbon-coated CVT quartz ampule while exposed to ambient atmosphere. In addition, 0.1019 g (2.129 mmol) crystalline Ti pieces, 1.6227 g (12.717 mmol) Te powder, and iodine crystals (~60 mg) were added to the bottom of the ampule while exposed to ambient atmosphere. The ampule was evacuated and backfilled with Ar three times using a Schlenk line manifold while submerged in an acetonitrile/dry ice bath before being flame sealed under vacuum (~10^{-2} Torr). The evacuated ampule was positioned inside a preheated horizontal tube furnace at a final temperature gradient of either 850–750 °C or 750–650 °C for 10 d followed by natural cooling to room temperature.

Crystal Growth of $Ti_xHf_{1-x}Te_3$: for $Ti_xZr_{1-x}Te_3$ where x = 0.25, 0.7107 g (1.266 mmol) of pre-prepared $HfTe_3$ (solid state synthesis) was lightly ground into a fine powder using an agate mortar/pestle inside an Ar-filled glovebox. The resulting powder was ball milled under Ar atmosphere for 1 h (Fritsch Pulverisette 6 planetary ball mill using about thirty 10-mm Si_3N_4 balls in an 80 mL Si_3N_4 milling bowl at 300 rpm). Upon completion, the milling bowl was opened inside the glovebox to avoid combustion. NH_4Cl powder (~30 mg) and 0.0207 g (0.432 mmol) crystalline Ti pieces were transferred to a carbon-coated solid state quartz glass ampule using a funnel, followed by the ground $HfTe_3$. The ampule was evacuated and backfilled with Ar three times using a Schlenk line manifold while submerged in an acetonitrile/dry ice bath before being flame sealed

under vacuum (~10^{-2} Torr). The evacuated ampule was positioned inside a preheated horizontal tube furnace at 530 °C (no gradient) for 14 d followed by natural cooling to room temperature.

Characterization: Powder X-ray diffraction (PXRD) data were collected on a Bruker D8 Advance instrument utilizing a Co−Kα X-ray source (λ = 1.78890 Å) operated at 35 kV and 40 mA. Data was collected from 5 to 80° 2θ with a scan rate of 0.1 s/step. Samples were prepared as powder mounts.

Scanning electron microscopy (SEM) analysis was performed with an FEI Teneo FE-SEM at 10 keV with a spot size of 13. Energy dispersive x-ray spectroscopy (EDS) was performed using an Aztec Oxford Instruments X-MAX^N detector operated at 10 keV with a spot size of 13. Samples were mounted onto a stub with carbon tape and exfoliated using scotch tape. Experimental compositions of $Hf_xZr_{1-x}Te_3$ were determined using average atomic percentages collected via EDS and calculated by normalizing the Te percentage.

For the single crystal X-ray diffraction study on $Hf_{0.80}Zr_{0.20}Te_3$, a silver crystal (with approximate dimensions 0.090 mm × 0.080 mm × 0.040 mm) was mounted on the tip of a glass fiber. The X-ray intensity data were measured at room temperature on a Bruker D8 Quest PHOTON 100 CMOS X-ray diffractometer system with Incoatec Microfocus Source (IμS) monochromated Mo Kα radiation (λ = 0.71073 Å, sealed tube) using phi and omega-scan technique. The data were collected in 2520 frames with 10 second exposure times. Additional details are provided in the Supporting Information.

XPS analysis was accomplished using a Thermo Scientific K-Alpha X-ray Photoelectron Spectrometer System operated with a monochromatic beam of Al Kα x-rays (1486 eV) with a 60 μm spot size. Instrument calibration was completed with Au (4*f*), Ag (3*d*), and Cu (2*p*) standards. The adventitious C 1*s* peak at ~284.9 eV was used for binding energy reference. Samples were

mounted on carbon tape and exfoliated using scotch tape. Peak fitting (Gaussian type) and data analysis were completed using Thermo Scientific Avantage Software.

Raman spectroscopy data was completed using a Thermo Scientific DXR Raman Microscope at 10× magnification with a laser power of 10 mW and a 532 nm excitation laser wavelength. Single crystals were mounted on double-sided scotch tape bonded to a glass slide and exfoliated using unattached scotch tape.

Results and Discussion

General Synthetic Considerations: The high affinity of zirconium and hafnium for oxygen (unavoidably present in fused quartz and as oxide impurities) prompted us to use carbon-coated ampules for all syntheses; indeed, we observed heavily oxidized products during early attempts using non-coated ampules.[17,27,28,29,30] In addition, the use of air-free conditions for all reactions is absolutely necessary.

Binary zirconium and hafnium telluride phases include M_3Te, M_3Te_2, M_2Te, M_5Te_4, M_5Te_6, MTe, MTe_2 (fully and sub-stoichiometric), MTe_3, and MTe_5.[31,32,33,34,35,36,37,38,39] Although the chemistry of zirconium and hafnium is often very similar, it is known to diverge in some cases.[40,41] Here we have found that competition between neighboring phases is significantly more problematic for $HfTe_3$ than for $ZrTe_3$. However, the choice of appropriate synthetic conditions can help minimize or even avoid the formation of competing phases during MTe_3 preparation.

CVT growth of $Hf_xZr_{1-x}Te_3$ crystals: Single crystals of alloyed $Hf_xZr_{1-x}Te_3$ (where x = 0.25, 0.50, 0.75 were target compositions) were prepared by leveraging the optimized temperatures for the CVT growth of $HfTe_3$ (530 °C) and $ZrTe_3$ (850 °C). In addition, we found gradient and starting materials to be critical to the success of Hf-rich compositions.

For $Hf_{0.25}Zr_{0.75}Te_3$, CVT growth at 750 °C using a 100 °C gradient, elemental starting materials, and I_2 transport were most suitable for crystal growth. This reaction temperature accommodated the significant Zr component while still obliging the incorporation of Hf. The resulting silver crystals resembled the distorted hexagonal morphology of $HfTe_3$ (Figure 3.1a). EDS analysis provided average atomic percentages (Table S3.6) confirming a composition of $Hf_{0.20}Zr_{0.80}Te_3$. In comparison, the ditelluride phase was favored at a reaction temperature of 850 °C. The resulting hexagonal crystals exhibiting a smooth, platelike morphology (Figure S3.4a and S3.4b) and gold color typical of $HfTe_2$, in addition to the average atomic percentages collected by EDS (Table S3.6) consistent with a composition of $Hf_{0.25}Zr_{0.75}Te_2$.

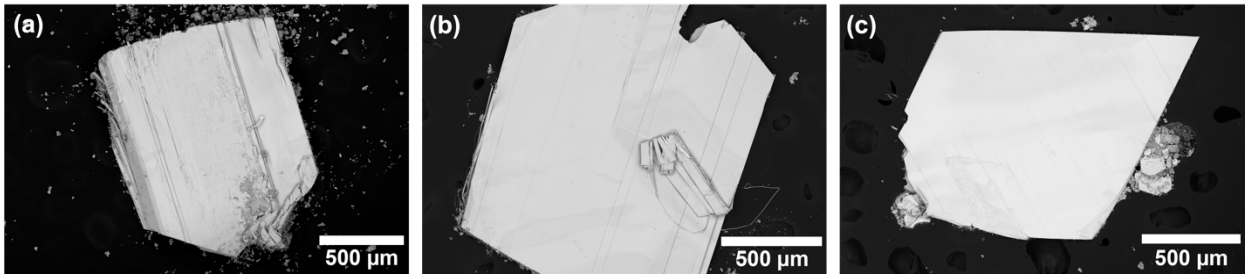

Figure 3.1 SEM imaging of single crystalline (a) $Hf_{0.20}Zr_{0.80}Te_3$, (b) $Hf_{0.40}Zr_{0.60}Te_3$, and (c) $Hf_{0.80}Zr_{0.20}Te_3$.

For $Hf_{0.50}Zr_{0.50}Te_3$, we used similar synthetic parameters as for $Hf_{0.20}Zr_{0.80}Te_3$ (100 °C gradient, I_2 transport) but decreased the temperature to 675 °C to promote Hf incorporation. Experiments showed that crystal growth was enhanced by using pre-made polycrystalline $HfTe_3$ and $ZrTe_3$ precursors instead of the elements. The polycrystalline precursors were ball milled together for 1 h under Ar atmosphere, as in our approach to single crystalline $HfTe_3$. CVT reaction

at these conditions yielded silver crystalline hexagonal plates with striated morphology (Figure 3.1b). EDS confirmed the composition of this phase to be $Hf_{0.40}Zr_{0.60}Te_3$ (Table S3.6).

When identical reaction parameters were used with elemental precursors, we isolated silver crystals with irregular morphologies (Figure S3.4e). Nevertheless, EDS showed that this product was also $Hf_{0.40}Zr_{0.60}Te_3$ (Table S3.6). At a higher temperature of 750 °C vs 675 °C, the resulting hexagonal, silver crystals exhibited familiar surface cleaved morphologies (Figure S3.4c), which EDS analysis confirmed to be the more Zr-rich composition $Hf_{0.20}Zr_{0.80}Te_3$ (Table S3.6). Additionally, the product contained minor gold-colored hexagonal plates (Figure S3.4d) with the ditelluride composition $Hf_{0.30}Zr_{0.70}Te_2$ (Table S3.6).

Even greater Hf incorporation became possible by using ball milled polycrystalline $HfTe_3$ and $ZrTe_3$ precursors and a CVT temperature of 530 °C with a 30 °C gradient. Under these conditions, we isolated hexagonal, silver crystals (Figure 3.1c) exhibiting morphologies in line with $HfTe_3$, $Hf_{0.20}Zr_{0.80}Te_3$, and $Hf_{0.40}Zr_{0.60}Te_3$. EDS analysis confirmed their composition as $Hf_{0.80}Zr_{0.20}Te_3$ (Table S3.6).

Temperature remained a critical parameter for optimum crystal growth even when using polycrystalline tritelluride precursors. At higher temperature (590 °C) and with a larger gradient (100 °C) we noted the presence of both silver hexagonal plates (Figure S3.4f) and golden hexagonal plates (Figure S3.4g). EDS analysis confirmed the silver plates to be $Hf_{0.70}Zr_{0.30}Te_3$ (Table S3.6), which is more Zr rich compared to crystals grown at lower temperature with smaller gradient. In addition, analysis of the gold plates confirmed their composition as $HfTe_2$ with negligible Zr incorporation (Table S3.6).

Synthetic experiments also confirmed the necessity of using polycrystalline $HfTe_3$ and $ZrTe_3$ precursors; using identical reaction conditions (530 °C, 30 °C gradient, I_2 transport),

elemental precursors yielded crystalline, silver wires (Figure S3.4h and Figure S3.4i). EDS analysis confirmed that the wires were pentatellurides, either $Hf_{0.55}Zr_{0.45}Te_5$ or $Hf_{0.70}Zr_{0.30}Te_5$ (Table S3.6). There was no evidence of the tritelluride phase under these reaction conditions.

Elemental mapping of $Hf_{0.20}Zr_{0.80}Te_3$, $Hf_{0.40}Zr_{0.60}Te_3$, and $Hf_{0.80}Zr_{0.20}Te_3$ single crystal products (Figure S3.5) showed uniform distribution of both the metals and chalcogen.

Table 3.1 Summary of the favored synthetic conditions for single crystalline $HfTe_3$, $ZrTe_3$, $Hf_{0.20}Zr_{0.80}Te_3$, $Hf_{0.40}Zr_{0.60}Te_3$, and $Hf_{0.80}Zr_{0.20}Te_3$.

Target Composition	**Optimized Synthetic Conditions**		**Experimental Result**
	Precursors	**CVT Temperature**	
$HfTe_3$	polycrystalline $HfTe_3$ ball milled for 1 h (Ar atmosphere)	530 °C (no gradient)	$HfTe_3$
$ZrTe_3$	elements	850 → 750 °C	$ZrTe_3$
$Hf_{0.25}Zr_{0.75}Te_3$	elements	750 → 650 °C	$Hf_{0.20}Zr_{0.80}Te_3$
$Hf_{0.50}Zr_{0.50}Te_3$	polycrystalline $HfTe_3$ and $ZrTe_3$ ball milled for 1 h (Ar atmosphere)	675 → 575 °C	$Hf_{0.40}Zr_{0.60}Te_3$
$Hf_{0.75}Zr_{0.25}Te_3$	polycrystalline $HfTe_3$ and $ZrTe_3$ ball milled for 1 h (Ar atmosphere)	530 → 500 °C	$Hf_{0.80}Zr_{0.20}Te_3$

Crystal Structure of $Hf_{0.80}Zr_{0.20}Te_3$: Single crystals of $Hf_{0.80}Zr_{0.20}Te_3$ were used to collect high quality x-ray diffraction data. Similar to its analogs, $Hf_{0.80}Zr_{0.20}Te_3$ crystallizes in the monoclinic $P2_1/m$ space group. In Table S3.5, we report the lattice parameters for $Hf_{0.80}Zr_{0.20}Te_3$ compared to $HfTe_3$ and $ZrTe_3$. Overall, the lattice parameters of these compositions fall within 1% of each other, confirming structural similarities.

We also report the bond lengths and bond angles of $Hf_{0.80}Zr_{0.20}Te_3$ versus $HfTe_3$ and $ZrTe_3$ in Tables S3.3 and S3.4. Comparison was made from the *c* axis (Figure S3.3) where the view of the metal center is coordination to six Te atoms. Hf/Zr—Te bond lengths were between ranges for $HfTe_3$ and $ZrTe_3$. Furthermore, a comparison of varying Te—Hf/Zr—Te bond angles were between expected values for both $HfTe_3$ and $ZrTe_3$, further confirming structural similarities. The structure of $Hf_{0.80}Zr_{0.20}Te_3$ is illustrated in Figure 3.2 in which Hf—Zr and select Te—Hf/Zr—Te bonding distances are illustrated. Estimated Hf—Hf, Hf—Te, Zr—Zr, and Zr—Te bonding distances are also shown which were derived from prior single crystalline $HfTe_3$ and $ZrTe_3$ reports.[16,20] Data tables for atomic coordinates and anisotropic displacement parameters are reported in Tables S3.1 and S3.2.

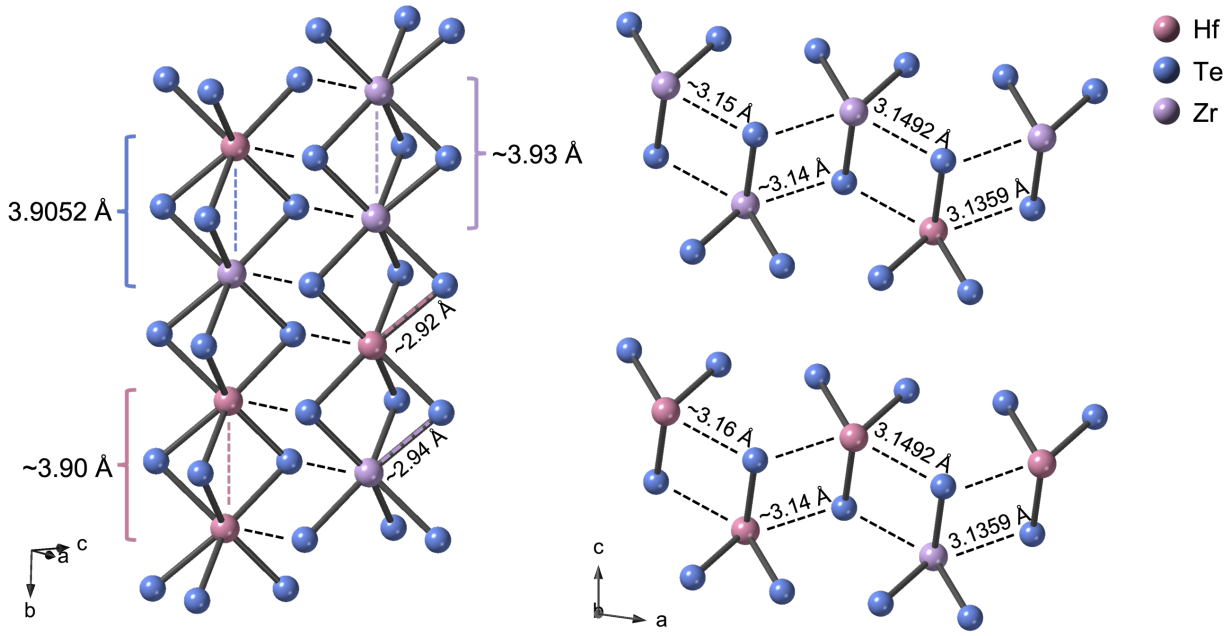

Figure 3.2 Crystal structure of $Hf_{0.80}Zr_{0.20}Te_3$ illustrating bonding distances from experimental single crystal data and estimated bonding distances for $HfTe_3$ and $ZrTe_3$.

XPS Analysis of $Hf_{0.80}Zr_{0.20}Te_3$: XPS of $Hf_{0.80}Zr_{0.20}Te_3$ single crystals provided information about their local bonding environments. A comprehensive list of experimental binding energies and additional information is provided in Table S3.7.

Two doublet Hf 4*f* peaks are present as illustrated in Figure 3.3a. Comparatively, Chen and coworkers found Hf 4*f* peaks for single crystalline $HfTe_3$ at 17.7 eV ($4f_{7/2}$), 19.5 eV ($4f_{5/2}$), 15.7 eV ($4f_{7/2}$), and 17.4 eV ($4f_{5/2}$).[16] In comparison, we note a slight shift to reduced binding energy due to Zr substitution. For Zr 3*d*, two doublets appear as illustrated in Figure 3.3b. We also can compare our data to that reported by Zhang and coworkers for $ZrTe_3$, which exhibited two Zr 3*d* doublets at 183.2 eV ($3d_{5/2}$), 185.6 eV ($3d_{3/2}$), 180 eV ($3d_{5/2}$), and 182.4 eV ($3d_{3/2}$).[42] In addition Petrovic and coworkers reported two Zr 3*d* doublets for $Hf_{0.05}Zr_{0.95}Te_3$ at 183.0 eV ($3d_{5/2}$), 185.4 eV ($3d_{3/2}$), 180 eV ($3d_{5/2}$), and 182.4 eV ($3d_{3/2}$).[26] We note a downward shift in the higher energy peaks as Hf incorporation increases comparatively from $ZrTe_3$, to $Hf_{0.05}Zr_{0.95}Te_3$, to $Hf_{0.80}Zr_{0.20}Te_3$. For the lower energy peaks, we note a negligible difference between $ZrTe_3$ to $Hf_{0.05}Zr_{0.95}Te_3$, but a slightly higher shift for $Hf_{0.80}Zr_{0.20}Te_3$.

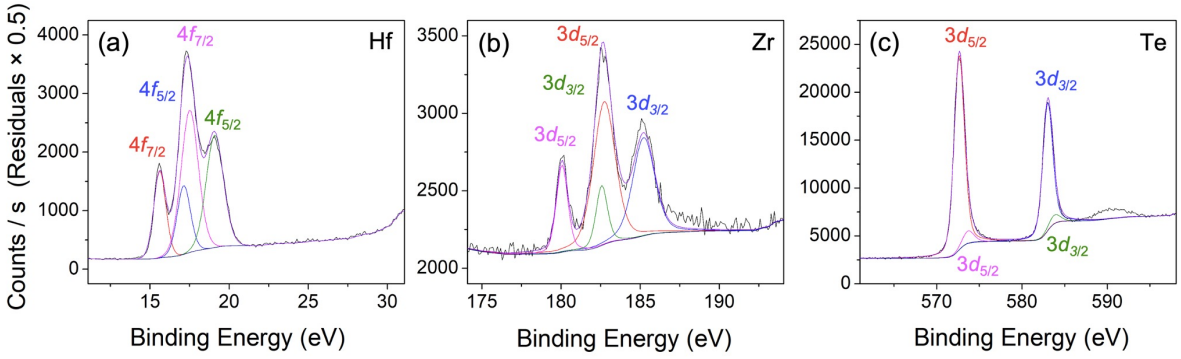

Figure 3.3 XPS spectra of (a) Hf 4*f* (b) Zr 3*d* and (c) Te 3*d* collected from $Hf_{0.80}Zr_{0.20}Te_3$ crystals.

We hypothesize the lower energy Hf 4*f* doublets and Zr 3*d* doublets correspond to Hf/Zr—Te bonding based on previous reports. In addition, we believe the higher energy Hf 4*f* doublets and Zr 3*d* doublets correspond to Hf/Zr—O bonding. Oxidation was indicated by the presence of O 1*s* peaks (Figures S3.8a) which we found corresponding to HfO_2 which has a reported peak at 531.4 eV, and ZrO_2, with a reported peak at 530.0 eV.[43,44] Furthermore, we found in related studies that oxidation of transition metal chalcogenide materials (e.g. $MoTe_2$, $TiTe_2$, ZrS_2, HfS_2, etc.) causes an upward shift in binding energy due to the introduction of M—O (M = metal) bonding.[45,46,47] Work by Pumera and coworkers specifically cited Zr^{4+} and Hf^{4+} in pristine ZrS_2 and HfS_2 and the subsequent shift in higher binding energy due to oxide environments while under identical oxidation states.[46]

For Te 3*d*, two doublets are present as illustrated in Figure 3.3c. We compared binding energies to work from Zhang and coworkers in which they reported three Te 3*d* doublets for $ZrTe_3$ at 573.0 eV ($3d_{5/2}$), 583.4 eV ($3d_{3/2}$), 572.1 eV ($3d_{5/2}$), 582.5 eV ($3d_{3/2}$), 573.9 eV ($3d_{5/2}$), and 584.2 eV ($3d_{3/2}$).[42] We also note work from Chen and coworkers in which they reported two Te 3*d* doublets for $HfTe_3$ at 572.7 eV ($3d_{5/2}$), 583.1 eV ($3d_{3/2}$), 576.9 eV ($3d_{5/2}$), and 587.3 eV ($3d_{3/2}$).[16] We note that the lower energy peaks in our work with $Hf_{0.80}Zr_{0.20}Te_3$ shifted to lower binding energies with Hf/Zr alloying, which we believe correlated to Hf/Zr—Te bonding. We also hypothesize that the higher energy Te 3*d* peaks were a result of Te—O bonding in our samples. The shift to higher binding energies because of oxidation is not limited to M—O bonding, with findings of the same behavior occurring in Te—O bonding also in previous reports.[45,47] Although single crystals were surface exfoliated with tape prior to analysis, the persistent presence of M—O and Te—O bonding is consistent with the susceptibility of $Hf_{0.80}Zr_{0.20}Te_3$ to oxidation.

Finally, we report the experimental spin-orbit splitting separations for Hf 4*f* (1.58 eV and 1.51 eV), Zr 3*d* (2.49 eV and 2.50 eV), and Te 3*d* (10.36 eV and 10.10 eV) which slightly deviated from expected values (1.71 eV for Hf 4*f*, 2.43 eV for Zr 3*d*, 10.39 eV for Te 3*d*).[48]

Raman Analysis of $Hf_xZr_{1-x}Te_3$ Single Crystals: Raman analysis was collected for $Hf_{0.20}Zr_{0.80}Te_3$, $Hf_{0.40}Zr_{0.60}Te_3$, and $Hf_{0.80}Zr_{0.20}Te_3$ single crystals as illustrated in Figure S3.9. We compared Raman peaks collected for $ZrTe_3$ which were also collected at an excitation wavelength of 532 nm by Zhang and coworkers. They found Raman peaks at 107 cm^{-1}, 142 cm^{-1}, and 213 cm^{-1} consistent with A_g Raman modes corroborating the peaks we found in our solid solution samples with slight shifts due to metal alloying.[42]

CVT growth of $Ti_xZr_{1-x}Te_3$ and $Ti_xHf_{1-x}Te_3$ crystals: In addition to compositions of $Hf_xZr_{1-x}Te_3$ ($0 \leq x \leq 1$), we also attempted Ti incorporation into $ZrTe_3$ and $HfTe_3$. As already noted, $TiTe_3$ has not been synthesized in the bulk, prompting us to use the favored conditions of $ZrTe_3$ and $HfTe_3$. For $Ti_{0.25}Zr_{0.75}Te_3$, CVT growth at 850 °C using a 100 °C gradient, elemental starting materials, and I_2 transport resulted in a very minimal yield of silver crystals (Figure S3.10a and Figure S3.10b) and significant oxidation. Using EDS analysis, we found the compositions of the crystals were $Ti_{0.02}Zr_{0.98}Te_3$ (Table S3.8) indicating minimal Ti incorporation into $ZrTe_3$. Elemental mapping illustrated that although Ti incorporation was miniscule, it was not limited to the edge of the products, but was indeed homogeneous throughout (Figure S3.11). We also found a crystal with a hexagonal platelike morphology (Figure S3.10c) that was the $Ti_{0.60}Zr_{0.40}Te_2$ phase as confirmed by EDS (Table S3.8).

We also tried targeting $Ti_{0.50}Zr_{0.50}Te_3$ with the hypothesis that increased stoichiometric Ti would result in crystals with higher Ti percentage. When implementing CVT growth at both 850 and 750 °C using a 100 °C gradient, elemental starting materials, and I_2 transport, we isolated

silver crystals with hexagonal platelike morphologies (Figure S3.10d and Figure S3.10e) that were either $Ti_{0.98}Zr_{0.02}Te_2$ or $TiTe_2$ based on EDS analysis (Table S3.8). Significant oxidation was also present in this sample.

Finally, we targeted $Ti_{0.25}Hf_{0.75}Te_3$ by implementing CVT growth at 530°C in the absence of a temperature gradient and using NH_4Cl transport. In addition, polycrystalline $HfTe_3$ which was ball milled under Ar atmosphere for 1 h was used with crystalline Ti pieces. As a result, silver crystals of varying morphologies were collected (Figure S3.10f, Figure S3.10g, Figure S3.10h, and Figure S3.10i). EDS analysis confirmed the compositions were either $Ti_{0.80}Hf_{0.20}Te_2$ and $Ti_{0.70}Hf_{0.30}Te_2$ (Table S3.8).

Conclusions

In this contribution, we have described successful approaches in three $Hf_xZr_{1-x}Te_3$ solid solutions (x = 0.20, 0.40, 0.80) largely by leveraging the chemistry of $HfTe_3$ and $ZrTe_3$. The optimized formation of each solid solution composition occurred at a different temperature (from 750–530 °C), and starting materials and temperature gradient were also critical for crystal growth and single phase isolation. More specifically, our results demonstrate the need to tailor synthetic conditions with increasing Hf incorporation, and shows how the chemistry of $Hf_xZr_{1-x}Te_3$ solid solutions changes as the overall composition is tuned. Single crystal x-ray diffraction established the structure of $Hf_{0.80}Zr_{0.20}Te_3$, whereas XPS analysis elucidated local bonding environments as a function of metal alloying. This work provides routes in isolating $Hf_xZr_{1-x}Te_3$ solid solutions, and sheds light in experiment design specifically with solid solutions, thereby providing insight into other TMT alloying possibilities.

Supporting Information

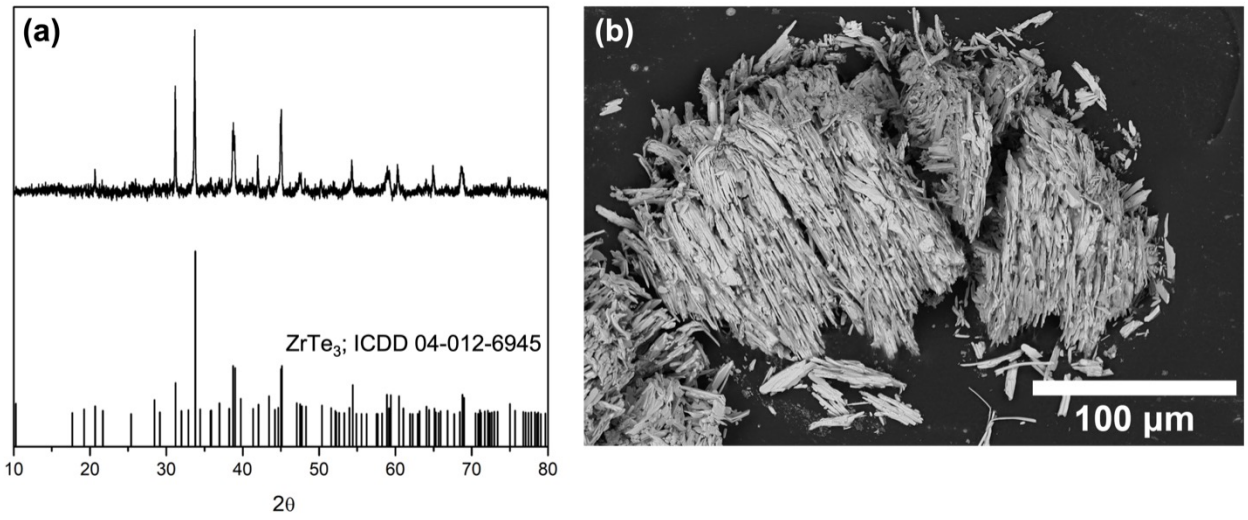

Figure S3.1 (a) PXRD and (b) SEM of polycrystalline $ZrTe_3$ synthesized via solid state reaction.

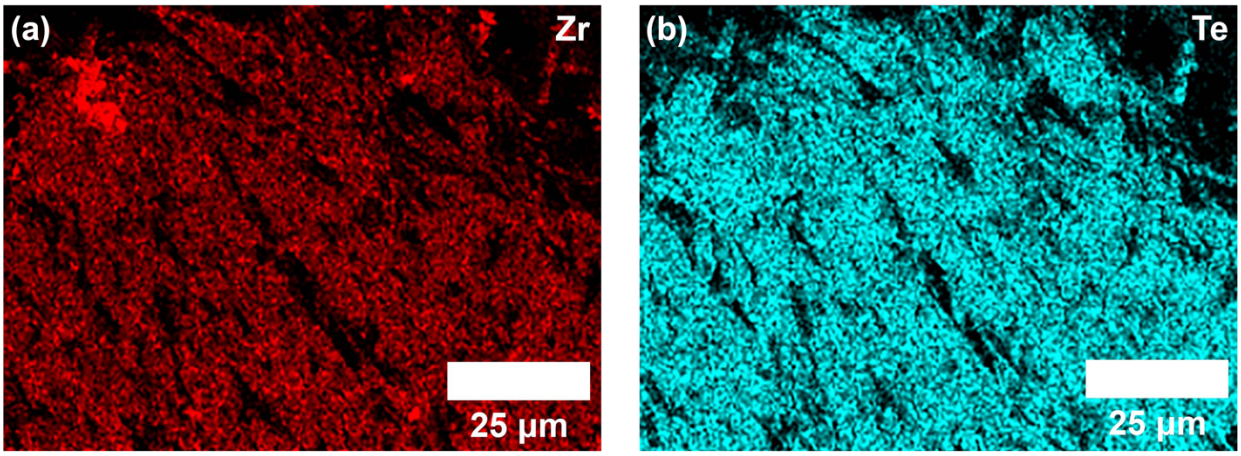

Figure S3.2 Elemental mapping of $ZrTe_3$ illustrating elemental distribution of (a) Zr and (b) Te.

Experimental details for the single crystal x-ray diffraction structure determination of $Hf_{0.80}Zr_{0.20}Te_3$:

Data reduction[1]: Of the 519 unique reflections collected, 518 were observed ($I > 2\sigma(I)$). The linear absorption coefficient for Mo Kα radiation is 37.239 mm^{-1}. The data were integrated with the manufacturer's SAINT software. Absorption corrections were applied with the Multi-Scan method (SADABS).

Structure solution and refinement[2]: Subsequent solution and refinement were performed using the SHELXTL-2018[3] solution package. The structure was solved by intrinsic phasing method using SHELXTL-2018 Software Package. Non-hydrogen atomic scattering factors were taken from the literature tabulations.[4] Non-hydrogen atoms were located from successive difference Fourier map calculations. Based on the SEM/EDS analysis that suggests the formula is $Hf_{1.60}Zr_{0.40}Te_6$ in the unit cell with Z = 1, the Hf and Zr atoms were constrained to share a same position with the ratio of 0.80/0.20 for Hf/Zr with formula of $Hf_{0.40}Zr_{0.10}Te_{1.5}$ in an asymmetric unit. In the final cycles of each refinement, all the atoms were refined in anisotropic displacement parameters with proper constraints/restraints on Hf and Zr atoms. The crystal system of compound is monoclinic, space group $P2_1/m$ (No. 11) and the final residual values based on 26 variable parameters and 518 observed reflections ($I > 2\sigma(I)$) are $R1$ = 0.0391, $wR2$ = 0.0939, and those for all unique reflections are $R1$ = 0.0392, $wR2$ = 0.0939. The goodness-of-fit indicator for all data is 1.086. Peaks on the final difference map, ranging from 2.102 to -2.302/$Å^3$ around Hf(1) (0.96 Å from Hf(1)) and Te(3) (1.40 Å from Te(3)) atoms, are of no chemical significance. While the absorption correction was extensively exploited to find optimized absorption correction conditions and the remaining electron density residuals were dramatically reduced for this heavily absorbed material, the efforts

have been made to resolve as many alerts as possible generated by CheckCIF. The current highest alert is at level C, which is due to fractional Hf and Zr atoms occupying the same position.

Summary: The compound crystallizes in monoclinic, space group $P2_1/m$ (No. 11). The asymmetric unit contains a component in the form of $Hf_{0.40}Zr_{0.10}Te_{1.5}$ in a polymeric structure with all the atoms residing on symmetries of mirror. The whole formula in the unit cell is in the form of $Hf_{1.60}Zr_{0.40}Te_6$. Structure solution, refinement and the calculation of derived results were performed using the SHELXTL-2018[3] package of computer programs. Neutral atom scattering factors were those of Cromer and Waber[4], and the real and imaginary anomalous dispersion corrections were those of Cromer.[5]

References:

1. Data Reduction:
   Intensity
   $I = [S - B/R]\cdot V$
   Standard Deviation in Intensity
   $s(I) = [S + B/R^2]^{1/2}\cdot V$
   Structure Factor
   $F = (I/Lp)^{1/2}$
   Standard Deviation in Structure Factor
   $\sigma(F) = \sigma(I)/(2\cdot F\cdot Lp)$
   Where: S = total scan count
   B = sum of background counts
   R = ratio of background counting time to scan counting time
   V = scan rate
   Lp = Lorentz-polarization correction

2. Least-Squares Refinement:
   Weighting Scheme
   $w = 1/[\ \sigma^2(F_o^2) + 0.0364*P)^2 + 10.8750*P]$ where $P = [\mathrm{Max}(F_o^2, 0) + 2*F_c^2]/3$;
   Residuals
   R-factors:
   $R = \Sigma\ |\ |F_o|\ -\ |F_c|\ |\ /\Sigma\ |F_o|$;
   Weighted R-factor on F^2:
   $wR2 = [\Sigma[w\ (F_o^2 - F_c^2)^2] / \Sigma[w(F_o^2)^2]]^{1/2}$;
   Goodness of Fit Indicator:
   goodness-of-fit = $[\Sigma[w\ (F_o^2 - F_c^2)^2] /(N_{observns}-N_{params})\ ]^{1/2}$.

3. (a) Sheldrick, G.M. *SHELXTL-2018*, *Crystallographic Computing System*; Bruker Analytical X-Ray Instruments: Madison, WI, 2018; (b) Sheldrick, G.M. *A Short History of SHELX*, Acta Cryst. 2008, A64, 112.

4. Cromer, D.T. and Waber, J.T. International Tables for X-ray Crystallography, Vol. IV, Table 2.2B, The Kynoch Press, Birmingham England, 1974.

5. Cromer, D.T. International Tables for X-ray Crystallography, Vol. IV, Table 2.3.1, The Kynoch Press, Birmingham England, 1974.

Table S3.1 Atomic coordinates (x 10^4) and equivalent isotropic displacement parameters ($Å^2$ x 10^3) for $Hf_{0.80}Zr_{0.20}Te_3$. U_{eq} is defined as 1/3 of the trace of the orthogonalized *Uij* tensor.

Atom	*x*	*y*	*z*	U_{eq}
Hf(1)	7115(2)	7500	3342(1)	30(1)
Zr(1)	7115(2)	7500	3342(1)	30(1)
Te(1)	7634(2)	2500	5540(1)	26(1)
Te(2)	4311(2)	2500	1677(1)	29(1)
Te(3)	9064(2)	2500	1624(1)	29(1)

Table S3.2 Anisotropic displacement parameters (A^2 x 10^3) for $Hf_{0.80}Zr_{0.20}Te_3$. The anisotropic displacement factor exponent takes the form: -2 pi^2 [h^2 a*^2 U11 + ... + 2 h k a* b* U12].

Atom	U11	U22	U33	U23	U13	U12
Hf(1)	33(1)	24(1)	31(1)	0	4(1)	0
Zr(1)	33(1)	24(1)	31(1)	0	4(1)	0
Te(1)	30(1)	23(1)	26(1)	0	3(1)	0
Te(2)	29(1)	24(1)	33(1)	0	3(1)	0
Te(3)	31(1)	25(1)	32(1)	0	7(1)	0

Table S3.3 Selected bond length comparison for $HfTe_3$, $Hf_{0.80}Zr_{0.20}Te_3$, and $ZrTe_3$.

	$HfTe_3$ Bond Lengths (Å)	**$Hf_{0.80}Zr_{0.20}Te_3$ Bond Lengths (Å)**	**$ZrTe_3$ Bond Lengths (Å)**
M-Te^1; M-Te^4	2.9258(4)	2.9292(12)	2.9399(4)
M-Te^2; M-Te^5	2.9296(5)	2.9353(11)	2.9564(4)
M-Te^3; M-Te^6	2.9416(5)	2.9435(12)	2.9593(4)

Table S3.4 Selected bond angle comparison for $HfTe_3$, $Hf_{0.80}Zr_{0.20}Te_3$, and $ZrTe_3$.

	$HfTe_3$ Bond Angles (°)	**$Hf_{0.80}Zr_{0.20}Te_3$ Bond Angles (°)**	**$ZrTe_3$ Bond Angles (°)**
∠Te^1-M-Te^2 ∠Te^4-M-Te^5	88.73(6)	88.86(3)	88.957(8)
∠Te^2-M-Te^3 ∠Te^5-M-Te^6	89.48(5)	89.62(3)	89.870(8)
∠Te^1-M-Te^3 ∠Te^4-M-Te^6	57.19(0)	56.97(3)	56.502(10)

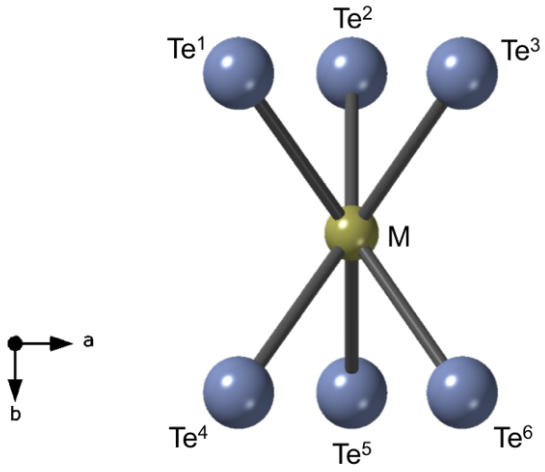

Figure S3.3 Crystal structure of $Hf_{0.80}Zr_{0.20}Te_3$ from the *c* axis illustrating metal coordination (where M = Hf or Zr) to Te.

Table S3.5 Summary of crystallographic data for $HfTe_3$, $Hf_{0.80}Zr_{0.20}Te_3$, and $ZrTe_3$.

Formula	**$HfTe_3$**	**$Hf_{0.80}Zr_{0.20}Te_3$**	**$ZrTe_3$**
F.W. (g/mol)	561.29	543.84	474.02
Crystal system	Monoclinic	Monoclinic	Monoclinic
Space group	$P2_1/m$	$P2_1/m$	$P2_1/m$
Z	2	2	2
a (Å)	5.8845(2)	5.8765(7)	5.8938(3)
b (Å)	3.9026(2)	3.9052(5)	3.9256(2)
c (Å)	10.0551(4)	10.0684(12)	10.1011(5)
α (°)	90	90	90
β (°)	97.945(1)	97.901(4)	97.8200(10)
γ (°)	90	90	90
V (Å^3)	228.70(2)	228.87(5)	231.53(2)
Absorption coefficient (mm^{-1})	Not reported	37.239	20.688
Θ range (°)	2.04-38.97	2.042-25.999	3.489-32.577
hkl ranges	$-10 \le h \le 10$ $-6 \le k \le 6$ $-17 \le l \le 17$	$-7 \le h \le 7$ $-4 \le k \le 4$ $-12 \le l \le 12$	$-8 \le h \le 8$ $-5 \le k \le 5$ $-15 \le l \le 15$
No. reflections; $R_{int.}$	1410; 0.0533	519; 0.0607	939; 0.0308
No. parameters	26	26	26
R_1; wR_2	0.0337; 0.1002	0.0391; 0.0939	0.0201; 0.0611
Goodness of fit	1.224	1.086	1.004
Diffraction peak; hole (e$^-$; Å^3)	Not reported	2.102; -2.302	1.890; -2.329
Temperature (K)	293	295(2)	297(2)
Reference	10	This work	21

Table S3.6 $Hf_xZr_{1-x}Te_3$ reaction list with target compositions, synthetic conditions used, and experimental results calculated using atomic percentages collected via EDS.

Target Composition	Synthetic Conditions	Atomic % by EDS			Experimental Result
		Hf	Zr	Te	
$Hf_{0.25}Zr_{0.75}Te_3$	750 → 650 °C; elements	6.1	20.2	73.7	$Hf_{0.20}Zr_{0.80}Te_3$
$Hf_{0.25}Zr_{0.75}Te_3$	850 → 750 °C; elements	8.7	25.9	65.4	$Hf_{0.25}Zr_{0.75}Te_2$
$Hf_{0.50}Zr_{0.50}Te_3$	675 → 575 °C; polycrystalline $HfTe_3$ and $ZrTe_3$ ball milled for 1 h (Ar atmosphere)	11.2	15.1	73.7	$Hf_{0.40}Zr_{0.60}Te_3$
$Hf_{0.50}Zr_{0.50}Te_3$	675 → 575 °C; elements	11.0	14.9	74.1	$Hf_{0.40}Zr_{0.60}Te_3$
$Hf_{0.50}Zr_{0.50}Te_3$	750 → 650 °C; elements	5.5	20.7	73.9	$Hf_{0.20}Zr_{0.80}Te_3$
		12.7	23.5	63.8	$Hf_{0.30}Zr_{0.70}Te_2$
$Hf_{0.75}Zr_{0.25}Te_3$	530 → 500 °C; polycrystalline $HfTe_3$ and $ZrTe_3$ ball milled for 1 h (Ar atmosphere)	20.1	6.2	73.7	$Hf_{0.80}Zr_{0.20}Te_3$
$Hf_{0.75}Zr_{0.25}Te_3$	590 → 490 °C; polycrystalline $HfTe_3$ and $ZrTe_3$ ball milled for 1 h (Ar atmosphere)	8.5	17.8	73.7	$Hf_{0.70}Zr_{0.30}Te_3$
		34.9	0.2	64.9	$HfTe_2$
$Hf_{0.75}Zr_{0.25}Te_3$	530 → 500 °C; elements	9.4	8.4	82.2	$Hf_{0.55}Zr_{0.45}Te_5$
		11.4	6.2	82.4	$Hf_{0.70}Zr_{0.30}Te_5$

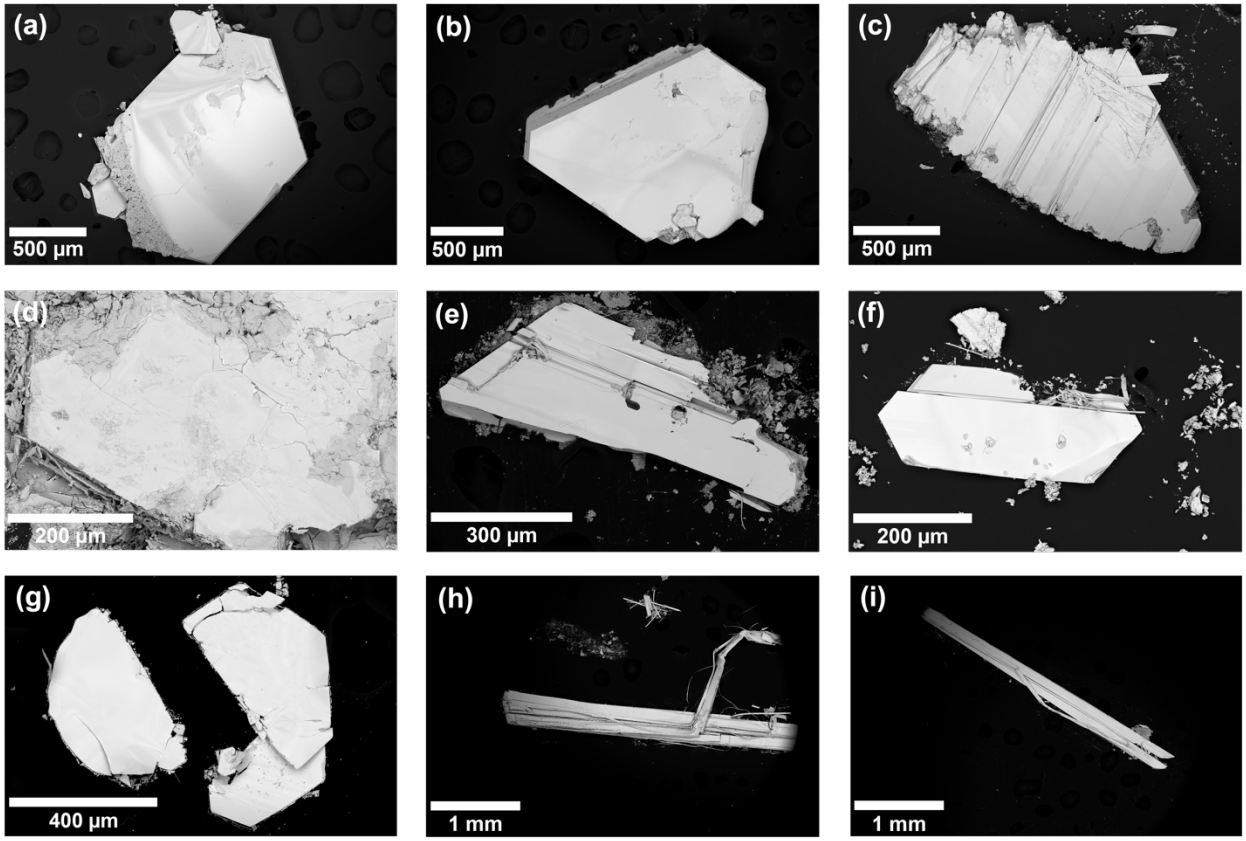

Figure S3.4 SEM imaging of single crystalline: (a)-(b) $Hf_{0.25}Zr_{0.75}Te_2$ from the attempted synthesis of $Hf_{0.25}Zr_{0.75}Te_3$; (c) $Hf_{0.20}Zr_{0.80}Te_3$, (d) $Hf_{0.30}Zr_{0.70}Te_2$, and (e) $Hf_{0.40}Zr_{0.60}Te_3$ from the attempted synthesis of $Hf_{0.50}Zr_{0.50}Te_3$; (f) $Hf_{0.70}Zr_{0.30}Te_3$, (g) $HfTe_2$, (h) $Hf_{0.55}Zr_{0.45}Te_5$, and (i) $Hf_{0.70}Zr_{0.30}Te_5$ from the attempted synthesis of $Hf_{0.75}Zr_{0.25}Te_3$.

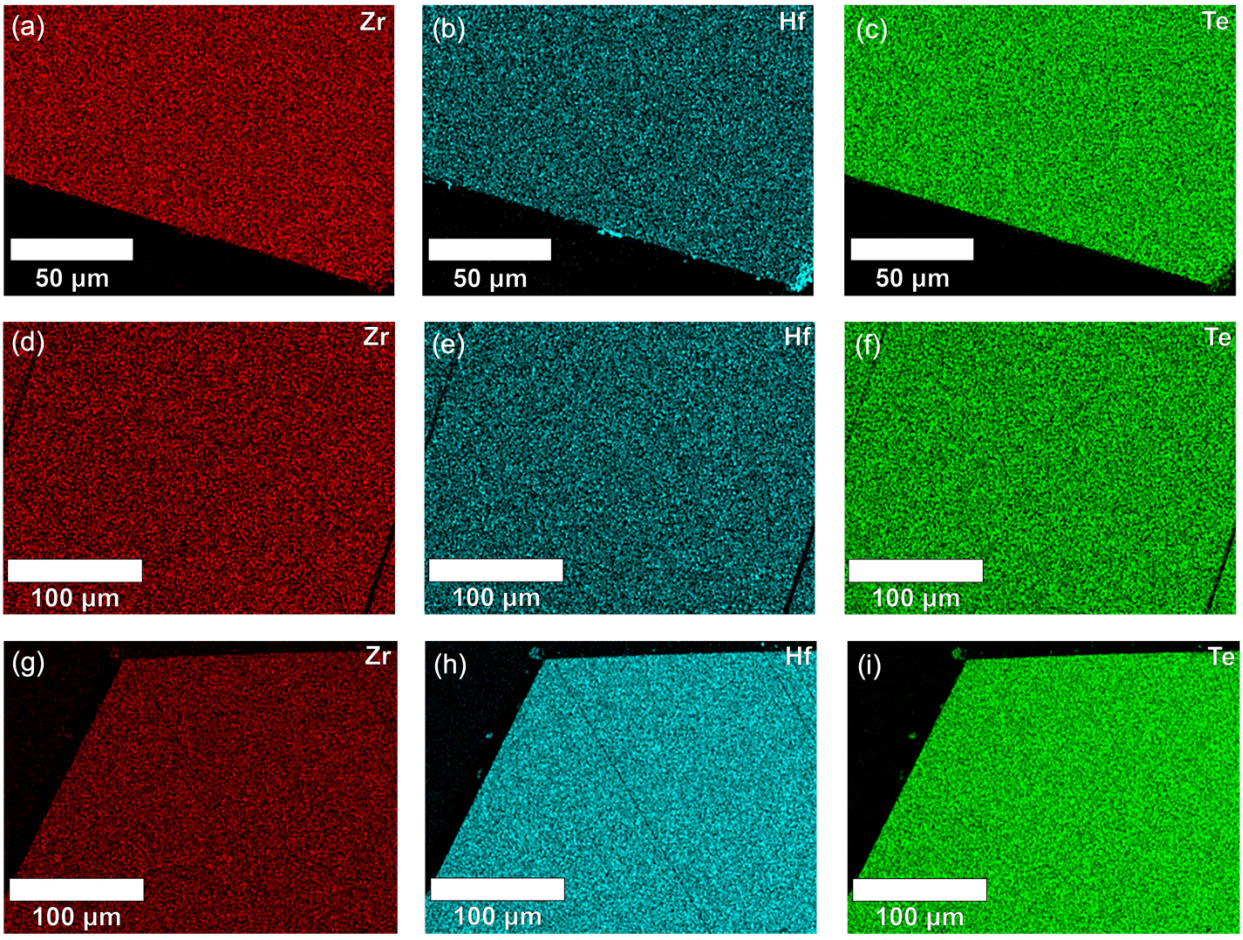

Figure S3.5 Elemental mapping illustrating homogeneous distribution of Zr, Hf, and Te in (a)-(c) $Hf_{0.20}Zr_{0.80}Te_3$, (d)-(f) $Hf_{0.40}Zr_{0.60}Te_3$, (g)-(i) and $Hf_{0.80}Zr_{0.20}Te_3$.

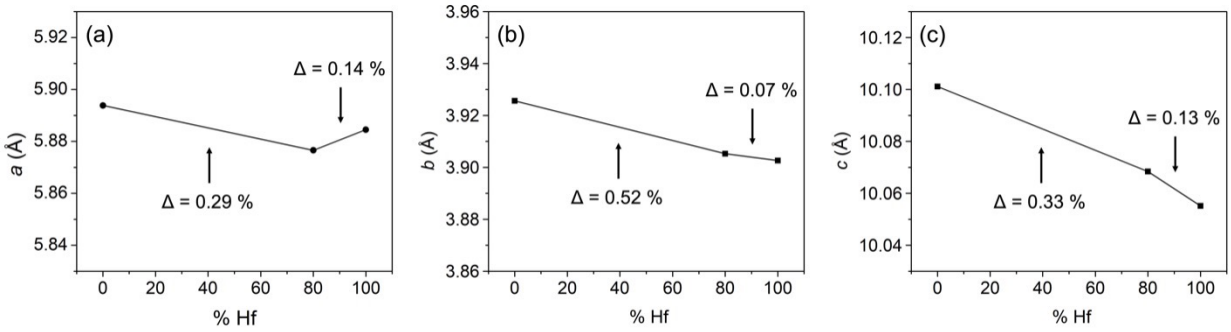

Figure S3.6 Composition plots of $Hf_xZr_{1-x}Te_3$ ($0 \leq x \leq 1$) as a function of increasing Hf percentage vs (a) *a*, (b) *b*, and (c) *c* lattice parameters.

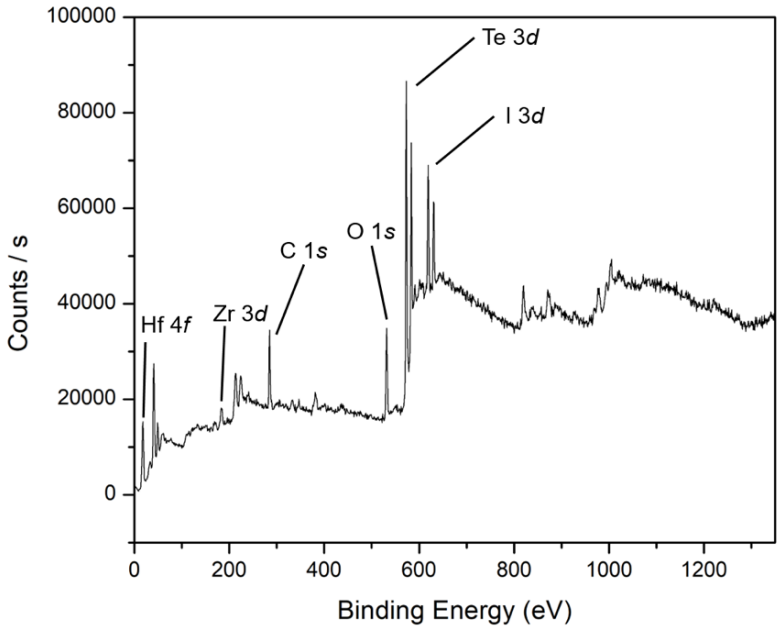

Figure S3.7 XPS survey collected from $Hf_{0.80}Zr_{0.20}Te_3$ crystals.

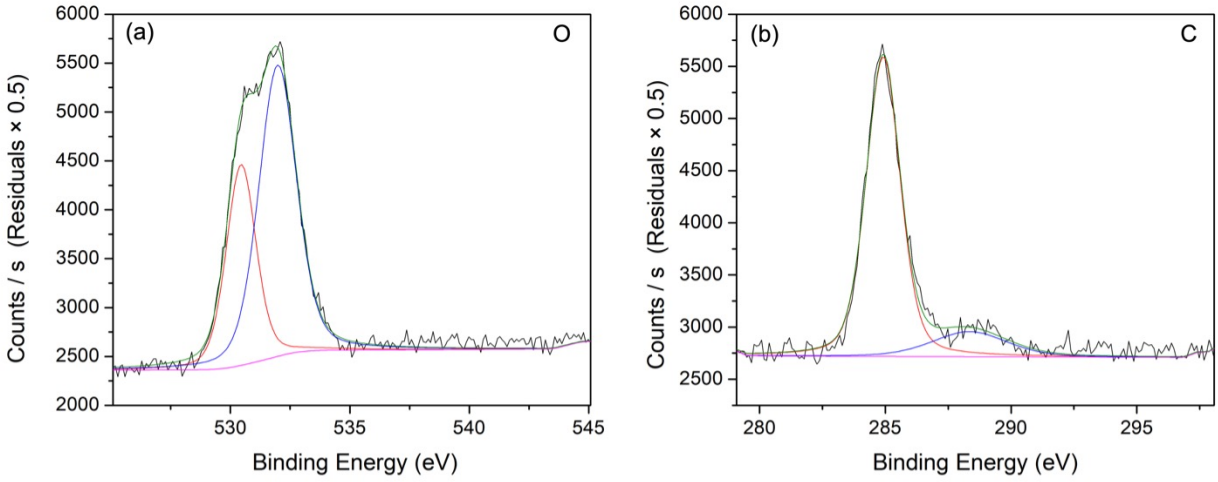

Figure S3.8 XPS spectra of (a) O 1*s* and (b) C 1*s* collected from $Hf_{0.80}Zr_{0.20}Te_3$ crystals.

Table S3.7 XPS peak assignments, binding energies, FWHM values, and atomic percentages collected from $HfTe_3$ and $Hf_{0.80}Zr_{0.20}Te_3$ crystals.

Experimental Result	Assignments	Binding Energies (eV)	FWHM (eV)	Atomic %
$Hf_{0.80}Zr_{0.20}Te_3$	Hf: $4f_{7/2}$, $4f_{5/2}$	17.51, 19.09	1.29, 1.29	5.70, 5.70
	Hf: $4f_{7/2}$, $4f_{5/2}$	15.62, 17.13	0.90, 0.99	2.44, 2.68
	Zr: $3d_{5/2}$, $3d_{3/2}$	182.73, 185.22	1.64, 1.64	3.34, 3.34
	Zr: $3d_{5/2}$, $3d_{3/2}$	180.06, 182.56	0.85, 0.85	1.07, 1.07
	Te: $3d_{5/2}$, $3d_{3/2}$	572.65, 583.01	1.43, 1.38	19.61, 18.17
	Te: $3d_{5/2}$, $3d_{3/2}$	573.70, 583.80	1.61, 1.61	1.41, 1.42
	O: 1*s*	531.98	1.87	22.08
	O: 1*s*	530.45	1.46	11.97

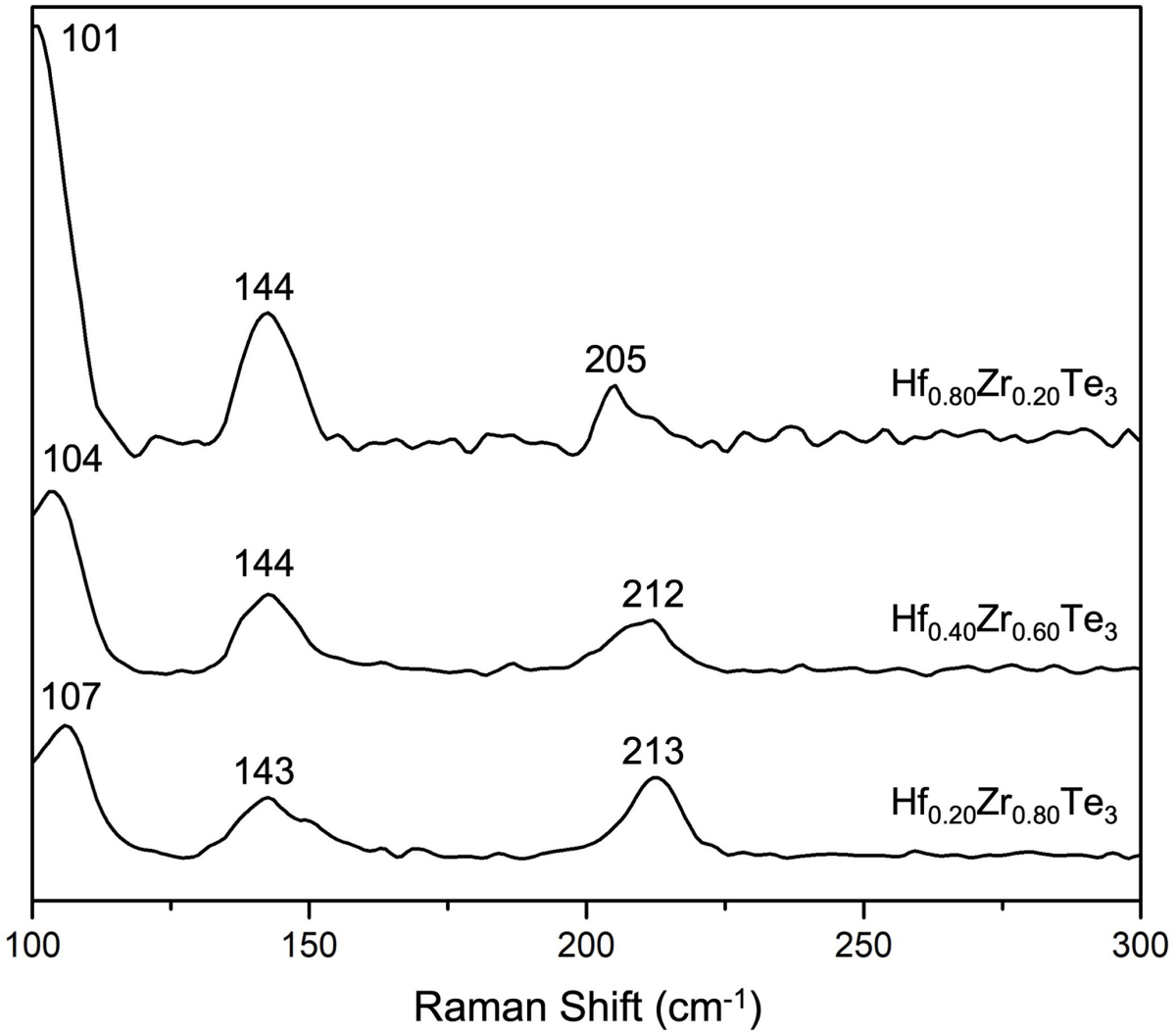

Figure S3.9 Raman spectrum of single crystalline $Hf_{0.20}Zr_{0.80}Te_3$, $Hf_{0.40}Zr_{0.60}Te_3$, and $Hf_{0.80}Zr_{0.20}Te_3$ collected with a 532 nm excitation laser wavelength.

Table S3.8 $Ti_xZr_{1-x}Te_3$ and $Ti_xHf_{1-x}Te_3$ reaction list with target compositions, synthetic conditions used, and experimental results calculated using atomic percentages collected via EDS.

Target Composition	Synthetic Conditions	Atomic % by EDS			Experimental Result
		Ti	Zr	Te	
$Ti_{0.25}Zr_{0.75}Te_3$	850 → 750 °C; elements	0.5	25.0	74.5	$Ti_{0.02}Zr_{0.98}Te_3$
		18.9	14.5	66.6	$Ti_{0.60}Zr_{0.40}Te_2$
$Ti_{0.50}Zr_{0.50}Te_3$	850 → 750 °C; elements	33.0	1.0	66.0	$Ti_{0.98}Zr_{0.02}Te_2$
$Ti_{0.50}Zr_{0.50}Te_3$	750 → 650 °C; elements	32.9	0.0	67.1	$TiTe_2$
$Ti_{0.25}Hf_{0.75}Te_3$	530 °C (no gradient); polycrystalline $HfTe_3$ ball milled for 1 h (Ar atmosphere) + crystalline Ti pieces	27.0	6.2	66.8	$Ti_{0.80}Hf_{0.20}Te_2$
		24.1	9.4	66.5	$Ti_{0.70}Hf_{0.30}Te_2$

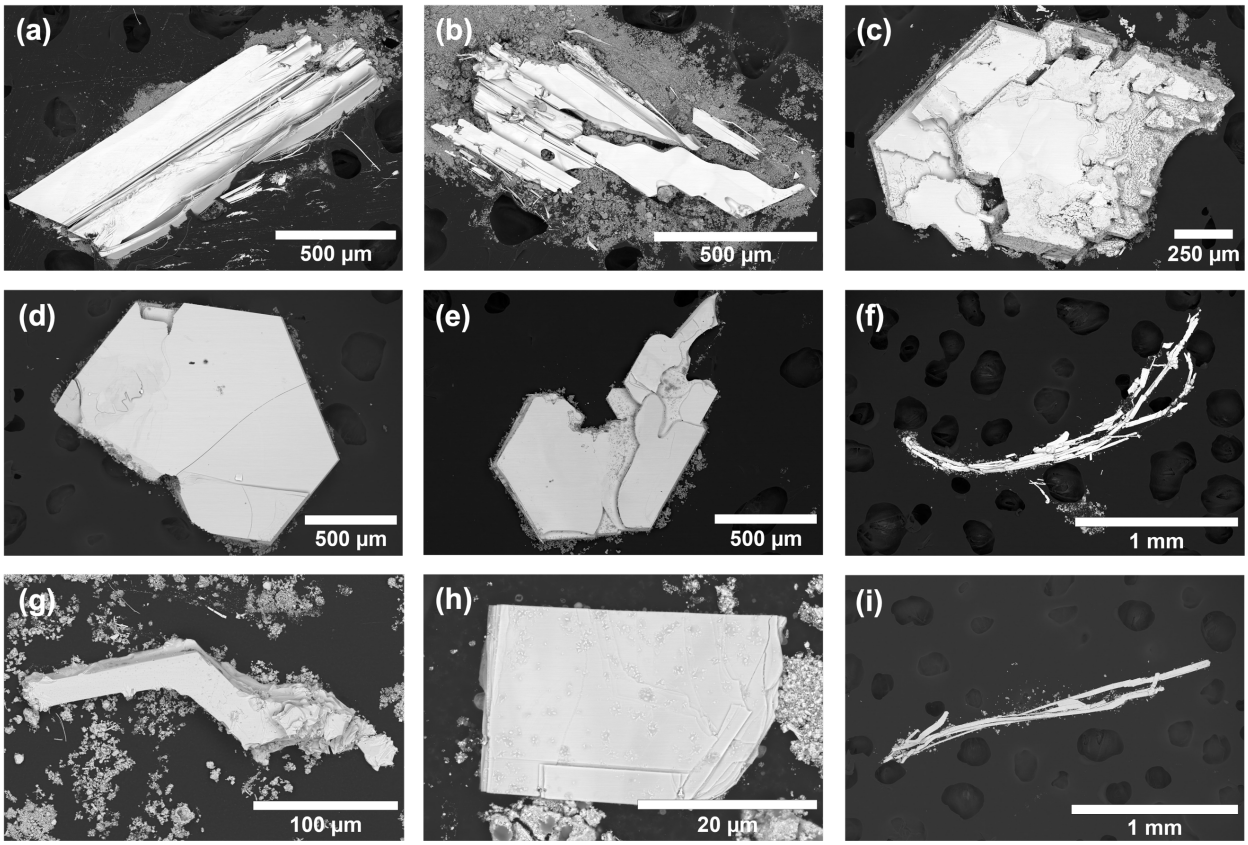

Figure S3.10 SEM imaging of single crystalline: (a)-(b) $Ti_{0.02}Zr_{0.98}Te_3$ and (c) $Ti_{0.60}Zr_{0.40}Te_2$ from the attempted synthesis of $Ti_{0.25}Zr_{0.75}Te_3$; (d) $Ti_{0.98}Zr_{0.02}Te_2$ from the attempted synthesis of $Ti_{0.50}Zr_{0.50}Te_3$; (e) $TiTe_2$ from the attempted synthesis of $Ti_{0.50}Zr_{0.50}Te_3$; (f)-(h) $Ti_{0.80}Hf_{0.20}Te_2$ from the attempted synthesis of $Ti_{0.25}Hf_{0.75}Te_3$; and $Ti_{0.70}Hf_{0.30}Te_2$ from the attempted synthesis of $Ti_{0.25}Hf_{0.75}Te_3$.

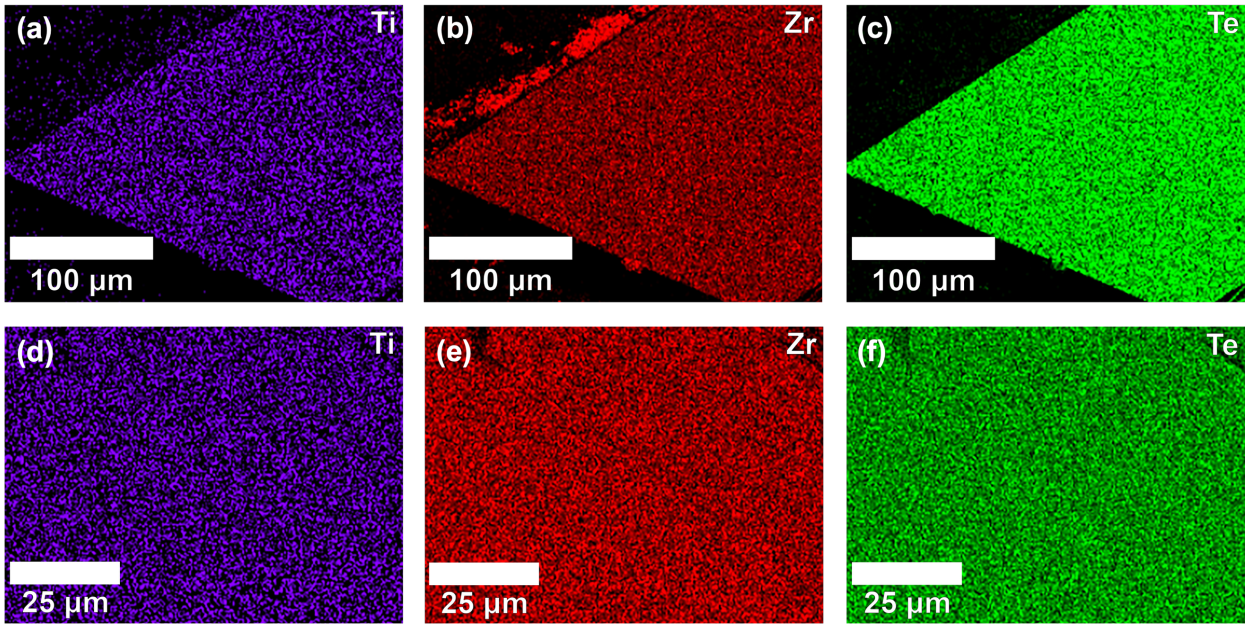

Figure S3.11 Elemental mapping illustrating homogeneous distribution of (a) and (d) Ti, (b) and (e) Zr, and (c) and (f) Te in $Ti_{0.02}Zr_{0.98}Te_3$ crystals.

References

1. Novoselov, K.; Geim, A.; Morozov, S.; Jiang, D.; Zhang, Y.; Dubonos, S.; Grigorieva, I.; Firsov, A. Electric Field Effect in Atomically Thin Carbon Films. *Science* **2004**, *306*, 666-669.

2. Choi, W.; Choudhary, N.; Han, G.; Park, J.; Akinwande, D.; Lee, Y. Recent Development of Two-Dimensional Transition Metal Dichalcogenides and Their Applications. *Mater. Tod.* **2017**, *20*, 116-130.

3. Manzeli, S.; Ovchinnikov, D.; Pasquier, D.; Yazyev, O.; Kis, A. 2D Transition Metal Dichalcogenides. *Nat. Rev. Mater.* **2017**, *2*, 17033.

4. Island, J.; Molina-Mendoza, A.; Barawi, M.; Biele, R.; Flores, E.; Clamagirand, J.; Ares, J.; Sánchez, C.; van der Zant, H.; D'Agosta, R.; Ferrer, I.; Castellanos-Gomez, A. Electronics and Optoelectronics of Quasi-1D Layered Transition Metal Trichalcogenides. *2D Mater.* **2017**, *4*, 022003.

5. Dai, J.; Li, M.; Zeng, X. Group IVB Transition Metal Trichalcogenides: A New Class of 2D Layered Materials Beyond Graphene. *WIREs Comput. Mol. Sci.* **2016**, *6*, 211-222.

6. Balandin, A.A.; Kargar, F.; Salguero, T.T.; Lake, R.K. One Dimensional van der Waals Quantum Materials. *Mater. Today* **2022**, *55*, 74-91.

7. Zhou, Y.; Wang, L.; Chen, S.; Qin, S.; Liu, X.; Chen, J.; Xue, D.; Luo, M.; Cao, Y.; Cheng, Y.; Sargent, E.; Tang, J. Thin-film Sb_2Se_3 Photovoltaics with Oriented One-Dimensional Ribbons and Benign Grain Boundaries. *Nat. Photonics* **2015**, *9*, 409-415.

8. Oh, S.; Chae, S.; Kim, B.; Choi, K.; Jang, W.; Jang, J.; Hussain, Y.; Lee, D.; Kim, Y.; Yu, H.; Choi, J. Synthesis of a One-Dimensional Atomic Crystal of Vanadium Selenide (V_2Se_9). *RSC Adv.* **2018**, *8*, 33980-33984.

9. Chen, X.; Shen, J.; Xu, Y.; Zhou, J.; Xu, Z. The Transport Properties of Nb-Doped Trichalcogenide $Ta_{0.8}Nb_{0.2}S_3$. *Phys. B: Condens. Matter* **2004**, *352*, 280-284.

10. Muratov, D.; Vanyushin, V.; Vorobeva, N.; Jukova, P.; Lipatov, A.; Kolesnikov, E.; Karpenkov, D.; Kuznetsov, D.; Sinitskii, A. Synthesis And Exfoliation Of Quasi-1D $(Zr,Ti)S_3$ Solid Solutions for Device Measurements. *J. Alloys Compd.* **2020**, *815*, 152316.

11. Flores, E.; Ares, J.; Sánchez, C.; Ferrer, I. Ternary Transition Titanium-Niobium Trisulfide as Photoanode for Assisted Water Splitting. *Catal. Today* **2019**, *321-322*, 107-112.

12. Yang, S.; Wu, M.; Shen, W.; Huang, L.; Tongay, S.; Wu, K.; Wei, B.; Qin, Y.; Wang, Z.; Jiang, C.; Hu, C. Highly Sensitive Polarization Photodetection Using a Pseudo-One-Dimensional $Nb_{(1-x)}Ti_xS_3$ Alloy. *ACS Appl. Mater. Interfaces* **2018**, *11*, 3342-3350.

13. Wu, K.; Blei, M.; Chen, B.; Liu, L.; Cai, H.; Brayfield, C.; Wright, D.; Zhuang, H.; Tongay, S. Phase Transition Across Anisotropic NbS_3 and Direct Gap Semiconductor TiS_3 at Nominal Titanium Alloying Limit. *Adv. Mater.* **2020**, *32*, 2000018.

14. Agarwal, A.; Qin, Y.; Chen, B.; Blei, M.; Wu, K.; Liu, L.; Shen, Y.; Wright, D.; Green, M.; Zhuang, H.; Tongay, S. Anomalous Isoelectronic Chalcogen Rejection in 2D Anisotropic vdW $TiS_{3(1-x)}Se_{3x}$ Trichalcogenides. *Nanoscale* **2018**, *10*, 15654-15660.

15. Stonemeyer, S.; Cain, J.; Oh, S.; Azizi, A.; Elasha, M.; Thiel, M.; Song, C.; Ercius, P.; Cohen, M.; Zettl, A. Stabilization of $NbTe_3$, VTe_3, and $TiTe_3$ via Nanotube Encapsulation. *J. Am. Chem. Soc.* **2021**, *143*, 4563-4568.

16. Li, J.; Peng, J.; Zhang, S.; Chen, G. Anisotropic Multichain Nature and Filamentary Superconductivity in the Charge Density Wave System $HfTe_3$. *Phys. Rev. B* **2017**, *96*, 174510.

17. Denholme, S.; Yukawa, A.; Tsumura, K.; Nagao, M.; Tamura, R.; Watauchi, S.; Tanaka, I.; Takayanagi, H.; Miyakawa, N. Coexistence of Superconductivity and Charge-Density Wave in the Quasi-One-Dimensional Material $HfTe_3$. *Sci. Rep.* **2017**, *7*, 45217.

18. Felser, C.; Finckh, E.; Kleinke, H.; Rocker, F.; Tremel, W. Electronic Properties of $ZrTe_3$. *J. Mater. Chem.* **1998**, *8*, 1787-1798.

19. Geremew, A.; Bloodgood, M.; Aytan, E.; Woo, B.; Corber, S.; Liu, G.; Bozhilov, K.; Salguero, T.; Rumyantsev, S.; Rao, M.; Balandin, A.A. Current Carrying Capacity of Quasi-1D $ZrTe_3$ van der Waals Nanoribbons. *IEEE Electron Device Lett.* **2018**, *39*, 735-738.

20. Geremew, A.; Rumyantsev, S.; Bloodgood, M.; Salguero, T.; Balandin, A. Unique Features of the Generation–Recombination Noise in Quasi-One-Dimensional van der Waals Nanoribbons. *Nanoscale* **2018**, *10*, 19749-19756.

21. Zhu, X.; Ning, W.; Li, L.; Ling, L.; Zhang, R.; Zhang, J.; Wang, K.; Liu, Y.; Pi, L.; Ma, Y.; Du, H.; Tian, M.; Sun, Y.; Petrovic, C.; Zhang, Y. Superconductivity and Charge Density Wave in $ZrTe_{3-x}Se_x$. *Sci. Rep.* **2016**, *6*, 26974.

22. Lei, H.; Zhu, X.; Petrovic, C. Raising T_c in Charge Density Wave Superconductor $ZrTe_3$ by Ni Intercalation. *Europhys. Lett.* **2011**, *95*, 17011.

23. Zhu, X.; Lei, H.; Petrovic, C. Coexistence of Bulk Superconductivity and Charge Density Wave in Cu_xZrTe_3. *Phys. Rev. Lett.* **2011**, *106,* 246404.

24. Tsuchiya, S.; Matsubayashi, K.; Yamaya, K.; Takayanagi, S.; Tanda, S.; Uwatoko, Y. Effects of Pressure and Magnetic Field on Superconductivity in $ZrTe_3$: Local Pair-Induced Superconductivity. *New J. Phys.* **2017**, *19*, 063004.

25. Yomo, R.; Yamaya, K.; Abliz, M.; Hedo, M.; Uwatoko, Y. Pressure Effect on Competition Between Charge Density Wave and Superconductivity in $ZrTe_3$: Appearance of Pressure-Induced Reentrant Superconductivity. *Phys. Rev. B* **2005**, *71*, 132508.

26. Liu, Y.; Hu, Z.; Tong, X.; Leshchev, D.; Zhu, X.; Lei, H.; Stavitski, E.; Attenkofer, K.; Petrovic, C. Thermal Transport and Mixed Valence in $ZrTe_3$ Doped with Hf and Se. *Appl. Phys. Lett.* **2022**, *120*, 022601.

27. Fjellvåg, H.; Furuseth, S.; Kjekshus, A.; Rakke, T. Low-Temperature Oxidative Degradation of Low-Dimensional Zirconium and Hafnium Tellurides. *Solid State Comm.* **1987**, *63*, 293-297.

28. Yamanaka, S.; Takatsuka, N.; Katsura, M.; Miyake, M. Study of the Zr-Te-O Ternary System. *J. Nucl. Mater.* **1989**, *161*, 210-215.

29. Kidd, T.; O'Shea, A.; Boyle, K.; Wallace, J.; Strauss, L. Synthesis of Freestanding HfO_2 Nanostructures. *Nanoscale Research Lett.* **2011**, *6*, 294.

30. Saibene, S.; Butz, T.; Lerf, A. Thermal Decomposition and Oxidation of $HfTe_5$ Single Crystals. *Ber. Bunsenges. Phys. Chem.* **1989**, *93*, 1359-1362.

31. de Boer, R.; Cordfunke, E.H.P. Reaction of Tellurium with Zircaloy-4. *J. Nucl. Mater.* **1995**, *223*, 103-108.

32. Örlygsson, G.; Harbrecht, B. The Crystal Structure of WC Type ZrTe. Advantages in Chemical Bonding as Contrasted to NiAs Type ZrTe. *Z. Naturforsch. B* **1999**, *54*, 1125-1128.

33. Sodeck, H.; Mikler, H.; Komarek, K. Transition Metal-Chalcogen Systems, VI: The Zirconium-Tellurium Phase Diagram. *Monatsh. Chem.* **1979**, *110*, 1-8.

34. Smeggil, J.; Bartram, S. The Preparation and X-Ray Characterization of $HfTe_{2-x}$, x = 0.061. *J. Solid State Chem.* **1972**, *5*, 391-394.

35. Harbrecht, B.; Conrad, M.; Degen, T.; Herbertz, R. Synthesis and Crystal Structure of Hf_2Te. *J. Alloys Compd.* **1997**, *255*, 178-182.

36. He, M.; Simon, A.; Duppel, V. Zr Stabilized Ti_5Te_4-Type Hafnium Telluride. *Z. Naturforsch. B* **2005**, *60b*, 284-288.

37. Furuseth, S.; Brattås, L.; Kjekshus, A.; Enzell, C.; Enzell, C.; Swahn, C. The Crystal Structure of $HfTe_5$. *Acta Chem. Scand.* **1973**, *27*, 2367-2374.

38. Abdon, R.; Hughbanks, T. Hf_3Te_2: A New and Remarkable Layered Compound. *Angew. Chem. Int. Ed. Engl.* **1994**, *33*, 2328-2330.

39. Hahn, H.; Ness, P. Über das System Zirkon/Tellur. *Z. fur Anorg. Allg. Chem.* **1959***, 302,* 136-154.

40. Sommers, J.; Palys, L.; Martin, N.; Fast, D.; Amiri, M.; Nyman, M. Oxo-Cluster-Based Zr/Hf^{IV} Separation: Shedding Light on a 70-Year-Old Process. *J. Am. Chem. Soc.* **2022**, *144*, 2816-2824.

41. Fahrenholtz, W.; Hilmas, G.; Talmy, I.; Zaykoski, J. Refractory Diborides of Zirconium and Hafnium. *J. Am. Ceram. Soc.* **2007**, *90*, 1347-1364.

42. Yu, X.; Wen, X.; Zhang, W.; Yang, L.; Wu, H.; Lou, X.; Xie, Z.; Liu, Y.; Chang, H. Fast and Controlled Growth of Two-dimensional Layered $ZrTe_3$ Nanoribbons by Chemical Vapor Deposition. *CrystEngComm* **2019**, *21*, 5586-5594.

43. Tan, R.; Azuma, Y.; Kojima, I. Comparative Study of the Interfacial Characteristics of Sputter-Deposited HfO_2 on Native SiO_2/Si (100) Using in situ XPS, AES and GIXR. *Surf. Interface Anal.* **2006**, *38*, 784-788.

44. Sygellou, L.; Gianneta, V.; Xanthopoulos, N.; Skarlatos, D.; Georga, S.; Krontiras, C.; Ladas, S.; Kennou, S. ZrO_2 and Al_2O_3 Thin Films on Ge (100) Grown By ALD: An XPS Investigation. *Surf. Sci. Spectra* **2011**, *18*, 58-67.

45. Yang, L.; Wu, H.; Zhang, W.; Chen, Z.; Li, J.; Lou, X.; Xie, Z.; Zhu, R.; Chang, H. Anomalous Oxidation and Its Effect on Electrical Transport Originating from Surface Chemical Instability in Large-Area, Few-Layer 1T′-$MoTe_2$ Films. *Nanoscale* **2018**, *10*, 19906-19915.

46. Toh, R.; Sofer, Z.; Pumera, M. Catalytic Properties of Group 4 Transition Metal Dichalcogenides (MX_2; M = Ti, Zr, Hf; X = S, Se, Te). *J. Mater. Chem. A* **2016**, *4*, 18322-18334.

47. Huang, J.; Hsu, H.; Wang, D.; Lin, W.; Cheng, C.; Lee, Y.; Hou, T. Polymorphism Control of Layered $MoTe_2$ through Two-Dimensional Solid-Phase Crystallization. *Sci. Rep.* **2019**, *9*, 8810.

48. Moulder, J. F.; Sticle, W. F.; Sobol, P. E.; Bomben, K. D. Handbook of X-ray Photoelectron Spectroscopy, Perkin-Elmer: **1993**.

CHAPTER 4

CHEMICAL VAPOR TRANSPORT GROWTH OF TRANSITION METAL DITELLURIDE AND DISELENIDE SOLID SOLUTIONS

Matthew D. Seivert and Tina T. Salguero. To be submitted to *Crystal Growth & Design*.

Abstract

We describe synthetic pathways leading to the isolation of single crystalline solid solutions of $Ti_xZr_{1-x}Te_2$ (x = 0.30, 0.50, 0.80), $Ti_xHf_{1-x}Te_2$ (x = 0.25, 0.40, 0.80), and $Ti_xZr_{1-x}Se_2$ (x = 0.25, 0.50, 0.75) via the chemical vapor transport (CVT) method. Solid solutions of $Ti_xZr_{1-x}Te_2$ and $Ti_xHf_{1-x}Te_2$ were isolated from temperatures ranging 875–825 °C via CVT by leveraging the chemistry of $TiTe_2$, $ZrTe_2$, and $HfTe_2$. Single crystal x-ray diffraction for $Ti_{0.50}Zr_{0.50}Te_2$ shows that this composition crystallizes in the trigonal space group $P\bar{3}m1$ with lattice parameters a = 3.84540(10) Å, c = 6.5519(2) Å, V = 83.904(5) Å^3, and Z = 1. Single crystal x-ray diffraction for $Ti_{0.25}Hf_{0.75}Te_2$ shows that this composition crystallizes in the trigonal space group $P\bar{3}m1$ with lattice parameters a = 3.89920(7) Å, c = 6.6108(2) Å, V = 87.043(4) Å^3, and Z = 1. For $Ti_xZr_{1-x}Se_2$ solid solutions, we found a temperature gradient of 900–870 °C under CVT conditions was ideal for crystal growth and phase isolation.

Introduction

The remarkable discovery of graphene in 2004 has attracted significant interest to the study of two-dimensional (2D) materials for electronics and optoelectronics applications.[1] Although graphene has exceptional properties, one of its greatest limitations is the absence of a bandgap, leading researchers to explore other 2D materials. Examples of 2D materials with promising properties include transition metal dichalcogenides (TMDs) (e.g. MoS_2, $ZrSe_2$, $TiTe_2$, etc.), hexagonal boron nitride (h-BN), black phosphorus, and "Xenes" (phosphorene, silicene, etc.).[2,3,4,5] Investigators have applied considerable focus on the transition metal dichalcogenides because of their variable compositions, ease of tunability, and unique properties.[6,7,8,9] The TMDs have an MX_2 composition where M is a transition metal and X is a chalcogen such as S, Se, or Te. The metal center is surrounded by six chalcogen atoms either in an octahedral or trigonal prismatic coordination and are covalently bonded together forming layers. Furthermore, these layers are held together via weak van der Waals interactions that make them easily exfoliated by either mechanical or chemical methods. Based on their underlying electronic structure, these materials can be classified as semiconducting, metallic, or semi-metallic. In addition, many of the TMDs have magnetic properties, charge density wave (CDW) properties, and can behave as superconductors.

Here, we focus on group IV transition metal ditelluride and diselenide solid solutions because there are indications that the modification of these materials can lead to tunable or novel electronic properties. Examples of TMD solid solutions previously reported that have demonstrated electronic property tunability (e.g. band gap engineering, increase in CDW potential, etc.) include $W_xMo_{1-x}S_2$, $W_xMo_{1-x}Se_2$, $W_{1-x}Nb_xS_2$, $Mo_xNb_{1-x}Se_2$, TaS_xSe_{2-x}, ZrS_xSe_{2-x}, HfS_xSe_{2-x}, and $ReS_{2-x}Se_x$.[10,11,12,13,14,15,16,17] Additional reports for group IV TMD solid solutions include $TiTe_{2-x}I_x$, $TiSe_xTe_{2-x}$, $HfS_{2-x}Te_x$, $Hf(Se_xTe_{1-x})_2$, $HfSe_{2-x}Te_x$, $Hf_xZr_{1-x}Te_2$, $ZrTe_{2(1-x)}Se_{2x}$, $Ti_xZr_{1-x}Te_2$,

$TiSe_{2-x}S_x$, and $Ti_xZr_{1-x}Se_2$.[18,19,20,21,22,23,24,25,26,27] In addition to alloying, researchers have also reported physical and chemical modifications such as pressure application and metal intercalation to modify various properties (e.g. electronic, magnetic, etc.) for many group IV TMDs.[24,28,29,30,31]

In this contribution, we consider the synthesis and crystal growth of solid solutions involving the analogs $TiTe_2$, $ZrTe_2$, and $HfTe_2$ using the chemical vapor transport (CVT) technique; more specifically, we target $Ti_xZr_{1-x}Te_2$ and $Ti_xHf_{1-x}Te_2$ across the compositional range $0 \leq x \leq 1$. Our experimental studies reported here briefly examine the favored synthetic conditions to isolate $TiTe_2$, $ZrTe_2$, and $HfTe_2$, and more significantly builds off of the chemistry of these materials to synthesize solid solutions of $Ti_xZr_{1-x}Te_2$ and $Ti_xHf_{1-x}Te_2$. EDS analysis for $Ti_xZr_{1-x}Te_2$ solid solutions confirms the isolated compositions are $Ti_{0.30}Zr_{0.70}Te_2$, $Ti_{0.50}Zr_{0.50}Te_2$, and $Ti_{0.80}Zr_{0.20}Te_2$. We also report the single crystal x-ray diffraction structure of $Ti_{0.50}Zr_{0.50}Te_2$ in which we note that both the *a* and *c* lattice parameters were between reported values for $TiTe_2$ and $ZrTe_2$. We also observe that the bond lengths of this structure are between reported values, but that the bond angles have slight deviations. For $Ti_xHf_{1-x}Te_2$ solid solutions, we observe that the isolated compositions are $Ti_{0.25}Hf_{0.75}Te_2$, $Ti_{0.40}Hf_{0.60}Te_2$, and $Ti_{0.80}Hf_{0.20}Te_2$ based on EDS analysis. Single crystal x-ray diffraction for $Ti_{0.25}Hf_{0.75}Te_2$ also shows that the *a* and *c* lattice parameters were between reported values for $TiTe_2$ and $HfTe_2$. Furthermore, we found that the bond lengths were slightly higher than its analogs, but, that the bond angles fell between reported values.

Finally, we consider preparation of $Ti_xZr_{1-x}Se_2$ single crystals. Our work was motivated by recent work by Mahapatra and coworkers in which they reported calculations indicating $Ti_{0.50}Zr_{0.50}Se_2$ may have exhibit CDW transitions.[32] Previous synthetic work regarding $Ti_xZr_{1-x}Se_2$ has included polycrystalline $Ti_{0.50}Zr_{0.50}Se_2$ reported by Cybulski, and single crystalline $Ti_{1-x}Zr_xSe_2$ ($x<0.21$) reported by Nieveen and coworkers and Freund and coworkers.[25,26,27] To further expand

previous experimental work, we isolated single crystals of $Ti_{1-x}Zr_xSe_2$ (x = 0.25, 0.50, 0.75) whose compositions we were able to confirm using EDS analysis.

Experimental

Materials: Zr foil (0.025 mm thickness, annealed, 99.8% metals basis excluding Hf) and Hf foil (0.25 mm thickness, annealed, 99.5% metals basis excluding Zr) were obtained from Alfa Aesar. Te powder (~200 mesh, 99.8% trace metals basis) and crystalline Ti (5-10 mm, ≥ 99.99% trace metals basis) were obtained from Sigma Aldrich. Se powder (~200 mesh, 99.99%) was obtained from Strem Chemicals. I_2 (crystals, 99.9% purity) was obtained from J.T. Baker Company. HNO_3 (15.8 M, Certified ACS Plus) was obtained from Fisher Chemical.

Ampule Preparation: Two sizes of fused quartz glass ampules were used in this work. "Solid state ampules": body dimensions of 90 mm length, 19 mm inner diameter, 22 mm outer diameter, volume ~33 cm^3; neck dimensions of 170 mm length, 7 mm inner diameter, 9.6 mm outer diameter. "CVT ampules": body dimensions of 175 mm length, 10 mm inner diameter, 14 mm outer diameter, volume ~13 cm^3; neck dimensions of 170 mm length, 7 mm inner diameter, 9.6 mm outer diameter. Ampules were cleaned by immersing in 15.8 M HNO_3 overnight. Afterwards, they were rinsed 3-5 times with deionized water, and then positioned in a horizontal tube furnace or box furnace and heated at 6 °C min^{-1} to a final temperature of 900 °C for 12 h followed by natural cooling to room temperature.

Crystal Growth of $TiTe_2$: 0.3168 g (6.618 mmol) Ti pieces were positioned at the bottom of a CVT quartz ampule with 1.6921 g (13.261 mmol) Te powder and I_2 crystals (~60 mg) while exposed to ambient atmosphere. The ampule was evacuated and backfilled with Ar three times using a Schlenk line manifold while submerged in an acetonitrile/dry ice bath before being flame

sealed under vacuum (~10^{-2} Torr). The evacuated ampule was positioned inside a preheated horizontal tube furnace at a final temperature gradient of 800–700 °C for 7 d followed by natural cooling to room temperature. The product was isolated as mm-sized, silver hexagonal plates (78.4 % isolated yield).

Crystal Growth of $ZrTe_2$: 0.5282 g (5.790 mmol) Zr foil was cut into mm-sized squares and positioned at the bottom of a CVT quartz ampule with 1.4763 g (11.569 mmol) Te powder and I_2 crystals (~60 mg) while exposed to ambient atmosphere. The ampule was evacuated and backfilled with Ar three times using a Schlenk line manifold while submerged in an acetonitrile/dry ice bath before being flame sealed under vacuum (~10^{-2} Torr). The evacuated ampule was positioned inside a preheated horizontal tube furnace at a final temperature gradient of 900–800 °C for 10 d followed by natural cooling to room temperature. The product was isolated as mm-sized, gold hexagonal plates (83.1 % isolated yield).

Crystal Growth of $HfTe_2$: 0.8282 g (4.640 mmol) Hf foil was cut into mm-sized squares and positioned at the bottom of a CVT quartz ampule with 1.1896 g (9.3229 mmol) Te powder and I_2 crystals (~60 mg) while exposed to ambient atmosphere. The ampule was evacuated and backfilled with Ar three times using a Schlenk line manifold while submerged in an acetonitrile/dry ice bath before being flame sealed under vacuum (~10^{-2} Torr). The evacuated ampule was positioned inside a horizontal tube furnace and heated at 3 °C min^{-1} to a final temperature gradient of 900–800 °C for 10 d followed by natural cooling to room temperature. The product was isolated as mm-sized, gold hexagonal plates (28.7 % isolated yield).

Crystal Growth of $Ti_xZr_{1-x}Te_2$: for $Ti_{0.25}Zr_{0.75}Te_2$, 0.0801 g (1.67 mmol) Ti pieces and 0.4547 g (4.985 mmol) Zr foil (cut into mm-sized squares) were positioned at the bottom of a CVT

quartz ampule with 1.6860 g (13.213 mmol) Te powder and I_2 crystals (~60 mg) while exposed to ambient atmosphere.

For $Ti_{0.50}Zr_{0.50}Te_2$, 0.1595 g (3.332 mmol) Ti pieces and 0.3022 g (3.313 mmol) Zr foil (cut into mm-sized squares) were positioned at the bottom of a CVT quartz ampule with 1.6875 g (13.225 mmol) Te powder and I_2 crystals (~60 mg) while exposed to ambient atmosphere.

For $Ti_{0.75}Zr_{0.25}Te_2$, 0.2393 g (4.999 mmol) Ti pieces and 0.1539 g (1.687 mmol) Zr foil (cut into mm-sized squares) were positioned at the bottom of a CVT quartz ampule with 1.6909 g (13.252 mmol) Te powder and I_2 crystals (~60 mg) while exposed to ambient atmosphere.

All of the ampules were evacuated and backfilled with Ar three times using a Schlenk line manifold while submerged in an acetonitrile/dry ice bath before being flame sealed under vacuum (~10^{-2} Torr). The evacuated ampules were then positioned inside a preheated horizontal tube furnace to final temperature gradients (875–775 °C for $Ti_{0.30}Zr_{0.70}Te_2$; 850–750 °C for $Ti_{0.50}Zr_{0.50}Te_2$; 825–725 °C for $Ti_{0.80}Zr_{0.20}Te_2$) based on the target compositions of the materials for 10 d followed by natural cooling to room temperature. These syntheses resulted in mm-sized silver hexagonal plates. The isolated yields for the products $Ti_{0.30}Zr_{0.70}Te_2$, $Ti_{0.50}Zr_{0.50}Te_2$, and $Ti_{0.80}Zr_{0.20}Te_2$ were 78.5 %, 82.6 %, and 85.2 % respectively.

Crystal Growth of $Ti_xHf_{1-x}Te_2$: for $Ti_{0.25}Hf_{0.75}Te_2$, 0.0564 g (1.18 mmol) Ti pieces and 0.6202 g (3.475 mmol) Hf foil (cut into mm-sized squares) were positioned at the bottom of a CVT quartz ampule with 1.1860 g (9.2947 mmol) Te powder and I_2 crystals (~60 mg) while exposed to ambient atmosphere.

For $Ti_{0.50}Hf_{0.50}Te_2$, 0.1107 g (2.313 mmol) Ti pieces and 0.4118 g (2.307 mmol) Hf foil (cut into mm-sized squares) were positioned at the bottom of a CVT quartz ampule with 1.1850 g (9.2868 mmol) Te powder and I_2 crystals (~60 mg) while exposed to ambient atmosphere.

For $Ti_{0.75}Hf_{0.25}Te_2$, 0.1687 g (3.524 mmol) Ti pieces and 0.2067 g (1.158 mmol) Hf foil (cut into mm-sized squares) were positioned at the bottom of a CVT quartz ampule with 1.1873 g (9.3049 mmol) Te powder and I_2 crystals (~60 mg) while exposed to ambient atmosphere.

All of the ampules were evacuated and backfilled with Ar three times using a Schlenk line manifold while submerged in an acetonitrile/dry ice bath before being flame sealed under vacuum (~10^{-2} Torr). The evacuated ampules were then positioned inside a preheated horizontal tube furnace to final temperature gradients (875–775 °C for $Ti_{0.25}Hf_{0.75}Te_2$; 850–750 °C for $Ti_{0.40}Hf_{0.60}Te_2$; 825–725 °C for $Ti_{0.80}Hf_{0.20}Te_2$) based on the target compositions of the materials for 10 d followed by natural cooling to room temperature. These syntheses resulted in mm-sized silver hexagonal plates. The isolated yields for the products $Ti_{0.25}Hf_{0.75}Te_2$, $Ti_{0.40}Hf_{0.60}Te_2$, and $Ti_{0.80}Hf_{0.20}Te_2$ were 88.8 %, 86.0 %, and 78.4 % respectively.

Solid State Synthesis of $ZrSe_2$: 1.1001 g (12.060 mmol) Zr foil were cut into mm-sized squares and positioned at the bottom of a solid state quartz ampule, in addition to 1.9196 g (24.308 mmol) Se powder while exposed to ambient atmosphere. The ampule was evacuated and backfilled with Ar three times using a Schlenk line manifold before being flame sealed under vacuum (~10^{-2} Torr). The evacuated ampule was then positioned inside a preheated horizontal tube furnace to a final temperature of 800 °C for 72 h, followed by natural cooling to room temperature. The product was isolated as cm-sized, grey/black flakes (94.7 % isolated yield).

Solid State Synthesis of $TiSe_2$: 0.7006 g (14.64 mmol) Ti pieces were positioned at the bottom of a solid state quartz ampule in addition to 2.3040 g (29.176 mmol) Se powder while exposed to ambient atmosphere. The ampule was evacuated and backfilled with Ar three times using a Schlenk line manifold before being flame sealed under vacuum (~10^{-2} Torr). The evacuated ampule was then positioned inside a preheated horizontal tube furnace to a final temperature of

800 °C for 72 h, followed by natural cooling to room temperature. The product was isolated as cm-sized, maroon/burgundy flakes (92.0 % isolated yield).

Crystal Growth of $Ti_xZr_{1-x}Se_2$: for $Ti_{0.50}Zr_{0.50}Se_2$, two approaches were taken: with elemental precursors (Ti, Zr, and Se), and with polycrystalline precursors ($TiSe_2$ and $ZrSe_2$).

For the synthesis with elemental precursors, 0.1188 g (2.482 mmol) Ti pieces and 0.2230 g (2.445 mmol) Zr foil (cut into mm-sized squares) were positioned at the bottom of a CVT quartz ampule with 0.7720 g (9.776 mmol) Se powder and I_2 crystals (~60 mg) while exposed to ambient atmosphere.

For the synthesis with polycrystalline precursors, 0.8290 g (4.028 mmol) as-prepared $TiSe_2$ and 1.0052 g (4.0344 mmol) as-prepared $ZrSe_2$ (solid state routes) were lightly ground into fine powders using an agate mortar and pestle inside an Ar glovebox. The ground $TiSe_2$/ $ZrSe_2$ mixtures were transferred to the bottom of a CVT quartz ampule with iodine crystals (~60 mg) while inside an Ar glovebox.

For $Ti_{0.75}Zr_{0.25}Se_2$, 0.1749 g (3.654 mmol) Ti pieces and 0.1116 g (1.223 mmol) Zr foil (cut into mm-sized squares) were positioned at the bottom of a solid state quartz ampule with 0.7690 g (9.738 mmol) Se powder and I_2 crystals (~60 mg) while exposed to ambient atmosphere.

For $Ti_{0.25}Zr_{0.75}Se_2$, 0.0584 g (1.22 mmol) Ti pieces and 0.3339 g (3.660 mmol) Zr foil (cut into mm-sized squares) were positioned at the bottom of a solid state quartz ampule with 0.7688 g (9.735 mmol) Se powder and I_2 crystals (~60 mg) while exposed to ambient atmosphere.

All of the ampules were evacuated and backfilled with Ar three times using a Schlenk line manifold while submerged in an acetonitrile/dry ice bath before being flame sealed under vacuum (~10^{-2} Torr). The evacuated ampules were then positioned inside a preheated horizontal tube

furnace to a final temperature gradient of 900–870 °C for 7-10 d followed by natural cooling to room temperature. These syntheses resulted in mm-sized gold hexagonal plates.

Characterization: Powder X-ray diffraction (PXRD) data were collected on a Bruker D8 Advance instrument utilizing a Co−Kα X-ray source (λ = 1.78890 Å) operated at 35 kV and 40 mA. Data was collected from 10 to 80° 2θ with a scan rate of 0.1 s/step. Samples were prepared as powder mounts.

Scanning electron microscopy (SEM) analysis was performed using a FEI Teneo FE-SEM at 10 keV with a spot size of 13. Energy dispersive x-ray spectroscopy (EDS) was performed using an integrated Aztec Oxford Instruments X-MAX^N detector operated at 10 keV with a spot size of 13. Samples were mounted onto a stub with carbon tape and exfoliated using scotch tape. Experimental compositions of $Ti_xZr_{1-x}Te_2$, $Ti_xHf_{1-x}Te_2$, and $Ti_xZr_{1-x}Se_2$ were determined using average atomic percentages collected via EDS and calculated by normalizing the chalcogen percentage.

For the single crystal X-ray diffraction study on $Ti_{0.50}Zr_{0.50}Te_2$, a silver crystal (with approximate dimensions 0.030 mm × 0.070 mm × 0.140 mm) was mounted on the tip of a glass fiber. The X-ray intensity data were measured at room temperature on a Bruker D8 Quest PHOTON 100 CMOS X-ray diffractometer system with Incoatec Microfocus Source (IμS) monochromated Mo Kα radiation (λ = 0.71073 Å, sealed tube) using phi and omega-scan technique. Additional details are provided in the Supporting Information.

For the single crystal X-ray diffraction study on $Ti_{0.20}Hf_{0.80}Te_2$, a dark silver crystal (with approximate dimensions 0.010 mm × 0.050 mm × 0.160 mm) was mounted on the tip of a glass fiber. The X-ray intensity data were measured at room temperature on a Bruker D8 Quest PHOTON 100 CMOS X-ray diffractometer system with Incoatec Microfocus Source (IμS)

monochromated Mo Kα radiation (λ = 0.71073 Å, sealed tube) using phi and omega-scan technique. The data were collected in 1012 frames with 10 second exposure times. Additional details are provided in the Supporting Information.

Results and Discussion

The solid state approach was used to synthesize polycrystalline $TiSe_2$ and $ZrSe_2$ which were subsequently used under CVT conditions. Single crystals of $TiTe_2$, $ZrTe_2$, $HfTe_2$, $Ti_xZr_{1-x}Te_2$, $Ti_xHf_{1-x}Te_2$, and $Ti_xZr_{1-x}Se_2$ were synthesized using the CVT approach.

CVT growth of $TiTe_2$, $ZrTe_2$, and $HfTe_2$ crystals: For single crystalline $TiTe_2$, we determined that single crystals could be isolated reproducibly using a conventional CVT approach using a 800–700 °C gradient and I_2 transport. SEM imaging (Figure 4.1a) showed that mm-sized crystals with a hexagonal plate like morphology and well defined edges were isolated. Using EDS analysis, we compared the average atomic percentages of synthesized crystals (Ti: 33.4 %, Te: 66.6 %) versus theoretical percentages (Ti: 33.3 %, Te: 66.7 %) to confirm the $TiTe_2$ composition. Previous studies implementing the CVT approach reported the isolation of single crystals using temperature gradients ranging from 900–800 °C, 800–700 °C, and 750–690 °C, primarily using I_2 as a transport agent.[18,28,33,34,35] In the duration of this study, we attempted multiple CVT syntheses at all of the reported temperature gradients listed above for 7-10 days using multiple transport agents including I_2, NH_4Cl, and 10% excess Te chalcogen. Though these approaches led to crystalline $TiTe_2$ phases, we found these crystals were not of adequate size, or did not result in well-defined morphologies.

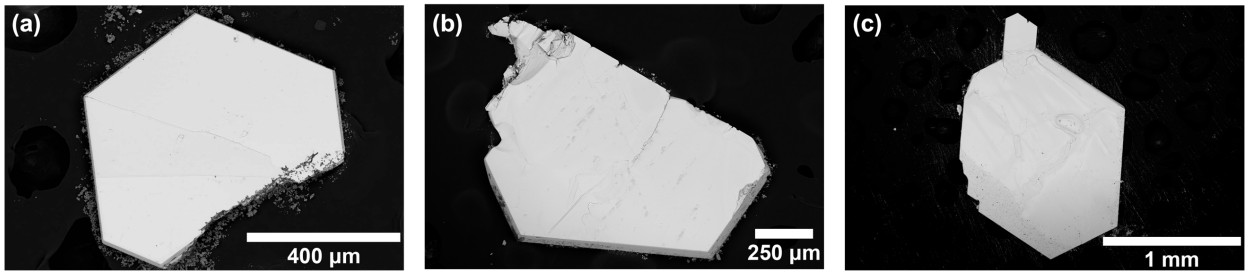

Figure 4.1 SEM imaging of (a) $TiTe_2$ (b) $ZrTe_2$ and (c) $HfTe_2$ single crystals.

For single crystalline $ZrTe_2$, we were able to readily synthesize gold, mm-sized crystals via the CVT approach at 900–800 °C using I_2 transport. SEM analysis is shown in Figure 4.1b illustrating the hexagonal plate morphology of the synthesized crystals. Using EDS analysis, we compared the average atomic percentages of synthesized crystals (Zr: 33.9 %, Te: 66.1 %) versus theoretical percentages (Zr: 33.3 %, Te: 66.7 %) confirming the $ZrTe_2$ phase. Previous reports for $ZrTe_2$ indicated varying temperature gradients via CVT including 900–800 °C**,** 880–780 °C, 850–800 °C, and 800–700 °C.[36,37,38,39] Although different temperature gradients had been reported, we were aware of the neighboring $ZrTe_3$ phase and its favored temperature gradient from 850–750 °C using I_2 transport.[40,41] As is common with neighboring dichalcogenide and trichalcogenides materials, it is usual for the dichalcogenide phase to be favored at higher temperatures than the corresponding trichalcogenide phase. Therefore, we predicted the optimized temperature for $ZrTe_2$ had to surpass the 850–750 °C gradient.

For single crystalline $HfTe_2$, we isolated mm-sized, gold hexagonal plates using a temperature gradient from 900–800 °C under CVT conditions. SEM analysis is shown in Figure 4.1c, illustrating the hexagonal plate morphology of the synthesized crystals. Using EDS analysis, we compared the average atomic percentages of synthesized crystals (Hf: 35.8 %, Te: 64.2 %) versus theoretical percentages (Hf: 33.3 %, Te: 66.7 %) confirming the $HfTe_2$ composition. We

note that the atomic percentage for Te in $HfTe_2$ was slightly lower than expected potentially due to Te vacancies in the crystalline lattice. Previous studies using the CVT approach reported the isolation of single crystals using temperature gradients ranging from 1025–850 °C, 900–750 °C, 750–650 °C, 700–600 °C, and 600–500 °C using transport agents such as I_2, NH_4I, and CBr_4.[20,30,42,43,44,45] In our work with the neighboring $HfTe_3$ phase, we found that $HfTe_2$ was readily accessible at temperatures above 530 °C, and more specifically, we determined crystal growth was optimized at 900 °C.

CVT growth of $Ti_xZr_{1-x}Te_2$ crystals: for the isolation of single crystal solid solutions of $Ti_xZr_{1-x}Te_2$ (where x = 0.25, 0.50, and 0.75 were target compositions) we found temperature to be one of the most important factors. We considered the favored temperatures of $TiTe_2$ and $ZrTe_2$ based on previous studies, in addition to other factors such as temperature gradient and transport agent. More specifically, we leveraged the favored temperature gradient of $TiTe_2$ from 800–700 °C and the favored temperature gradient of $ZrTe_2$ from 900–800 °C. As a result, we hypothesized that each solid solution of $Ti_xZr_{1-x}Te_2$ would be favored at a different temperature gradient based on its composition assuming a linear relationship between the ideal temperature gradients of $TiTe_2$ and $ZrTe_2$: 875–775 °C for $Ti_{0.25}Zr_{0.75}Te_2$; 850–750 °C for $Ti_{0.50}Zr_{0.50}Te_2$; and 825–725 °C for $Ti_{0.75}Zr_{0.25}Te_2$.

Each CVT synthesis for $Ti_xZr_{1-x}Te_2$ resulted in silver hexagonal plates that were collected after 10 days of heating. SEM analysis indicated the crystals were mm-sized and also had a "sheet-like" layered morphology (Figure 4.2) which resembled that of the corresponding $TiTe_2$ and $ZrTe_2$ analogs. In addition to SEM, EDS analysis was implemented to determine the compositions of the different solid solutions. In Table 4.1, the average atomic percentages of Ti, Zr, and Te for the three different target compositions are listed, in addition to the corresponding experimental

compositions. Furthermore, we implemented elemental mapping (Figure S4.2) and noted homogeneous distribution of Ti, Zr, and Te throughout.

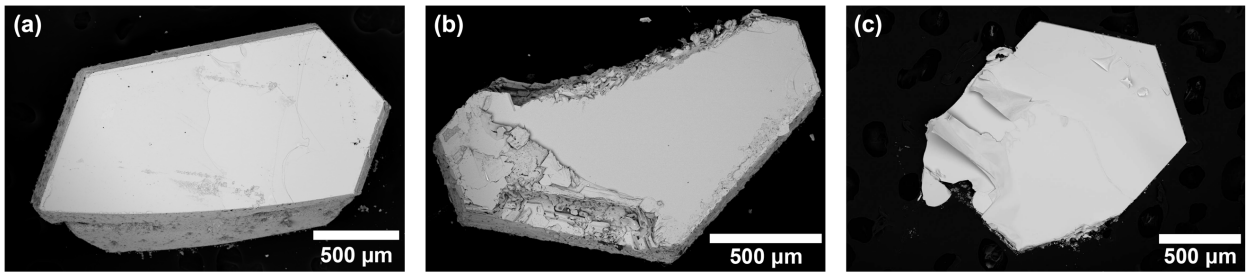

Figure 4.2 SEM imaging of (a) $Ti_{0.30}Zr_{0.70}Te_2$ (b) $Ti_{0.50}Zr_{0.50}Te_2$ and (c) $Ti_{0.80}Zr_{0.20}Te_2$ single crystals.

Table 4.1 Summary of $Ti_xZr_{1-x}Te_2$ compositions determined using EDS analysis.

Target Composition	Atomic % by EDS			Experimental Result
	Ti	Zr	Te	
$Ti_{0.25}Zr_{0.75}Te_2$	10.7	23.5	65.8	$Ti_{0.30}Zr_{0.70}Te_2$
$Ti_{0.50}Zr_{0.50}Te_2$	17.6	16.5	65.9	$Ti_{0.50}Zr_{0.50}Te_2$
$Ti_{0.75}Zr_{0.25}Te_2$	27.6	5.8	66.6	$Ti_{0.80}Zr_{0.20}Te_2$

We also considered the potential presence of neighboring phases. As previously mentioned, we determined $ZrTe_2$ was favored at a temperature gradient of 900–800 °C, but, the neighboring $ZrTe_3$ phase is favored at 850–750 °C.[40,41] For $TiTe_2$, competition with neighboring phases was not a concern. In addition, bulk $TiTe_3$ has yet to be reported, although, a recent report by Zettl and coworkers described the growth of $TiTe_3$ chains within multiwalled carbon nanotubes.[46]

Advantageously, $Ti_xZr_{1-x}Te_3$ crystals were not present in our samples, which was likely due to the incorporation of Ti stabilizing the ditelluride phase.

Single crystals of $Ti_{0.50}Zr_{0.50}Te_2$ were used to collect high quality x-ray diffraction data. In Table 4.2, we report the lattice parameters for $Ti_{0.50}Zr_{0.50}Te_2$, $TiTe_2$, and $ZrTe_2$. Overall, the lattice parameters of these compositions were within approximately 3% of each other confirming their isostructural nature. We also found $Ti_{0.50}Zr_{0.50}Te_2$ crystallizes in the hexagonal $P\bar{3}m1$ space group shared with $TiTe_2$ and $ZrTe_2$. Finally, we note expansion of the unit cell volume from $TiTe_2$ to $Ti_{0.50}Zr_{0.50}Te_2$ to $ZrTe_2$ due to increased Zr incorporation and its larger atomic radii.

Table 4.2 Summary of crystallographic data for $TiTe_2$, $Ti_{0.50}Zr_{0.50}Te_2$, and $ZrTe_2$.

Formula	**$TiTe_2$**	**$Ti_{0.50}Zr_{0.50}Te_2$**	**$ZrTe_2$**
F.W. (g/mol)	303.07	324.75	346.42
Crystal system	Trigonal	Trigonal	Trigonal
Space group	$P\bar{3}m1$	$P\bar{3}m1$	$P\bar{3}m1$
Z	1	1	1
a (Å)	3.777(3)	3.84540(10)	3.9563
b (Å)	3.777(3)	3.84540(10)	3.9563
c (Å)	6.498(6)	6.5519(2)	6.6566
α (°)	90	90	90
β (°)	90	90	90
γ (°)	120	120	120
V (Å^3)	80.28	83.904(5)	90.232
Absorption coefficient (mm^{-1})	-	19.648	-
Θ range (°)	6.257-52.118	3.109-59.752	-
hkl ranges	-	$-9 \leq h \leq 9$ $-9 \leq k \leq 8$ $-15 \leq l \leq 15$	-
No. reflections; $R_{int.}$	-	533; 0.0620	-
No. parameters	-	10	-
R_1; wR_2	0.035; -	0.0279; 0.0930	-
Goodness of fit	-	1.096	-
Diffraction peak; hole (e$^-$; Å^3)	-	4.686; -2.167	-
Temperature (K)	-	288(2)	-
Reference	35	This work	37

We also report the bond lengths and bond angles of $Ti_{0.50}Zr_{0.50}Te_2$ versus $TiTe_2$ and $ZrTe_2$ in Tables S4.1 and S4.2. Comparison was made where the view of the metal center is coordination to six Te atoms (Figure S4.1). Ti/Zr—Te bond lengths were within ranges for $TiTe_2$ and $ZrTe_2$. Furthermore, a comparison of varying Te—Ti/Zr—Te bond angles was made where we found the angles slightly deviated, either being slightly lower or higher than the reported analogs. The structure of $Ti_{0.50}Zr_{0.50}Te_2$ is illustrated in Figure 4.3 from the a and c axes in which the octahedral coordination of the metal centers and the van der Waals gap are readily apparent. Data tables for atomic coordinates and anisotropic displacement parameters are reported in Tables S4.3 and S4.4.

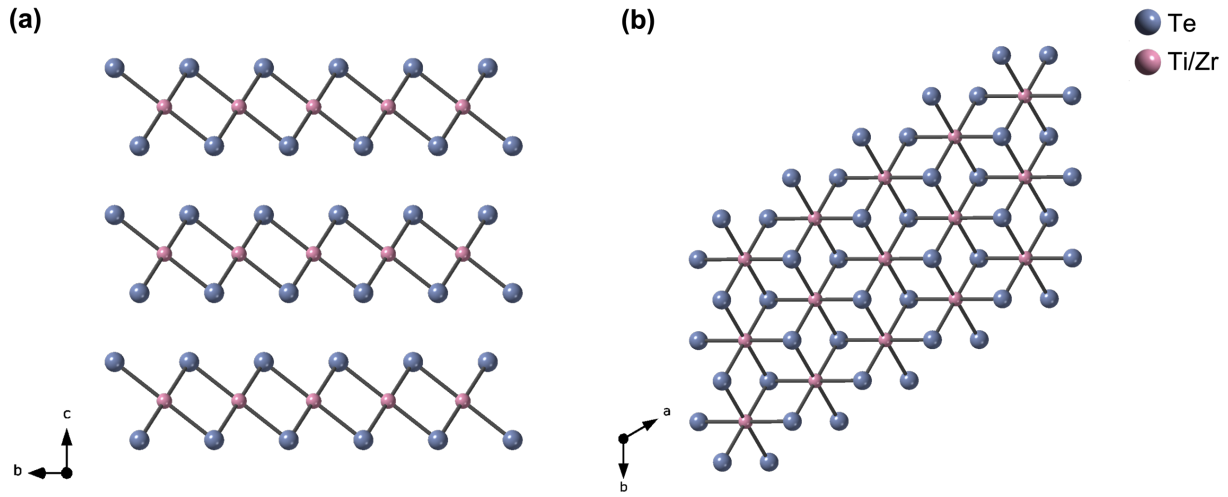

Figure 4.3 Crystal structure of $Ti_{0.50}Zr_{0.50}Te_2$ along the (a) *a* and (b) *c* axes.

CVT growth of $Ti_xHf_{1-x}Te_2$ crystals: for this portion of our study, we continued to prioritize temperature as the most important factor in isolating single crystal solid solutions of $Ti_xHf_{1-x}Te_2$ (where x = 0.25, 0.50, and 0.75 were target compositions). Like the case with $Ti_xZr_{1-x}Te_2$, we leveraged the favored temperature gradients of both $TiTe_2$ and $HfTe_2$ for $Ti_xHf_{1-x}Te_2$. We considered the favored temperature gradient of $TiTe_2$ from 800–700 °C and the favored temperature gradient of $HfTe_2$ from 900–800 °C. As a result, we hypothesized that each solid solution of $Ti_xHf_{1-x}Te_2$ would be favored at a different temperature gradient based on its composition: 875–775 °C for $Ti_{0.25}Hf_{0.75}Te_2$; 850–750 °C for $Ti_{0.50}Hf_{0.50}Te_2$; and 825–725 °C for $Ti_{0.75}Hf_{0.25}Te_2$.

As a result, we found each CVT synthesis resulted in silver hexagonal plates after 10 days of heating. Using SEM, we determined that the crystals were mm-sized and had the expected "sheet-like" layered morphology (Figure 4.4) seen in $TiTe_2$ and $HfTe_2$. Analysis using EDS provided further quantification of the exact compositions isolated. In Table 4.3, the average atomic percentages of Ti, Zr, and Te for the three different target compositions are listed, in addition to

the corresponding experimental compositions. Furthermore, we conducted elemental mapping (Figure S4.6) and noted homogeneous distribution of Ti, Hf, and Te throughout.

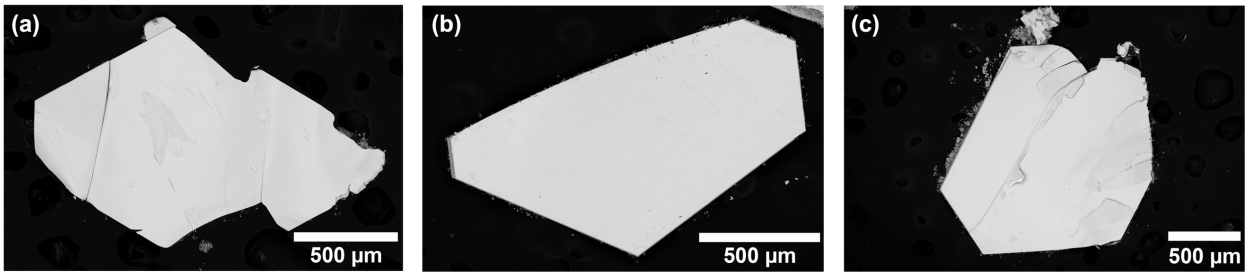

Figure 4.4 SEM imaging of (a) $Ti_{0.25}Hf_{0.75}Te_2$ (b) $Ti_{0.40}Hf_{0.60}Te_2$ and (c) $Ti_{0.80}Hf_{0.20}Te_2$ single crystals.

Table 4.3 Summary of $Ti_xHf_{1-x}Te_2$ compositions determined using EDS analysis.

Target Composition	**Atomic % by EDS**			**Experimental Result**
	Ti	**Hf**	**Te**	
$Ti_{0.25}Hf_{0.75}Te_2$	8.9	25.6	65.5	$Ti_{0.25}Hf_{0.75}Te_2$
$Ti_{0.50}Hf_{0.50}Te_2$	15.2	18.8	66.0	$Ti_{0.40}Hf_{0.60}Te_2$
$Ti_{0.75}Hf_{0.25}Te_2$	29.0	4.8	66.2	$Ti_{0.80}Hf_{0.20}Te_2$

When considering neighboring phases, there was less concern for $Ti_xHf_{1-x}Te_2$ solid solutions versus our work with $Ti_xZr_{1-x}Te_2$. As previously mentioned, there are no polycrystalline or single crystalline neighboring phases of $TiTe_2$, and the two neighboring phases of $HfTe_2$ ($HfTe_3$ and $HfTe_5$) are thermodynamically favored at significantly lower temperatures.

Single crystals of $Ti_{0.25}Hf_{0.75}Te_2$ were used to collect high quality x-ray diffraction data. In Table 4.4, we report the lattice parameters for $Ti_{0.25}Hf_{0.75}Te_2$, $TiTe_2$, and $HfTe_2$. Overall, the lattice parameters of these compositions fall within approximately 3% of each other, confirming their

isostructural nature. Similar to its analogs, $Ti_{0.25}Hf_{0.75}Te_2$ crystallizes in the hexagonal $P\bar{3}m1$ space group shared with $TiTe_2$ and $HfTe_2$. We also note expansion of the unit cell volume from $TiTe_2$ to $Ti_{0.25}Hf_{0.75}Te_2$ to $HfTe_2$ with increased Hf incorporation and its larger atomic radii.

Table 4.4 Summary of crystallographic data for $TiTe_2$, $Ti_{0.25}Hf_{0.75}Te_2$, and $HfTe_2$.

Formula	**$TiTe_2$**	**$Ti_{0.25}Hf_{0.75}Te_2$**	**$HfTe_2$**
F.W. (g/mol)	303.07	401.04	433.69
Crystal system	Trigonal	Trigonal	Trigonal
Space group	$P\bar{3}m1$	$P\bar{3}m1$	$P\bar{3}m1$
Z	1	1	1
a (Å)	3.777(3)	3.89920(7)	3.951(8)
b (Å)	3.777(3)	3.89920(7)	3.951(8)
c (Å)	6.498(6)	6.6108(2)	6.658(8)
α (°)	90	90	90
β (°)	90	90	90
γ (°)	120	120	120
V (Å^3)	80.28	87.043(4)	90.01
Absorption coefficient (mm^{-1})	-	39.216	-
Θ range (°)	6.257-52.118	3.081-29.963	6.107-52.760
hkl ranges	-	$-5 \leq h \leq 5$ $-5 \leq k \leq 5$ $-9 \leq l \leq 9$	-
No. reflections; $R_{int.}$	-	127; 0.0616	-
No. parameters	-	10	-
R_1; wR_2	0.035; -	0.0466; 0.1498	-
Goodness of fit	-	1.013	-
Diffraction peak; hole (e$^-$; Å^3)	-	3.793; -4.191	-
Temperature (K)	-	297(2)	-
Reference	35	This work	20

We also report the bond lengths and bond angles of $Ti_{0.25}Hf_{0.75}Te_2$ versus $TiTe_2$ and $HfTe_2$ in Tables S4.5 and S4.6. Comparison was made where the view of the metal center is coordination to six Te atoms (Figure S4.4). Ti/Hf—Te bond lengths were slightly higher than values previously reported for $TiTe_2$ and $HfTe_2$. Furthermore, a comparison of varying Te—Ti/Hf—Te bond angles

were between expected values for both $TiTe_2$ and $HfTe_2$. The structure of $Ti_{0.25}Hf_{0.75}Te_2$ is illustrated in Figure 4.5 from the *a* and *c* axes in which the octahedral coordination of the metal centers and the van der Waals gap are readily apparent. Data tables for atomic coordinates and anisotropic displacement parameters are reported in Tables S4.7 and S4.8.

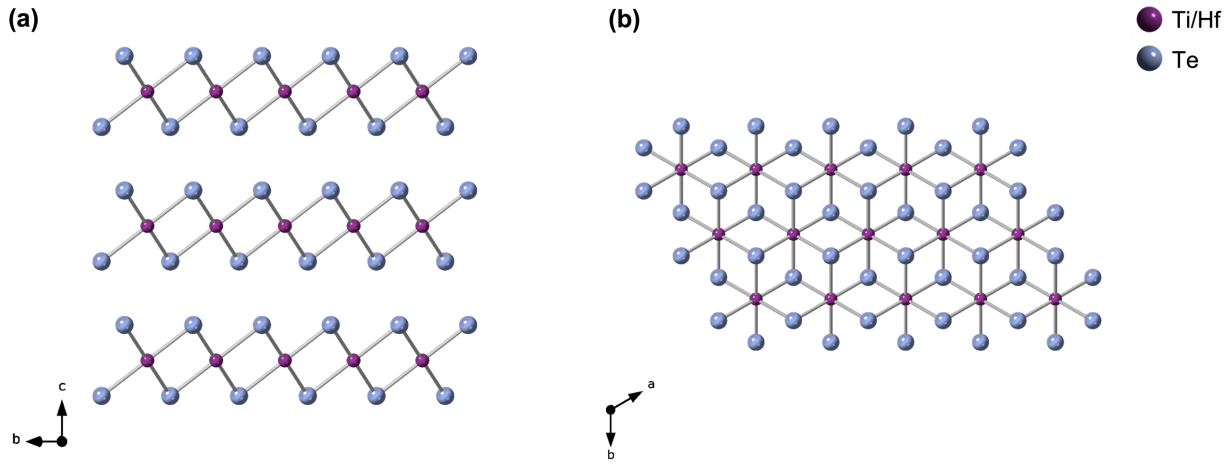

Figure 4.5 Crystal structure of $Ti_{0.25}Hf_{0.75}Te_2$ along the (a) *a* and (b) *c* axes.

CVT growth of $Ti_xZr_{1-x}Se_2$ crystals: We determined single crystals of $Ti_xZr_{1-x}Se_2$ (x = 0.25, 0.50, and 0.75) were accessible under CVT conditions using elemental precursors. We considered previous work reported for polycrystalline $Ti_{0.50}Zr_{0.50}Se_2$ grown at 900 °C and single crystalline $Ti_{1-x}Zr_xSe_2$ (x < 0.21) grown at 600 °C.[25,26,27]

For $Ti_{0.50}Zr_{0.50}Se_2$, we collected gold, mm-sized hexagonal plates at 900 °C using a 30 °C gradient (Figure 4.6a). EDS analysis confirmed the composition of the resulting crystals were consistently $Ti_{0.50}Zr_{0.50}Se_2$ (Table S4.9).

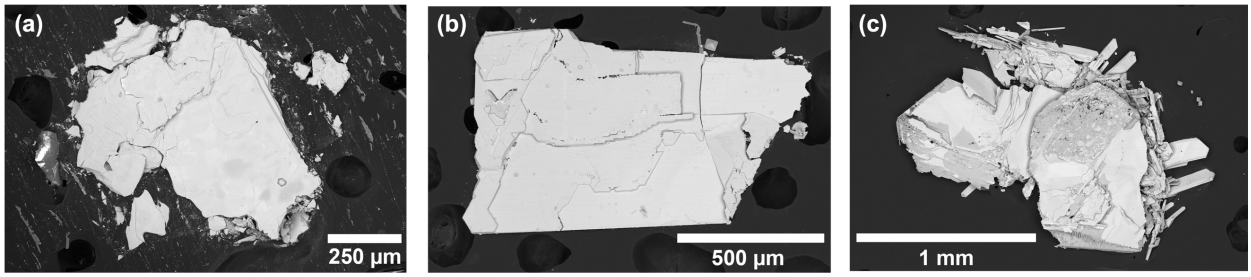

Figure 4.6 SEM imaging of (a) $Ti_{0.50}Zr_{0.50}Se_2$ (b) $Ti_{0.75}Zr_{0.25}Se_2$ and (c) $Ti_{0.25}Zr_{0.75}Se_2$ single crystals.

We also attempted synthesis of $Ti_{0.50}Zr_{0.50}Se_2$ under identical synthetic conditions using polycrystalline $TiSe_2$ and $ZrSe_2$ ground together vs elemental precursors. As a result, we found that crystal growth of gold hexagonal plates (Figure S4.7a) and composition (Table S4.9) were nearly identical. We note there was negligible change in composition with starting materials, and we found that temperature and gradient were important factors. When attempting the synthesis of $Ti_{0.50}Zr_{0.50}Se_2$ at 900 °C using a 100 °C gradient, we isolated gold hexagonal plates (Figure S4.7b and Figure S4.7c) that EDS analysis showed were varying phases including $Ti_{0.70}Zr_{0.30}Se_2$ and $Ti_{0.60}Zr_{0.40}Se_2$ (Table S4.9). Based on these results, we found minimizing the gradient from 100 °C to 30 °C was critical for singular phase isolation.

Furthermore, we also attempted syntheses at 975 °C and 600 °C using a 100 °C gradient. At 975 °C, mm-sized gold hexagonal plates (Figure S4.7d, Figure S4.7e, and Figure S4.8f) were collected, but multiple phases were present including $Ti_{0.80}Zr_{0.20}Se_2$, $Ti_{0.70}Zr_{0.30}Se_2$, and $Ti_{0.60}Zr_{0.40}Se_2$ based on EDS analysis (Table S4.9). At 600 °C, we isolated gold plates with irregular morphologies (Figure S4.7g and Figure S4.7h) which we confirmed were various phases including $Ti_{0.70}Zr_{0.30}Se_2$ and $Ti_{0.30}Zr_{0.70}Se_2$ based on EDS analysis (Table S4.9).

For $Ti_{0.75}Zr_{0.25}Se_2$, both mm and cm-sized single crystalline gold, hexagonal plates were isolated using elemental precursors at 900 °C using a 30 °C temperature gradient (Figure 4.6b). Based on EDS analysis, we confirmed crystals were indeed $Ti_{0.75}Zr_{0.25}Se_2$ (Table S4.9). For $Ti_{0.25}Zr_{0.75}Se_2$, we isolated minimal single crystalline hexagonal gold plates (Figure 4.6c), but we found the composition was the targeted $Ti_{0.25}Zr_{0.75}Se_2$ phase based on EDS analysis (Table S4.9). We also found wires (Figure S4.7i) with composition of $Ti_{0.03}Zr_{0.97}Se_3$ based on EDS (Table S4.9), although it was only a minor component.

Elemental mapping for $Ti_{0.50}Zr_{0.50}Se_2$, $Ti_{0.75}Zr_{0.25}Se_2$, and $Ti_{0.25}Zr_{0.75}Se_2$ showing homogeneous elemental distribution is provided in Figure S4.8.

Conclusions

Our work described here further expands synthetic routes leading to the isolation of single crystalline TMD solid solutions. We found that by leveraging the favored temperatures and synthetic conditions of $TiTe_2$, $ZrTe_2$, and $HfTe_2$, we could isolate solid solutions of $Ti_xZr_{1-x}Te_2$ (x = 0.30, 0.50, 0.80) and $Ti_xHf_{1-x}Te_2$ (x = 0.25, 0.40, 0.80) from 875–825 °C under CVT conditions. Using single crystal x-ray diffraction, we were able to establish the structures of both $Ti_{0.50}Zr_{0.50}Te_2$ and $Ti_{0.25}Hf_{0.75}Te_2$. Our data indicates that based on structural data such as lattice parameters, bond lengths, and bond angles, that these solid solutions have very similar structures to their corresponding analogs. For $Ti_xZr_{1-x}Se_2$ (x = 0.25, 0.50, 0.75), we determined single crystals with consistent composition could be isolated at a temperature gradient from 900–870 °C. We also found that a smaller temperature gradient (30 °C) was critical to phase isolation, especially based on our results when a higher gradient (100 °C) was used. Although we isolated single crystals of the $Ti_xZr_{1-x}Se_2$ compositions, we did find that crystal growth for $Ti_{0.25}Zr_{0.75}Se_2$ was minimal, and

requires further consideration. These findings expand the available routes of isolating TMD solid solutions which can aid in the understanding of metal alloying and the subsequent change in potential electronic properties.

Supporting Information

Experimental details for the single crystal x-ray diffraction structure determination of $Ti_{0.50}Zr_{0.50}Te_2$:

Data reduction[1]: Of the 533 unique reflections collected, 522 were observed ($I > 2\sigma(I)$). The linear absorption coefficient for Mo Kα radiation is 19.648 mm^{-1}. The data were integrated with the manufacturer's SAINT software and corrected for absorption effects using the Multi-Scan method (SADABS).

Structure solution and refinement[2]: Subsequent solution and refinement were performed using the SHELXTL-2018[3] solution package. The structure was solved by intrinsic phasing method using SHELXTL-2018 Software Package. Non-hydrogen atomic scattering factors were taken from the literature tabulations.[4] Non-hydrogen atoms were located from successive difference Fourier map calculations. Based on the SEM/EDS analysis that suggests the formula is $Ti_{0.50}Zr_{0.50}Te_2$ in the unit cell with Z = 1, the Ti and Zr atoms were found to share a same position with the ratio of 0.50/0.50 for Ti/Zr with formula of $Ti_{0.04167}Zr_{0.04167}Te_{0.1667}$ in an asymmetric unit. The twinning feature was detected and detwinning by applying a twin law (0 -1 0 -1 0 0 0 0 -1) dramatically improved the refinement. The final cycles of each refinement, all the atoms were refined in anisotropic displacement parameters. The crystal system of compound is trigonal, space group P-3m1 (No. 164) and the final residual values based on 10 variable parameters and 522 observed reflections (($I > 2\sigma(I)$) are $R1 = 0.0279$, $wR2 = 0.0930$, and those for all unique reflections are $R1 = 0.0288$, $wR2 = 0.0936$. The goodness-of-fit indicator for all data is 1.096. Peaks on the final difference map, ranging from 4.686 to -2.167 e/Å^3 around Te(1) (0.39 Å from Te(1)) and Te(1) (2.01 Å from Te(1)) atoms, are of no chemical significance. The large electron density residuals were greatly reduced to the current levels for this very heavily absorbed crystal by extensively exploiting the

parameters for optimization in additional spherical absorption correction plus applying a twin law in the refinement. The efforts have been made to resolve as many alerts as possible generated by CheckCIF. The current highest alerts are at level C.

Summary: The compound crystallizes in trigonal, space group $P\bar{3}m1$ (No. 164). The asymmetric unit contains a component in the form of $Ti_{0.04167}Zr_{0.04167}Te_{0.1667}$ in a polymeric structure with all the atoms residing on symmetries (the site symmetry is: -3m. for Ti(1) and Zr(1); 3m. for Te(1)). The whole formula in the unit cell is in the form of $Ti_{0.50}Zr_{0.50}Te_2$. Structure solution, refinement and the calculation of derived results were performed using the SHELXTL-2018[3] package of computer programs. Neutral atom scattering factors were those of Cromer and Waber,[4] and the real and imaginary anomalous dispersion corrections were those of Cromer.[5]

References:

1. Data Reduction:
   Intensity
   $I = [S - B/R]\cdot V$
   Standard Deviation in Intensity
   $s(I) = [S + B/R^2]^{1/2}\cdot V$
   Structure Factor
   $F = (I/Lp)^{1/2}$
   Standard Deviation in Structure Factor
   $\sigma(F) = \sigma(I)/(2\cdot F\cdot Lp)$
   Where: S = total scan count
   B = sum of background counts
   R = ratio of background counting time to scan counting time
   V = scan rate
   Lp = Lorentz-polarization correction

2. Least-Squares Refinement:
   Weighting Scheme
   $w = 1/[\ \sigma^2(F_o^2) + 0.0681*P)^2 + 0.0984*P]$ where $P = [\mathrm{Max}(F_o^2\ , 0) + 2*F_c^2]/3$;
   Residuals
   R-factors:
   $R = \Sigma\ |\ |\ F_o\ |\ -\ |\ F_c\ |\ |\ /\Sigma\ |\ F_o\ |\ ;$
   Weighted R-factor on F^2:
   $wR2 = [\Sigma[w\ (F_o^2 - F_c^2)^2] / \Sigma[w(F_o^2)^2]]^{1/2}$;

Goodness of Fit Indicator:

goodness-of-fit = $[\Sigma[w\ (F_o^2 - F_c^2)^2] / (N_{observns} - N_{params})\ ]^{1/2}$.

3. (a) Sheldrick, G.M. *SHELXTL-2018*, *Crystallographic Computing System*; Bruker Analytical X-Ray Instruments: Madison, WI, 2018; (b) Sheldrick, G.M. *A Short History of SHELX*, Acta Cryst. 2008, A64, 112.

4. Cromer, D.T. and Waber, J.T. International Tables for X-ray Crystallography, Vol. IV, Table 2.2B, The Kynoch Press, Birmingham England, 1974.

5. Cromer, D.T. International Tables for X-ray Crystallography, Vol. IV, Table 2.3.1, The Kynoch Press, Birmingham England, 1974.

Table S4.1 Selected bond length comparison for $TiTe_2$, $Ti_{0.50}Zr_{0.50}Te_2$, and $ZrTe_2$.

	$TiTe_2$ Bond Lengths (Å)	**$Ti_{0.50}Zr_{0.50}Te_2$ Bond Lengths (Å)**	**$ZrTe_2$ Bond Lengths (Å)**
M-Te^1; M-Te^4 M-Te^2; M-Te^5 M-Te^3; M-Te^6	2.7697	2.8205(2)	2.8982

Table S4.2 Selected bond angle comparison for $TiTe_2$, $Ti_{0.50}Zr_{0.50}Te_2$, and $ZrTe_2$.

	$TiTe_2$ Bond Angles (°)	**$Ti_{0.50}Zr_{0.50}Te_2$ Bond Angles (°)**	**$ZrTe_2$ Bond Angles (°)**
∠Te^1-M-Te^2 ∠Te^2-M-Te^3 ∠Te^1-M-Te^3 ∠Te^4-M-Te^5 ∠Te^5-M-Te^6 ∠Te^4-M-Te^6	85.975	85.951(9)	86.082
∠Te^1-M-Te^4 ∠Te^3-M-Te^6	94.025	94.049(9)	93.918

Table S4.3 Atomic coordinates (x 10^4) and equivalent isotropic displacement parameters ($Å^2$ x 10^3) for $Ti_{0.50}Zr_{0.50}Te_2$. U_{eq} is defined as 1/3 of the trace of the orthogonalized *Uij* tensor.

Atom	*x*	*y*	*z*	U_{eq}
Te(1)	6667	3333	2345(1)	13(1)
Zr(1)	10000	0	5000	18(1)
Ti(1)	10000	0	5000	9(1)

Table S4.4 Anisotropic displacement parameters (A^2 x 10^3) for $Ti_{0.50}Zr_{0.50}Te_2$. The anisotropic displacement factor exponent takes the form: -2 pi^2 [h^2 a*^2 U11 + ... + 2 h k a* b* U12].

Atom	U11	U22	U33	U23	U13	U12
Te(1)	14(1)	14(1)	12(1)	0	0	7(1)
Zr(1)	17(1)	17(1)	19(2)	0	0	9(1)
Ti(1)	10(1)	10(1)	6(1)	0	0	5(1)

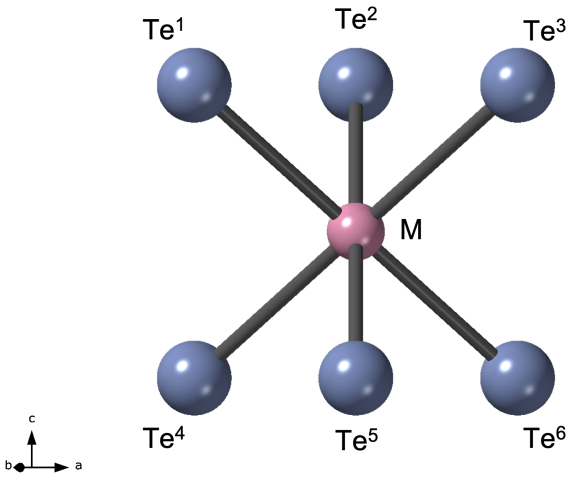

Figure S4.1 Crystal structure of $Ti_{0.50}Zr_{0.50}Te_2$ illustrating metal coordination (where M = Ti or Zr) to Te.

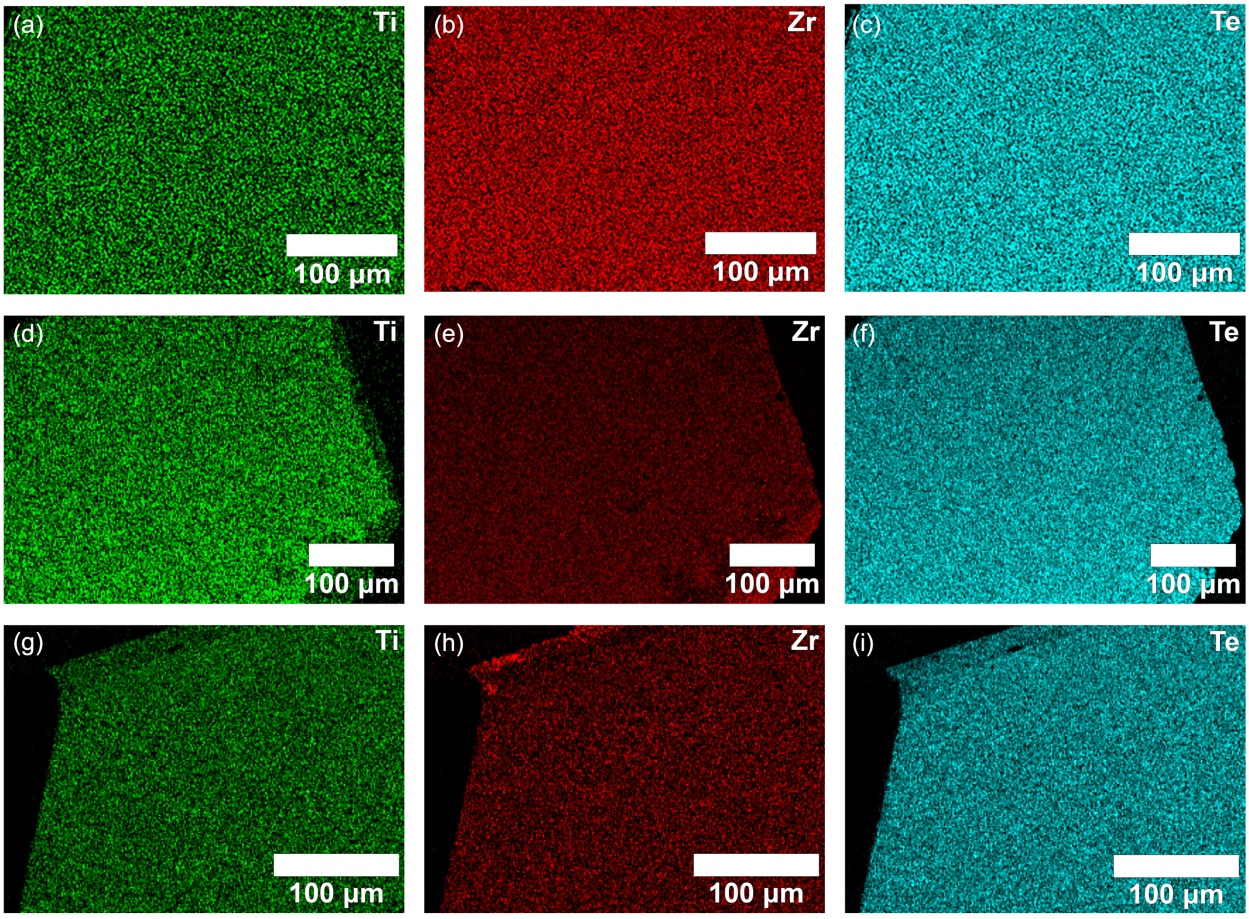

Figure S4.2 Elemental mapping illustrating homogeneous distribution of Ti, Zr, and Te in (a)-(c) $Ti_{0.30}Zr_{0.70}Te_2$, (d)-(f) $Ti_{0.50}Zr_{0.50}Te_2$, (g)-(i) and $Ti_{0.80}Zr_{0.20}Te_2$.

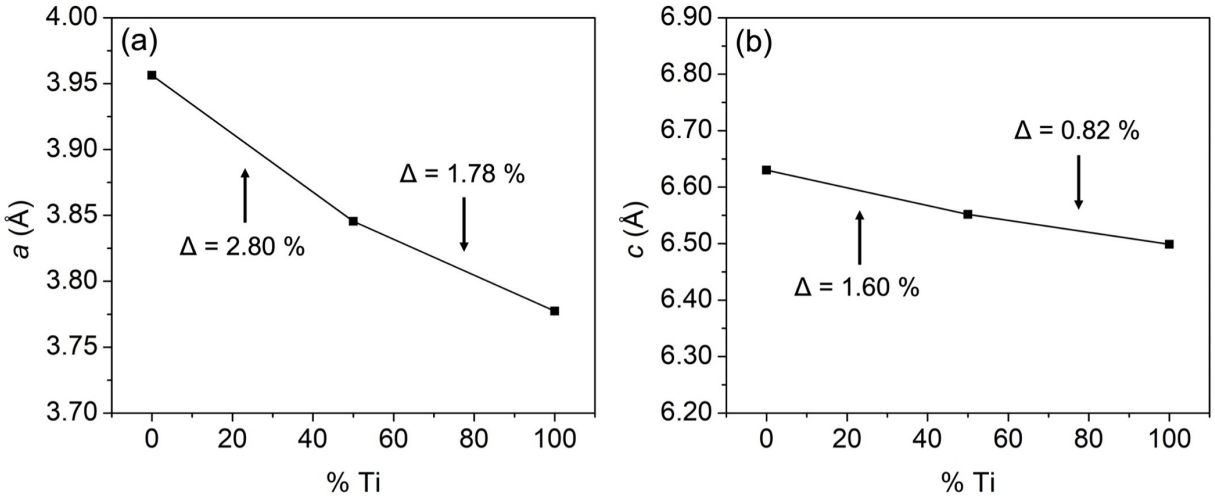

Figure S4.3 Composition plots of $Ti_xZr_{1-x}Te_2$ as a function of increasing Ti percentage vs (a) *a* and (b) *c* lattice parameters.

Experimental details for the single crystal x-ray diffraction structure determination of $Ti_{0.25}Hf_{0.75}Te_2$:

Data reduction[1]: Of the 127 unique reflections collected, 127 were observed ($I > 2\sigma(I)$). The linear absorption coefficient for Mo Kα radiation is 39.216 mm^{-1}. The data were integrated with the manufacturer's SAINT software and corrected for absorption effects using the Multi-Scan method (SADABS).

Structure solution and refinement[2]: Subsequent solution and refinement were performed using the SHELXTL-2018[3] solution package. The structure was solved by direct method using SHELXTL-2018 Software Package. Non-hydrogen atomic scattering factors were taken from the literature tabulations.[4] Non-hydrogen atoms were located from successive difference Fourier map calculations. Based on the SEM/EDS analysis that suggests the formula is $Hf_{0.75}Ti_{0.25}Te_2$ in the unit cell with Z = 1, the Hf and Ti atoms were assumed to share a same position with the ratio of 0.75/0.25 for Hf/Ti with formula of $Hf_{0.06250}Ti_{0.02083}Te_{0.16667}$ in an asymmetric unit. The twinning

feature was detected and detwinning by applying a twin law (0 -1 0 -1 0 0 0 0 -1) dramatically improved the refinement. In the final cycles of each refinement, all the atoms were refined in anisotropic displacement parameters with little bit restraints on Hf and Ti atoms. The crystal system of compound is trigonal, space group P-3m1 (No. 164) and the final residual values based on 10 variable parameters and 127 observed reflections ($I > 2\sigma(I)$) are $R1 = 0.0466$, $wR2 = 0.1498$, and those for all unique reflections are $R1 = 0.0466$, $wR2 = 0.1498$. The goodness-of-fit indicator for all data is 1.013. Peaks on the final difference map, ranging from 3.793 to -4.191 e/Å^3 around Te(1) (2.25 Å from Te(1)) and Te(1) (1.15 Å from Te(1)) atom, are of no chemical significance. The large electron density residuals were greatly reduced to the current levels for this very heavily absorbed crystal by extensively exploiting the parameters for optimization in additional spherical absorption correction plus applying a twin law in the refinement. The efforts have been made to resolve as many alerts as possible generated by CheckCIF. The current highest alerts are at level C.

Summary: The compound crystallizes in trigonal, space group P-3m1 (No. 164). The asymmetric unit contains a component in the form of $Hf_{0.06250}Ti_{0.02083}Te_{0.16667}$ in a polymeric structure with all the atoms residing on symmetries (the site symmetry is: -3m. for Hf(1) and Ti(1); 3m. for Te(1)). The whole formula in the unit cell is in the form of $Hf_{0.75}Ti_{0.25}Te_2$. Structure solution, refinement and the calculation of derived results were performed using the SHELXTL-2018[3] package of computer programs. Neutral atom scattering factors were those of Cromer and Waber,[4] and the real and imaginary anomalous dispersion corrections were those of Cromer.[5]

References:

1. Data Reduction:
   Intensity
      $I = [S - B/R] \cdot V$
   Standard Deviation in Intensity

$s(I) = [S + B/R^2]^{1/2} \cdot V$

Structure Factor

$F = (I/Lp)^{1/2}$

Standard Deviation in Structure Factor

$\sigma(F) = \sigma(I)/(2 \cdot F \cdot Lp)$

Where: S = total scan count
B = sum of background counts
R = ratio of background counting time to scan counting time
V = scan rate
Lp = Lorentz-polarization correction

2. Least-Squares Refinement:

Weighting Scheme

$w = 1/[\ \sigma^2(F_o^2) + 0.1401*P)^2 + 1.2912*P]$ where $P = [\mathrm{Max}(F_o^2\ , 0) + 2*F_c^2]/3$;

Residuals

R-factors:

$R = \Sigma\ |\ |\ F_o\ |\ -\ |\ F_c\ |\ |\ /\Sigma\ |\ F_o\ |\ ;$

Weighted R-factor on F^2:

$wR2 = [\Sigma[w\ (F_o^2 - F_c^2)^2] / \Sigma[w(F_o^2)^2]]^{1/2}$;

Goodness of Fit Indicator:

goodness-of-fit = $[\Sigma[w\ (F_o^2 - F_c^2)^2] /(N_{observns}-N_{params})\ ]^{1/2}$.

3. (a) Sheldrick, G.M. *SHELXTL-2018*, *Crystallographic Computing System*; Bruker Analytical X-Ray Instruments: Madison, WI, 2018; (b) Sheldrick, G.M. *A Short History of SHELX*, Acta Cryst. 2008, A64, 112.

4. Cromer, D.T. and Waber, J.T. International Tables for X-ray Crystallography, Vol. IV, Table 2.2B, The Kynoch Press, Birmingham England, 1974.

5. Cromer, D.T. International Tables for X-ray Crystallography, Vol. IV, Table 2.3.1, The Kynoch Press, Birmingham England, 1974.

Table S4.5 Selected bond length comparison for $TiTe_2$, $Ti_{0.25}Hf_{0.75}Te_2$, and $HfTe_2$.

	$TiTe_2$ Bond Lengths (Å)	**$Ti_{0.25}Hf_{0.75}Te_2$ Bond Lengths (Å)**	**$HfTe_2$ Bond Lengths (Å)**
M-Te[1]; M-Te[4] M-Te[2]; M-Te[5] M-Te[3]; M-Te[6]	2.7697	2.8472(9)	2.8238

Table S4.6 Selected bond angle comparison for $TiTe_2$, $Ti_{0.25}Hf_{0.75}Te_2$, and $HfTe_2$.

	$TiTe_2$ Bond Angles (°)	**$Ti_{0.25}Hf_{0.75}Te_2$ Bond Angles (°)**	**$HfTe_2$ Bond Angles (°)**
∠Te^1-M-Te^2 **∠Te^2-M-Te^3** **∠Te^1-M-Te^3** **∠Te^4-M-Te^5** **∠Te^5-M-Te^6** **∠Te^4-M-Te^6**	85.975	86.43(3)	88.787
∠Te^1-M-Te^4 **∠Te^3-M-Te^6**	94.025	93.57(3)	91.213

Table S4.7 Atomic coordinates (x 10^4) and equivalent isotropic displacement parameters ($Å^2$ x 10^3) for $Ti_{0.25}Hf_{0.75}Te_2$. U_{eq} is defined as 1/3 of the trace of the orthogonalized *Uij* tensor.

Atom	*x*	*y*	*z*	U_{eq}
Hf(1)	0	0	0	14(1)
Te(1)	-3333	3333	2637(2)	14(1)
Ti(1)	0	0	0	40(20)

Table S4.8 Anisotropic displacement parameters (A^2 x 10^3) for $Ti_{0.25}Hf_{0.75}Te_2$. The anisotropic displacement factor exponent takes the form: -2 pi^2 [h^2 a*^2 U11 + ... + 2 h k a* b* U12].

Atom	U11	U22	U33	U23	U13	U12
Hf(1)	13(1)	13(1)	18(2)	0	0	6(1)
Te(1)	13(1)	13(1)	16(1)	0	0	6(1)
Ti(1)	40(20)	40(20)	40(40)	0	0	20(12)

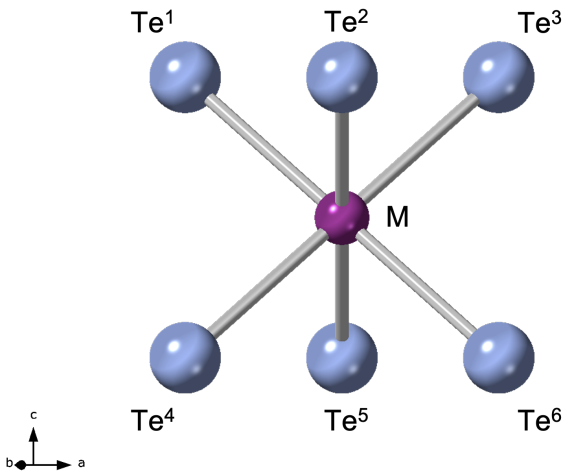

Figure S4.4 Crystal structure of $Ti_{0.25}Hf_{0.75}Te_2$ illustrating metal coordination (where M = Ti or Hf) to Te.

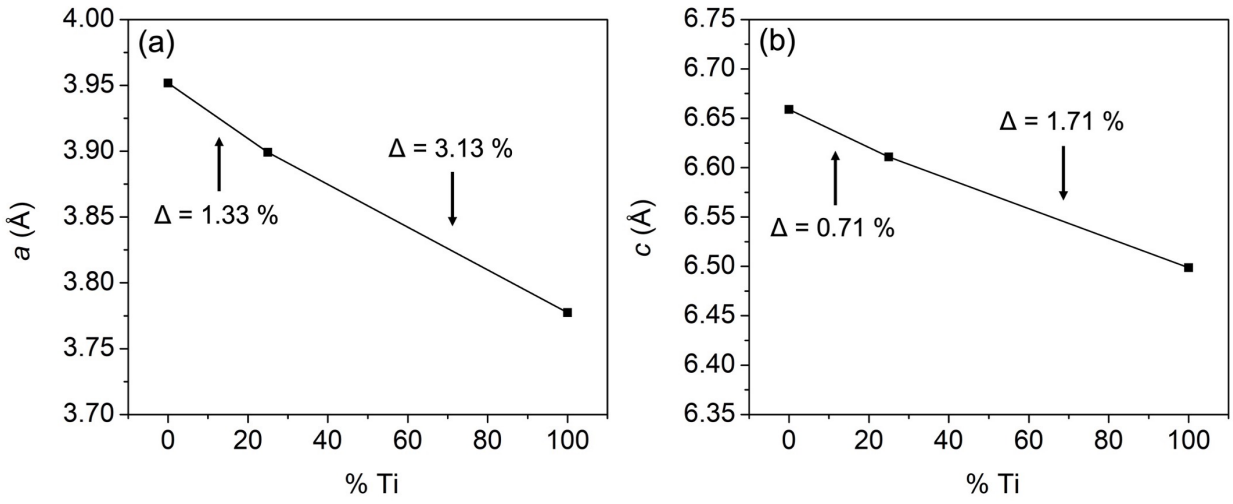

Figure S4.5 Composition plots of $Ti_xHf_{1-x}Te_2$ as a function of increasing Ti percentage vs (a) *a* and (b) *c* lattice parameters.

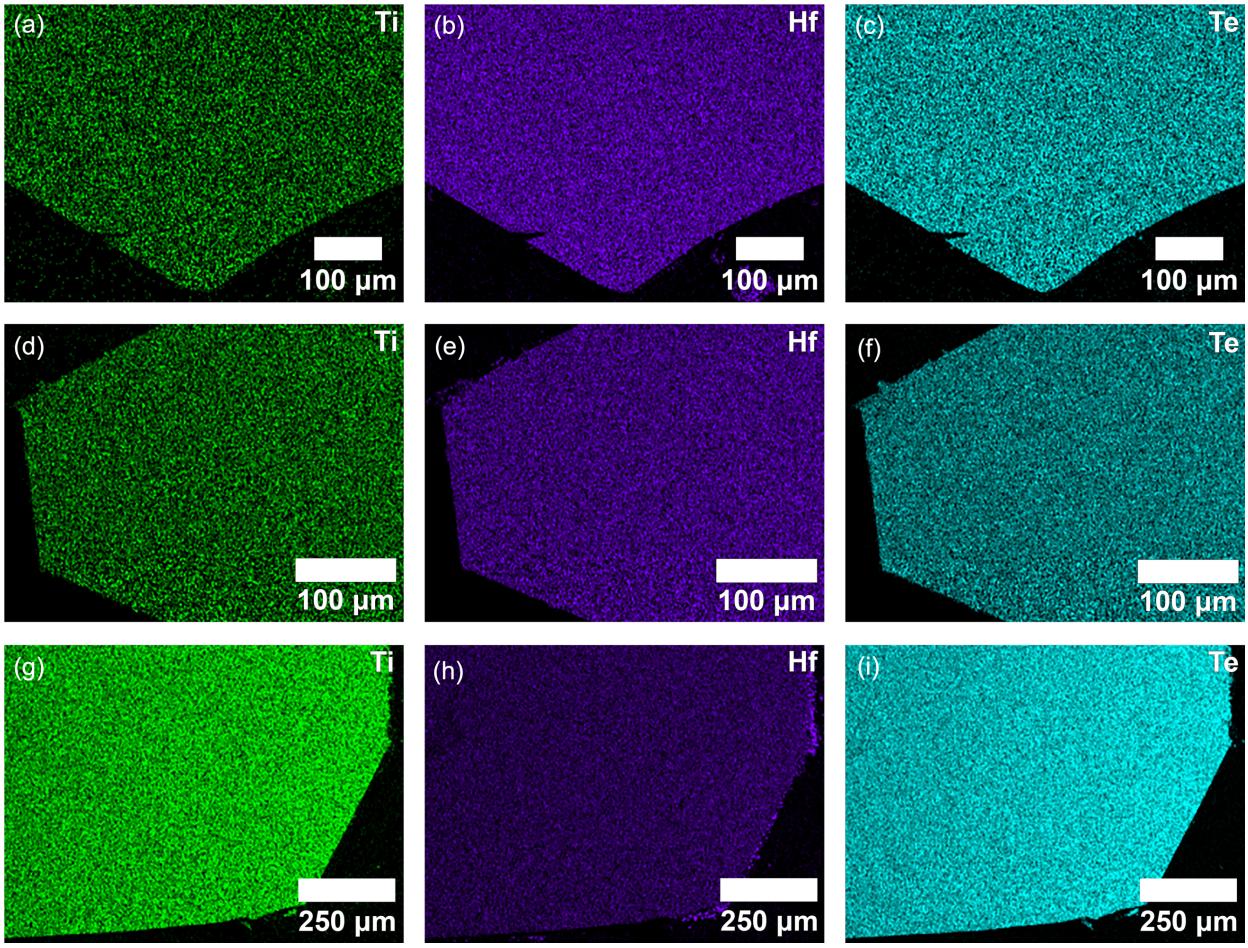

Figure S4.6 Elemental mapping illustrating homogeneous distribution of Ti, Hf, and Te in (a)-(c) $Ti_{0.25}Hf_{0.75}Te_2$, (d)-(f) $Ti_{0.40}Hf_{0.60}Te_2$, (g)-(i) and $Ti_{0.80}Hf_{0.20}Te_2$.

Table S4.9 $Ti_xZr_{1-x}Se_2$ reaction list with target compositions, synthetic conditions used, and experimental compositions calculated using atomic percentages and normalizing the Se percentage.

Target Composition	Synthetic Conditions	Atomic % by EDS			Experimental Result
		Ti	Zr	Se	
$Ti_{0.50}Zr_{0.50}Se_2$	900 → 870 °C; elements	17.1	17.3	65.6	$Ti_{0.50}Zr_{0.50}Se_2$
$Ti_{0.50}Zr_{0.50}Se_2$	900 → 870 °C; Polycrystalline $TiSe_2$ and $ZrSe_2$ ground together	18.2	16.0	65.8	$Ti_{0.50}Zr_{0.50}Se_2$
$Ti_{0.50}Zr_{0.50}Se_2$	900 → 800 °C; elements	22.8	11.4	65.8	$Ti_{0.70}Zr_{0.30}Se_2$
		19.5	14.7	65.8	$Ti_{0.60}Zr_{0.40}Se_2$
$Ti_{0.50}Zr_{0.50}Se_2$	975 → 875 °C; elements	26.1	7.8	66.1	$Ti_{0.80}Zr_{0.20}Se_2$
		23.1	11.0	65.9	$Ti_{0.70}Zr_{0.30}Se_2$
		20.8	13.7	65.6	$Ti_{0.60}Zr_{0.40}Se_2$
$Ti_{0.50}Zr_{0.50}Se_2$	600 → 500 °C; elements	11.8	22.8	65.4	$Ti_{0.30}Zr_{0.70}Se_2$
		23.2	10.8	66.0	$Ti_{0.70}Zr_{0.30}Se_2$
$Ti_{0.25}Zr_{0.75}Se_2$	900 → 870 °C; elements	8.8	25.4	65.8	$Ti_{0.25}Zr_{0.75}Se_2$
		1.0	24.2	74.8	$Ti_{0.03}Zr_{0.97}Se_3$
$Ti_{0.75}Zr_{0.25}Se_2$	900 → 870 °C; elements	25.9	8.0	66.1	$Ti_{0.75}Zr_{0.25}Se_2$

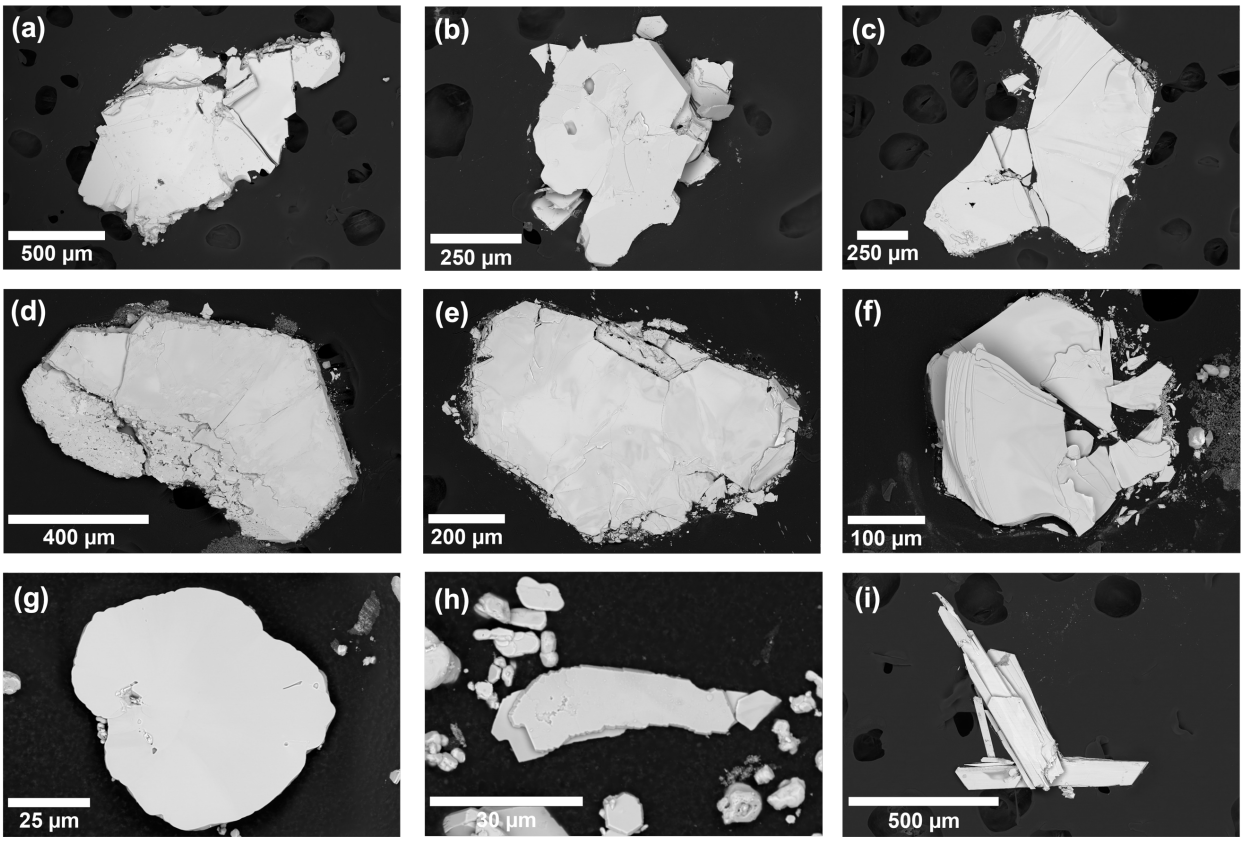

Figure S4.7 SEM imaging of single crystalline: (a) $Ti_{0.50}Zr_{0.50}Se_2$ using polycrystalline $TiSe_2$ and $ZrSe_2$ isolated from 900 → 870 °C; (b) $Ti_{0.70}Zr_{0.30}Se_2$ and (c) $Ti_{0.60}Zr_{0.40}Se_2$ from the attempted synthesis of $Ti_{0.50}Zr_{0.50}Se_2$ isolated from 900 → 800 °C; (d) $Ti_{0.80}Zr_{0.20}Se_2$, (e) $Ti_{0.70}Zr_{0.30}Se_2$ and (f) $Ti_{0.60}Zr_{0.40}Se_2$ from the attempted synthesis of $Ti_{0.50}Zr_{0.50}Se_2$ isolated from 975 → 875 °C; (g) $Ti_{0.30}Zr_{0.70}Se_2$ and (h) $Ti_{0.70}Zr_{0.30}Se_2$ from the attempted synthesis of $Ti_{0.50}Zr_{0.50}Se_2$ isolated from 600 → 500 °C; (i) $Ti_{0.03}Zr_{0.97}Se_3$ from the attempted synthesis of $Ti_{0.25}Zr_{0.75}Se_2$ isolated from 900 → 870 °C.

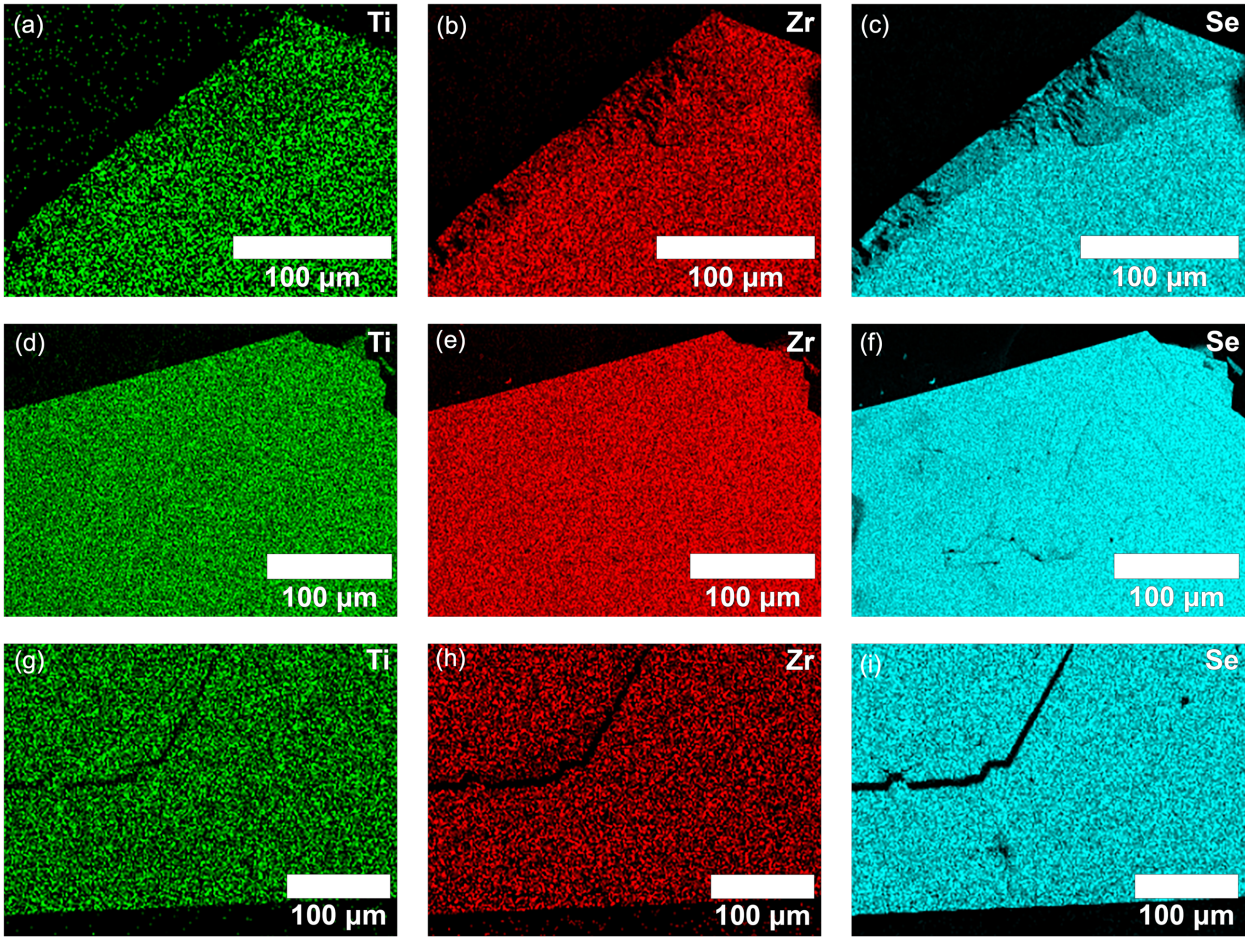

Figure S4.8 Elemental mapping illustrating homogeneous distribution of Ti, Zr, and Se in (a)-(c) $Ti_{0.25}Zr_{0.75}Se_2$, (d)-(f) $Ti_{0.50}Zr_{0.50}Se_2$, (g)-(i) and $Ti_{0.75}Zr_{0.25}Se_2$.

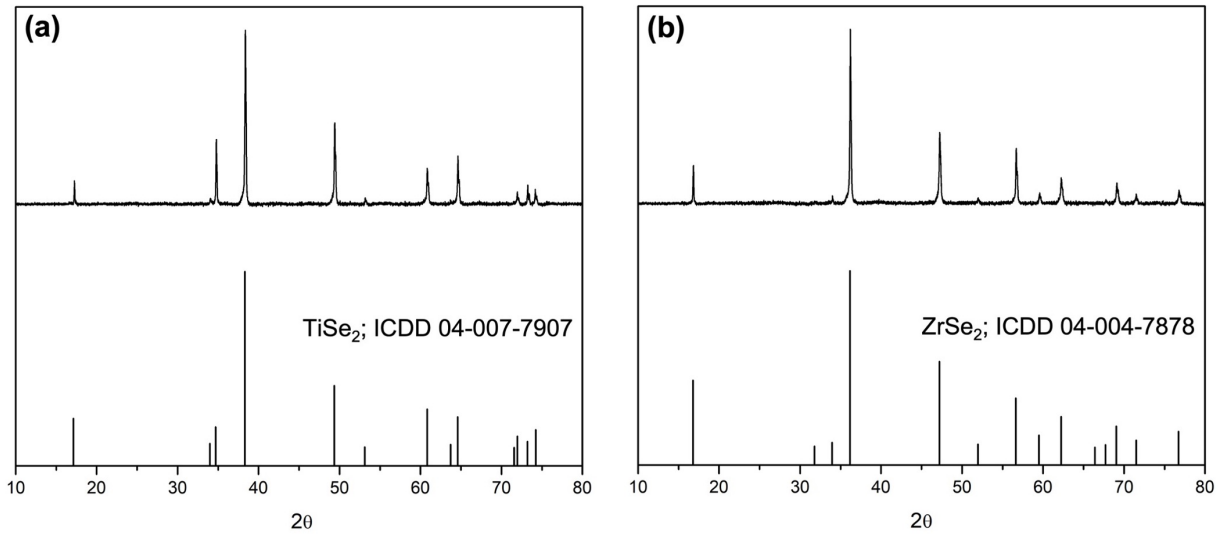

Figure S4.9 PXRD patterns of polycrystalline $TiSe_2$ and $ZrSe_2$.

References

1. Novoselov, K.; Geim, A.; Morozov, S.; Jiang, D.; Zhang, Y.; Dubonos, S.; Grigorieva, I.; Firsov, A. Electric Field Effect in Atomically Thin Carbon Films. *Science* **2004**, *306*, 666-669.

2. Choi, W.; Choudhary, N.; Han, G.; Park, J.; Akinwande, D.; Lee, Y. Recent Development of Two-Dimensional Transition Metal Dichalcogenides and Their Applications. *Mater. Tod.* **2017**, *20*, 116-130.

3. Song, L.; Ci, L.; Lu, H.; Sorokin, P.; Jin, C.; Ni, J.; Kvashnin, A.; Kvashnin, D.; Lou, J.; Yakobson, B.; Ajayan, P. Large Scale Growth and Characterization of Atomic Hexagonal Boron Nitride Layers. *Nano Lett.* **2010**, *10*, 3209-3215.

4. Li, L.; Yu, Y.; Ye, G.; Ge, Q.; Ou, X.; Wu, H.; Feng, D.; Chen, X.; Zhang, Y. Black Phosphorus Field-Effect Transistors. *Nat. Nanotechnol.* **2014**, *9*, 372-377.

5. Tao, W.; Kong, N.; Ji, X.; Zhang, Y.; Sharma, A.; Ouyang, J.; Qi, B.; Wang, J.; Xie, N.; Kang, C.; Zhang, H.; Farokhzad, O.; Kim, J. Emerging Two-Dimensional Monoelemental Materials (Xenes) for Biomedical Applications. *Chem. Soc. Rev.* **2019**, *48*, 2891-2912.

6. Butler, S.; Hollen, S.; Cao, L.; Cui, Y.; Gupta, J.; Gutiérrez, H.; Heinz, T.; Hong, S.; Huang, J.; Ismach, A.; Johnston-Halperin, E.; Kuno, M.; Plashnitsa, V.; Robinson, R.; Ruoff, R.; Salahuddin, S.; Shan, J.; Shi, L.; Spencer, M.; Terrones, M.; Windl, W.; Goldberger, J. Progress, Challenges, and Opportunities in Two-Dimensional Materials Beyond Graphene. *ACS Nano* **2013**, *7*, 2898-2926.

7. Su, J.; Liu, K.; Wang, F.; Jin, B.; Guo, Y.; Liu, G.; Li, H.; Zhai, T. van der Waals 2D Transition Metal Tellurides. *Adv. Mater. Interfaces* **2019**, *6*, 1900741.

8. Manzeli, S.; Ovchinnikov, D.; Pasquier, D.; Yazyev, O.; Kis, A. 2D Transition Metal Dichalcogenides. *Nat. Rev. Mater.* **2017**, *2*, 17033.

9. Wang, Q.; Kalantar-Zadeh, K.; Kis, A.; Coleman, J.; Strano, M. Electronics and Optoelectronics of Two-Dimensional Transition Metal Dichalcogenides. *Nat. Nanotech.* **2012**, *7*, 699-712.

10. Ho, C.; Wu, C.; Huang, Y.; Liao, P.; Tiong, K. Temperature Dependence of Energies and Broadening Parameters of the Band-Edge Excitons of $Mo_{1-x}W_xS_2$ Single Crystals. *J. Phys. Condens. Matt.* **1998**, *10*, 9317-9328.

11. Delphine, S.; Jayachandran, M.; Sanjeeviraja, C. Review of Material Properties of (Mo/W)Se_2-Layered Compound Semiconductors Useful for Photoelectrochemical Solar Cells. *Crystallogr. Rev.* **2011**, *17*, 281-301.

12. Loh, S.; Xia, X.; Wilson, N.; Hine, N. Strong In-Plane Anisotropy in the Electronic Properties of Doped Transition Metal Dichalcogenides Exhibited in $W_{1-x}Nb_xS_2$. *Phys. Rev. B* **2021**, *103*, 245410.

13. Wang, S.; Cavin, J.; Hemmat, Z.; Kumar, K.; Ruckel, A.; Majidi, L.; Gholivand, H.; Dawood, R.; Cabana, J.; Guisinger, N.; Klie, R.; Khalili-Araghi, F.; Mishra, R.; Salehi-Khojin, A. Phase-Dependent Band Gap Engineering in Alloys of Metal-Semiconductor Transition Metal Dichalcogenides. *Adv. Funct. Mater.* **2020**, *30*, 2004912.

14. Aiura, Y.; Hase, I.; Yagi-Watanabe, K.; Bando, H.; Ozawa, K.; Tanaka, K.; Kitagawa, R.; Maruyama, S.; Iwase, T.; Nishihara, Y.; Horiba, K.; Shiino, O.; Oshima, M.; Nakatake, M.; Kubota, M.; Ono, K. Increase in Charge-Density-Wave Potential of 1*T*-TaS_xSe_{2-x}. *Phys. Rev. B* **2004**, *69*, 245123.

15. Moustafa, M.; Zandt, T.; Janowitz, C.; Manzke, R. Growth and Band Gap Determination of the ZrS_xSe_{2-x} Single Crystal Series. *Phys. Rev. B* **2009**, *80*, 035206.

16. Gaiser, C.; Zandt, T.; Krapf, A.; Serverin, R.; Janowitz, C.; Manzke, R. Band-Gap Engineering with HfS_xSe_{2-x}. *Phys. Rev. B* **2004**, *69*, 075205.

17. Ho, C.; Huang, Y.; Liao, P.; Tiong, K. Piezoreflectance Study of Band-Edge Excitons of $ReS_{2-x}Se_x$ Single Crystals. *Phys. Rev. B* **1998**, *58*, 12575-12578.

18. Rimmington, H.; Balchin, A. The Growth by Iodine Vapour Transport Techniques and the Crystal Structures of Layer Compounds in the Series TiS_xSe_{2-X}, TiS_xTe_{2-X}, $TiSe_xTe_{2-X}$. *J. Cryst. Growth* **1974**, *21*, 171-181.

19. Gupta, H.; Sood, G.; Sinha, M.; Tripathi, B. Two-Mode Behaviour in Mixed Layer Crystal $HfS_{2-x}Te_x$ ($0 \leq x \leq 2$). *Phys. B: Condens. Matter* **1989**, *159*, 383-387.

20. Hodul, D.T.; Sienko, M.J. $Hf(Se_xTe_{1-x})_2$: Deviation from Vegard's Law in Mixed Systems. *Inorg. Chem.* **1981**, 20, 3655-3659.

21. Hodul, D.; Sienko, M. Solid State Studies of $HfSe_{2-X}Te_x$ and $HfTe_{2-X}$. *Physica B+C* **1980**, *99*, 215-218.

22. Fragkos, S.; Tsipas, P.; Xenogiannopoulou, E.; Panayiotatos, Y.; Dimoulas, A. Type-III Dirac Fermions in $Hf_xZr_{1-x}Te_2$ Semimetal Candidate. *J. Appl. Phys.* **2021**, *129*, 075104.

23. Muhammad, Z.; Zhang, B.; Lv, H.; Shan, H.; Rehman, Z.; Chen, S.; Sun, Z.; Wu, X.; Zhao, A.; Song, L. Transition from Semimetal to Semiconductor in $ZrTe_2$ Induced by Se Substitution. *ACS Nano* **2019**, *14*, 835-841.

24. Cybulski, Z.; Feltz, A.; Andratschke, M. Structure and Properties of Quaternary Chalcogenides: The Structure and Intercalation Behaviour of $TiZrTe_4$. *Mat. Res. Bull.* **1989**, *24*, 157-162.

25. Cybulski, Z.A. Ternary and Quaternary Selenide Compounds M^{I} TiZrSe4 (M^{I} = Li, Ag). *Mater. Sci. Forum* **1992**, *91-93*, 159-164.

26. Kirby, R.; Fagerquist, R.; Nieveen, W. Electronic Properties Of Zr-Doped $TiSe_2$. *Solid State Commun.* **1984**, *51*, 131-134.

27. Freund, G.; Kirby, R. Lattice Dynamics Of Mixed Crystals Of $TiSe_2$. *Phys. Rev. B* **1984**, *30*, 7122-7131.

28. Titov, A.N.; Titova, S.G. Phase Diagram and Electronic Properties of Ag_xTiTe_2. *J. Alloys Compd.* **1997**, *256*, 13-17.

29. Zhang, M.; Wang, X.; Rahman, A.; Zeng, Q.; Huang, D.; Dai, R.; Wang, Z.; Zhang, Z. Pressure-Induced Topological Phase Transitions and Structural Transition in 1T-$TiTe_2$ Single Crystal. *Appl. Phys. Lett.* **2018**, *112*, 041907.

30. Mangelsen, S.; Naumov, P.; Barkalov, O.; Medvedev, S.; Schnelle, W.; Bobnar, M.; Mankovsky, S.; Polesya, S.; Näther, C.; Ebert, H.; Bensch, W. Large Nonsaturating Magnetoresistance and Pressure-Induced Phase Transition in the Layered Semimetal *Phys. Rev. B* **2017**, *96*, 205148.

31. Correa, L.; Ferreira, P.; Faria, L.; Dorini, T.; Luz, M.; Fisk, Z.; Torikachvili, M.; Eleno, L.; Machado, A. Evidence for Multiband Superconductivity and Charge Density Waves in Ni-Doped $ZrTe_2$. *J. Alloys Compd.* **2022**, *907*, 164477.

32. Kabiraj, A.; Mahapatra, S. Machine-Intelligence-Driven High-Throughput Prediction of 2D Charge Density Wave Phases. *J. Phys. Chem. Lett.* **2020**, *11*, 6291-6298.

33. Greenaway, D.L.; Nitsche, R. Preparation and Optical Properties of Group IV-VI_2 Chalcogenides Having the CdI_2 Structure. *J. Phys. Chem. Solids* **1965**, *26*, 1445-1458.

34. de Boer, D.; van Bruggen, C.; Bus, G.; Coehoorn, R.; Haas, C.; Sawatzky, G.; Myron, H.; Norman, D.; Padmore, H. Titanium Ditelluride: Band Structure, Photoemission, and Electrical and Magnetic Properties. *Phys. Rev. B* **1984**, *29*, 6797-6809.

35. Arnaud, Y.; Chevreton, M. Etude Comparative des Composés TiX_2 (X = S, Se, Te). Structures de $TiTe_2$ et TiSeTe. *J. Solid State Chem.* **1981**, *39*, 230-239.

36. Zhang, B.; Muhammad, Z.; Wang, P.; Cui, S.; Li, Y.; Wang, S.; Wu, Y.; Liu, Z.; Zhu, H.; Liu, Y. Zhang, G.; Liu, D.; Song, L. Sun, Z. Electronic Structures of Cr-Intercalated $ZrTe_2$ Revealed by Angle-Resolved Photoemission Spectroscopy. *J. Phys. Chem.* **2020**, *124*, 16561-16567.

37. Muhammad, Z.; Usman, M.; Ullah, S.; Zhang, B.; Lu, Q.; Zhu, L.; Hu, R. Lattice Dynamics, Optical and Thermal Properties of Quasi-Two-Dimensional Anisotropic Layered Semimetal $ZrTe_2$. *Inorg. Chem. Front.* **2021**, *8*, 3885-3892.

38. Kar, I.; Chatterjee, J.; Harnagea, L.; Kushnirenko, Y.; Fedorov, A.; Shrivastava, D.; Büchner, B.; Mahadevan, P.; Thirupathaiah, S. Metal-Chalcogen Bond-Length Induced Electronic Phase Transition from Semiconductor to Topological Semimetal in ZrX_2 (X=Se and Te). *Phys. Rev. B* **2020**, *101*, 165122.

39. Bhavsar, D.N.; Jani, A.R. Structural and Transport Properties of $ZrTe_2$ Single Crystals. *J. Optoelectron. Adv. Mater.* **2014**, *16*, 215-220.

40. Geremew, A.; Bloodgood, M.; Aytan, E.; Woo, B.; Corber, S.; Liu, G.; Bozhilov, K.; Salguero, T.; Rumyantsev, S.; Rao, M.; Balandin, A.A. Current Carrying Capacity of Quasi-1D $ZrTe_3$ van der Waals Nanoribbons. *IEEE Electron Device Lett.* **2018**, *39*, 735-738.

41. Geremew, A.; Rumyantsev, S.; Bloodgood, M.; Salguero, T.; Balandin, A. Unique Features of the Generation–Recombination Noise in Quasi-One-Dimensional van der Waals Nanoribbons. *Nanoscale* **2018**, *10*, 19749-19756.

42. Lévy, F.; Berger, H. Single Crystals of Transition Metal Trichalcogenides. *J. Cryst. Growth* **1983**, *61*, 61-68.

43. Mangelsen, S.; Bensch, W. $HfTe_2$: Enhancing Magnetoresistance Properties by Improvement of the Crystal Growth Method. *Inorg. Chem.* **2019**, *59*, 1117-1124.

44. Brattås, L.; Kjekshus, A. On the Properties of the Zirconium and Hafnium Dichalcogenides. *Acta Chem. Scand.* **1973**, *27*, 1290-1298.

45. Hodul, D.; Stacy, M. Anomalies in the Properties of $Hf(S_{2-x}Te_x)_{1-y}$ and $Hf(Se_{2-x}Te_x)_{1-y}$ Near the Metal-Insulator Transition. J. Solid State Chem. **1984**, *54*, 438-446.

46. Stonemeyer, S.; Cain, J.; Oh, S.; Azizi, A.; Elasha, M.; Thiel, M.; Song, C.; Ercius, P.; Cohen, M.; Zettl, A. Stabilization of $NbTe_3$, VTe_3, and $TiTe_3$ via Nanotube Encapsulation. *J. Am. Chem. Soc.* **2021**, *143*, 4563-4568.

CHAPTER 5

CONCLUSIONS AND FUTURE WORK

Conclusions and Future Work

Low-dimensional layered materials have attracted a significant amount of interest from researchers due to their unique properties and promising applications.[1] At the forefront of these materials are the transition metal chalcogenides, which include both the transition metal di- and trichalcogenides. Thus far, a significant amount of research has been spent on the synthesis, tunability, characterization, and property investigation of these materials particularly.[2,3] The work described in this dissertation aims to further expand previous work with these materials with an emphasis on group IV transition metal chalcogenides.

In Chapter II, we specifically looked at isolating both polycrystalline and single crystalline $HfTe_3$. The work described in this chapter was driven by the exceptional properties reported for $ZrTe_3$ including recent reports of its exceptionally high current density (~100 MA/cm^2).[4,5] Furthermore, we were interested in resolving previous contradictions in the literature and providing reproducible synthetic pathways.[6,7] In our work we determined polycrystalline $HfTe_3$ could be isolated at 550 °C under solid state conditions. We also found that choice in Hf precursor and cooling route could affect the final phase. To isolate single crystalline $HfTe_3$, we determined 530 °C under chemical vapor transport (CVT) conditions was the most ideal temperature, and that slight deviations in temperature could favor neighboring phases ($HfTe_2$ and $HfTe_5$). Furthermore, we found it was necessary to use polycrystalline $HfTe_3$ that was ball milled under Ar atmosphere

for 1 h as a precursor, versus elemental precursors which favored neighboring phases. We also discovered morphology tunability of single crystal $HfTe_3$ when using different transport agents. This work further expanded synthetic routes in isolating $HfTe_3$, and also focused on methods in which neighboring phases and oxidation could be minimized. Indeed, throughout all of our synthetic experiments, we found that $HfTe_2$ and $HfTe_5$ were significantly more thermodynamically stable than $HfTe_3$, indicating the careful precision needed when implementing experimental work. Furthermore, we found oxidation was a significant issue, and that precautionary measures such as carbon coated ampules, glovebox use, etc. were necessary when performing experiments.

In Chapter III, we focused on novel solid solutions of single crystalline $Hf_xZr_{1-x}Te_3$ (x = 0.20, 0.40, 0.80) under CVT conditions by using the favored synthetic conditions of $HfTe_3$ and $ZrTe_3$. We found that each of the three different solid solutions we isolated were favored under different synthetic conditions, especially in terms of temperature (from 750–530 °C) and starting materials. Not surprisingly, we found as we increased Hf percentage that our synthetic conditions had to resemble the favored conditions of single crystalline $HfTe_3$ that we discussed in Chapter II. Furthermore, like $HfTe_3$, our syntheses had to be carefully tailored to avoid both neighboring phases and oxidation. We also briefly examined solid solutions of $Ti_xZr_{1-x}Te_3$ and $Ti_xHf_{1-x}Te_3$, but we found Ti incorporation was minimal or absent in the products.

Finally, in Chapter IV, we shifted our focus to group IV transition metal dichalcogenide solid solutions including $Ti_xZr_{1-x}Te_2$ (x = 0.30, 0.50, 0.80), $Ti_xHf_{1-x}Te_2$ (x = 0.25, 0.40, 0.80), and $Ti_xZr_{1-x}Se_2$ (x = 0.25, 0.50, 0.75) using CVT conditions. For $Ti_xZr_{1-x}Te_2$ and $Ti_xHf_{1-x}Te_2$ solid solutions, we leveraged the favored synthetic conditions of $TiTe_2$, $ZrTe_2$, and $HfTe_2$ from temperatures ranging 875–825 °C. For $Ti_xZr_{1-x}Se_2$ solid solutions, we found that all of the resulting phases were favored under a tight temperature gradient from 900–870 °C. Under different

temperatures and temperature gradients, we found that there was either inadequate crystal growth or significant deviations in phase isolation.

The worked described here in this dissertation provides significant synthetic routes and characterization for a number of group IV transition metal chalcogenide materials. In Chapter II we provided insights into the isolation of $HfTe_3$. A significant amount of work has been reported for $ZrTe_3$, $HfTe_2$, and $HfTe_5$ thus far in the literature, especially compared to $HfTe_3$. Undoubtedly, the lack of reports is due to the difficulty in isolating this material which we hope this chapter has addressed. Potential properties of $HfTe_3$ include its current density and plasmonic properties. As already mentioned, $ZrTe_3$ has an exceptionally high current density, which may indicate that $HfTe_3$ has comparable properties especially considering their isostructural relationship. Furthermore, we have recently began using scanning transmission electron microscopy (STEM) coupled with electron energy loss spectroscopy (EELS) to find localized surface plasmon resonance (LSPR) modes in $HfTe_3$. This approach has been well reported in the literature, and our preliminary results are very promising.[8]

For our work with the $Hf_xZr_{1-x}Te_3$ solid solutions, there are a considerable number of directions that property investigations can go. In addition, many researchers have also studied the tunability of charge density wave (CDW) transitions and superconductivity by tuning $ZrTe_3$ using techniques such as transition metal intercalation, chalcogen doping, pressure application, and alloying.[9,10,11,12,13,14] Given these reports, there is promise in seeing how these properties change as a function of metal alloying. We also briefly examined isolation of $Ti_xZr_{1-x}Te_3$ and $Ti_xHf_{1-x}Te_3$ solid solutions. While the synthesis of these solid solutions are very promising, more work is needed in isolating these materials. Even though the synthetic conditions of $ZrTe_3$ and $HfTe_3$ are now well described, the isolation of bulk $TiTe_3$ has yet to be reported which we hypothesize is

contributing to synthetic challenges. Indeed, there is currently only one report thus far of $TiTe_3$ being synthesized in the few chain limit in multiwalled carbon nanotubes.[15]

We have also isolated a number of transition metal dichalcogenide solid solutions including $Ti_xZr_{1-x}Te_2$, $Ti_xHf_{1-x}Te_2$, and $Ti_xZr_{1-x}Se_2$ that may have promising properties. $Ti_xZr_{1-x}Se_2$ solid solutions may be especially promising as there was a recent report by Mahapatra and coworkers in which their theoretical studies found that the solid solution $Ti_{0.50}Zr_{0.50}Se_2$ may exhibit CDW transitions.[16] While we were able to isolate three different compositions reliably, crystal growth for the $Ti_{0.25}Zr_{0.75}Se_2$ was minimal, especially compared to $Ti_{0.50}Zr_{0.50}Se_2$ and $Ti_{0.75}Zr_{0.25}Se_2$. Future synthetic work with this particular composition is necessary.

The synthesis, characterization, and property investigation of transition metal chalcogenide materials has garnered a significant amount of interest in the materials science field. As demonstrated in this dissertation, the directions in which these materials can be isolated is vast, and with these innovations comes rich opportunities for potential new properties and applications.

References

1. Tang, Q.; Zhou, Z. Graphene-Analogous Low-Dimensional Materials. *Prog. Mater. Sci.* **2013**, *58*, 1244-1315.

2. Island, J.; Molina-Mendoza, A.; Barawi, M.; Biele, R.; Flores, E.; Clamagirand, J.; Ares, J.; Sánchez, C.; van der Zant, H.; D'Agosta, R.; Ferrer, I.; Castellanos-Gomez, A. Electronics and Optoelectronics of Quasi-1D Layered Transition Metal Trichalcogenides. *2D Mater.* **2017**, *4*, 022003.

3. Manzeli, S.; Ovchinnikov, D.; Pasquier, D.; Yazyev, O.; Kis, A. 2D Transition Metal Dichalcogenides. *Nat. Rev. Mater.* **2017**, *2*, 17033.

4. Geremew, A.; Bloodgood, M.; Aytan, E.; Woo, B.; Corber, S.; Liu, G.; Bozhilov, K.; Salguero, T.; Rumyantsev, S.; Rao, M.; Balandin, A.A. Current Carrying Capacity of Quasi-1D $ZrTe_3$ van der Waals Nanoribbons. *IEEE Electron Device Lett.* **2018**, *39*, 735-738.

5. Geremew, A.; Rumyantsev, S.; Bloodgood, M.; Salguero, T.; Balandin, A. Unique Features of the Generation–Recombination Noise in Quasi-One-Dimensional van der Waals Nanoribbons. *Nanoscale* **2018**, *10*, 19749-19756.

6. Denholme, S.; Yukawa, A.; Tsumura, K.; Nagao, M.; Tamura, R.; Watauchi, S.; Tanaka, I.; Takayanagi, H.; Miyakawa, N. Coexistence of Superconductivity and Charge-Density Wave in the Quasi-One-Dimensional Material $HfTe_3$. *Sci. Rep.* **2017**, *7*, 45217.

7. Li, J.; Peng, J.; Zhang, S.; Chen, G. Anisotropic Multichain Nature and Filamentary Superconductivity in the Charge Density Wave System $HfTe_3$. *Phys. Rev. B* **2017**, *96*, 174510.

8. Wu, Y.; Li, G.; Camden, J. Probing Nanoparticle Plasmons with Electron Energy Loss Spectroscopy. *Chem. Rev.* **2017**, *118*, 2994-3031.

9. Zhu, X.; Ning, W.; Li, L.; Ling, L.; Zhang, R.; Zhang, J.; Wang, K.; Liu, Y.; Pi, L.; Ma, Y.; Du, H.; Tian, M.; Sun, Y.; Petrovic, C.; Zhang, Y. Superconductivity and Charge Density Wave in $ZrTe_{3-x}Se_x$. *Sci. Rep.* **2016**, *6*, 26974.

10. Lei, H.; Zhu, X.; Petrovic, C. Raising T_c in Charge Density Wave Superconductor $ZrTe_3$ by Ni Intercalation. *Europhys. Lett.* **2011**, *95*, 17011.

11. Zhu, X.; Lei, H.; Petrovic, C. Coexistence of Bulk Superconductivity and Charge Density Wave in Cu_xZrTe_3. *Phys. Rev. Lett.* **2011**, *106,* 246404.

12. Tsuchiya, S.; Matsubayashi, K.; Yamaya, K.; Takayanagi, S.; Tanda, S.; Uwatoko, Y. Effects of Pressure and Magnetic Field on Superconductivity in $ZrTe_3$: Local Pair-Induced Superconductivity. *New J. Phys.* **2017**, *19*, 063004.

13. Yomo, R.; Yamaya, K.; Abliz, M.; Hedo, M.; Uwatoko, Y. Pressure Effect on Competition Between Charge Density Wave and Superconductivity in $ZrTe_3$: Appearance of Pressure-Induced Reentrant Superconductivity. *Phys. Rev. B* **2005**, *71*, 132508.

14. Liu, Y.; Hu, Z.; Tong, X.; Leshchev, D.; Zhu, X.; Lei, H.; Stavitski, E.; Attenkofer, K.; Petrovic, C. Thermal Transport and Mixed Valence in $ZrTe_3$ Doped with Hf and Se. *Appl. Phys. Lett.* **2022**, *120*, 022601.

15. Stonemeyer, S.; Cain, J.; Oh, S.; Azizi, A.; Elasha, M.; Thiel, M.; Song, C.; Ercius, P.; Cohen, M.; Zettl, A. Stabilization of $NbTe_3$, VTe_3, and $TiTe_3$ via Nanotube Encapsulation. *J. Am. Chem. Soc.* 2021, *143*, 4563-4568.

16. Kabiraj, A.; Mahapatra, S. Machine-Intelligence-Driven High-Throughput Prediction of 2D Charge Density Wave Phases. *J. Phys. Chem. Lett.* **2020**, *11*, 6291-6298.